TAMPEREEN TEKNILLINEN YLIOPISTO
TAMPERE UNIVERSITY OF TECHNOLOGY

Kari Lappalainen

Output Power Variation and Mismatch Losses of Photovoltaic Power Generators Caused by Moving Clouds

Julkaisu 1506 • Publication 1506

Tampere 2017

Tampereen teknillinen yliopisto. Julkaisu 1506
Tampere University of Technology. Publication 1506

Kari Lappalainen

Output Power Variation and Mismatch Losses of Photovoltaic Power Generators Caused by Moving Clouds

Thesis for the degree of Doctor of Science in Technology to be presented with due permission for public examination and criticism in Sähkötalo Building, Auditorium SA203, at Tampere University of Technology, on the 17th of November 2017, at 12 noon.

Tampereen teknillinen yliopisto - Tampere University of Technology
Tampere 2017

Doctoral candidate:	Kari Lappalainen Laboratory of Electrical Energy Engineering Faculty of Computing and Electrical Engineering Tampere University of Technology Finland
Supervisor:	Seppo Valkealahti, Professor Laboratory of Electrical Energy Engineering Faculty of Computing and Electrical Engineering Tampere University of Technology Finland
Pre-examiners:	Ralph Gottschalg, Professor Centre for Renewable Energy Systems Technology Loughborough University United Kingdom
	Jan Kleissl, Associate Professor Department of Mechanical and Aerospace Engineering University of California United States of America
Opponent:	Jero Ahola, Professor LUT School of Energy Systems Lappeenranta University of Technology Finland

ISBN 978-952-15-4033-2 (printed)
ISBN 978-952-15-4044-8 (PDF)
ISSN 1459-2045

ABSTRACT

Photovoltaic (PV) systems are affected by irradiance fluctuations, mainly caused by overpassing cloud shadows, suffering from fluctuating output power. With high PV penetration levels, these fluctuations can lead to power system instability and problems in power quality. Further, overpassing cloud shadows cause partial shading (PS) which is the main cause of mismatch losses in PV systems. Mismatch losses occur in every PV system when interconnected PV cells have different electrical characteristics at a specific instant. Mismatch losses are mainly caused by PS but also by other differences in the operating conditions of PV modules, module damages and manufacturing tolerances. Moreover, PS can lead to failures in maximum power point tracking thereby causing extra losses.

In this thesis, the output power variation and mismatch losses of PV arrays caused by the edges of moving cloud shadows are studied by simulations based on a comprehensive analysis of the measured irradiance data of the solar PV power station research plant of Tampere University of Technology. Shadings caused by moving clouds, especially the characteristics of irradiance transitions caused by the edges of cloud shadows, are analysed. For that purpose, methods to identify irradiance transitions and shading periods caused by moving clouds in measured irradiance data and a method to determine apparent shadow edge velocity were developed. A mathematical model of irradiance transitions caused by moving clouds to be used in the simulations of PV system operation was developed and verified. A parametrisation method of irradiance transitions was also developed to make the simulations of PV system operation computationally less demanding.

The study of the output power variation and mismatch losses of PV arrays is conducted using the developed mathematical model of irradiance transitions and an experimentally verified MATLAB Simulink model of a PV module. The output power variation and mismatch losses of various electrical PV array configurations are studied during the irradiance transitions identified in the measured irradiance data. The effects of irradiance transition characteristics and the layout and geographic orientation of PV arrays on the output power variation and mismatch losses are studied and the overall effect of the mismatch losses caused by moving clouds on the energy production of PV plants is determined.

It is shown that the electrical configuration of PV arrays has only minor effects on the output power variation and mismatch losses of the arrays. Furthermore, it is shown that the mismatch losses caused by moving cloud shadows have only a minor effect on the overall efficiency of PV arrays. Even that can be largely eliminated by minimising PV string diameters.

PREFACE

The work was carried out at the Department of Electrical Engineering at Tampere University of Technology (TUT) during the years 2014–2017. The research was funded by TUT and ABB Oy. Grants from Walter Ahlström and Ulla Tuominen Foundations are greatly appreciated.

First of all, I want to thank Professor Seppo Valkealahti for supervising my thesis and providing guidance throughout my journey towards the doctoral degree. Secondly, I want to thank all my colleagues who have influenced my research, especially Assistant Professor Tuomas Messo, D.Sc. Juha Jokipii, M.Sc. Jukka Viinamäki, M.Sc. Aapo Aapro, M.Sc. Jyri Kivimäki and M.Sc. Kimmo Lummi. Moreover, I want to express my gratitude to the pre-examiners of the thesis, Professor Ralph Gottschalg from Loughborough University and Associate Professor Jan Kleissl from University of California, for their valuable comments and suggestions on how to improve the manuscript. I am also grateful to Professor Jero Ahola from Lappeenranta University of Technology for agreeing to act as an opponent in the public examination of the thesis. Finally, I want to thank all my relatives and friends who have supported me throughout my studies.

Tampere, September 2017

Kari Lappalainen

CONTENTS

LIST OF SYMBOLS AND ABBREVIATIONS

Abbreviations

AC	Alternating current
AM	Air mass
BL	Bridge-link
CdTe	Cadmium telluride
CIGS	Copper indium gallium diselenide
CA	Cloud amount
DC	Direct current
EU	European Union
GaAs	Gallium arsenide
GaInP	Gallium indium phosphide
HC	Honey-comb
IEA	International Energy Agency
LCE	Linear Cloud Edge
MPP	Maximum power point
MPPT	Maximum power point tracking
MS	Multi-string
NMRSD	Normalised root-mean-square deviation
NREL	National Renewable Energy Laboratory
OC	Open-circuit
p.u.	Per unit
PCC	Pearson correlation coefficient
PS	Partial shading
PV	Photovoltaic
RMSD	Root-mean-square deviation
SC	Short-circuit
Si	Silicon
SP	Series-parallel
SS	Shading strength
STC	Standard test conditions
TCT	Total-cross-tied

TUT	Tampere University of Technology

Greek alphabet

α	Angle between the shadow movement direction and the line between sensors S_o and S_a
β	Angle between the shadow edge and the line between sensors S_o and S_a
γ	Angle between the shadow edge normal and the line between sensors S_o and S_a
δ	Angle between the shadow edge normal and the movement direction of the shadow
θ	Angle between the line between sensors S_o and S_a and the line between sensors S_o and S_b

Latin alphabet

A	Ideality factor
A_1	Ideality factor of diode 1
A_2	Ideality factor of diode 2
A_{bypass}	Ideality factor of a bypass diode
b	Steepness related parameter in the mathematical model of irradiance transitions
$\hat{\boldsymbol{c}}$	Unitary vector in the direction of the shadow edge
d_a	Distance between sensors S_o and S_a
d_b	Distance between sensors S_o and S_b
E_a	Apparent shadow edge point that would pass over sensor S_a if the shadow moved to the direction of its edge normal
E_b	Apparent shadow edge point that would pass over sensor S_b if the shadow moved to the direction of its edge normal
E_F	Fermi energy
E_g	Band gap energy
E_p	Energy of a photon
f	Frequency of a photon
G	Irradiance
G_s	Irradiance under full shading
G_{us}	Irradiance of an unshaded situation
h	Planck’s constant
I_d	Current through a diode

I_{MPP}	Maximum power point current
$I_{\mathrm{MPP,\ STC}}$	Maximum power point current in standard test conditions
I_{o}	Dark saturation current
I_{o1}	Dark saturation current due to recombination in quasi-neutral regions
I_{o2}	Dark saturation current due to recombination in a depletion region
$I_{\mathrm{o,\ bypass}}$	Dark saturation current of a bypass diode
I_{ph}	Light-generated current
I_{SC}	Short-circuit current
$I_{\mathrm{SC,\ STC}}$	Short-circuit current in standard test conditions
I_{sh}	Current through a shunt resistance
k	Boltzmann constant
L1, L2 and L3	Phases 1, 2 and 3 of an electrical grid
N	Neutral of an electrical grid
N_{s}	Number of PV cells in a PV module
P_{MPP}	Power at maximum power point
$P_{\mathrm{MPP,\ STC}}$	Power at maximum power point in standard test conditions
q	Elementary charge
$\boldsymbol{r}_{\mathrm{a}}$	Position vector of sensor $\mathrm{S_a}$
$\boldsymbol{r}_{\mathrm{b}}$	Position vector of sensor $\mathrm{S_b}$
$\boldsymbol{r}_{\mathrm{E_a}}$	Position vector of point $\mathrm{E_a}$
$\boldsymbol{r}_{\mathrm{E_b}}$	Position vector of point $\mathrm{E_b}$
R_{s}	Series resistance
$R_{\mathrm{s,\ bypass}}$	Series resistance of a bypass diode
R_{sh}	Shunt resistance
S1, S2, S3, …	Irradiance sensors 1, 2, 3 and so on of the solar photovoltaic power station research plant of Tampere University of Technology
$\mathrm{S_a}$, $\mathrm{S_b}$ and $\mathrm{S_o}$	Irradiance sensors of the sensor triplet
t	Time
T	Temperature of a PV cell
t_0	Duration related parameter in the mathematical model of irradiance transitions
t_{a}	Time lag of shading or brightening of sensor $\mathrm{S_a}$ after shading or brightening of sensor $\mathrm{S_o}$ during the irradiance transition
t_{a1}	Time lag of shading of sensor $\mathrm{S_a}$ after shading of sensor $\mathrm{S_o}$ during the irradiance fall
t_{a2}	Time lag of brightening of sensor $\mathrm{S_a}$ after brightening of sensor $\mathrm{S_o}$ during the irradiance rise

t_b	Time lag of shading or brightening of sensor $\mathrm{S_b}$ after shading or brightening of sensor $\mathrm{S_o}$ during the irradiance transition
t_b1	Time lag of shading of sensor $\mathrm{S_b}$ after shading of sensor $\mathrm{S_o}$ during the irradiance fall
t_b2	Time lag of brightening of sensor $\mathrm{S_b}$ after brightening of sensor $\mathrm{S_o}$ during the irradiance rise
U_MPP	Maximum power point voltage
$U_\mathrm{MPP,\,STC}$	Maximum power point voltage in standard test conditions
U_OC	Open-circuit voltage
$U_\mathrm{OC,\,STC}$	Open-circuit voltage in standard test conditions
U_T	Thermal voltage
v	Speed of a shadow
$\boldsymbol{v}$	Velocity of a shadow
v_e	Apparent speed of a shadow edge
$\boldsymbol{v}_\mathrm{e}$	Apparent velocity of a shadow edge

1 INTRODUCTION

The wide consumption of the energy sources of nature has had an essential effect on the development of our modern civilization. The increase of the energy consumption has been very rapid since the industrial revolution began in the late 18th century (Bose, 2013). In consequence of this development, humankind is now more dependent on energy than ever before. In 2014, the world energy consumption was about 109.6 PWh and its growth has been predicted to continue (International Energy Agency (IEA), 2016a).

Since the industrial revolution, the main energy sources have been coal, oil and natural gas, which are fossil fuels. However, general concern about the climate change and the increase of carbon dioxide emissions has raised interest towards sustainable energy sources and energy efficient solutions. As for the awareness of the limitedness of fossil fuel reserves and the fear of the price increase and exhaustion of them, they have increased interest in the development and implementation of renewable energy technologies. European Union (EU) countries have agreed on a framework for climate and energy, including EU-wide targets and policy objectives for 2030. The targets are a 40% reduction in greenhouse gas emissions from 1990 levels, at least a 27% share of renewable energy consumption and at least 27% energy savings compared with the business-as-usual scenario (European Commission, 2017).

Renewable energy is energy derived from constantly replenish natural processes. Renewable energy sources include hydropower, wave, tide, biomass, wind, solar and geothermal resources. In 2014, 13.8% of world total primary energy supply and 22.3% of global electricity generation were produced from renewable energy sources (IEA, 2016b).

Solar energy is the most promising way to combat climate change and secure energy production. The incident solar power at the surface of the Earth is about 86 PW (Hermann, 2006). Thus, the amount of energy coming from the Sun to the surface of the Earth in just one and a half hours is more than the world energy consumption was in 2014. The power available from all the rest of the renewable energy sources is less than 1% of the available solar power (Abbot, 2010). These facts clearly demonstrate that solar, the dominant source of renewable energy, is where the effort of humankind must stay focussed for the future.

Solar energy can be exploited by two main ways, by utilising the heating effect of solar radiation or by conversing solar energy directly into electrical energy by using photovoltaic (PV) cells. The operation of PV cells is based on the photovoltaic effect. This phenomenon was first observed by Alexandre-Edmond Becquerel in 1839 and later explained by Albert Einstein in 1905. The first functional PV cell, with an efficiency of 1%, was made of selenium and gold leaf film by Charles Fritts in 1883 (Hegedus and Lugue, 2011). The modern era of PV can be considered to have begun in 1954 when the first appropriate silicon (Si) PV cell for energy production, with an efficiency of 6%, was developed by Chapin et al. (1954) at Bell Laboratories.

During the past decades, remarkable improvements in the efficiencies of PV cells have been achieved while PV cells have become radically cheaper. Between 2005 and 2015, the efficiency of average commercial crystalline silicon PV modules increased from about 12% to 17% (Fraunhofer Institute for Solar Energy Systems, 2016). At the same time, material usage for crystalline silicon PV cells reduced about 60% due to increased efficiencies and thinner wafers. The highest confirmed efficiencies for a terrestrial crystalline silicon PV cell and module are 26.6% (National Renewable Energy Laboratory (NREL), 2017) and 24.4% (Green et al., 2017), respectively. The cost of PV power has fallen dramatically during the past decade. Between 2008 and 2015, the average cost of utility-scale PV systems decreased by around 80% (IEA, 2015). Along with the PV power price development, PV is increasingly cost competitive with fossil fuels and onshore wind power (SolarPower Europe, 2016).

As a consequence of the price development and policy drivers for PV, the development of installed PV power capacity has been impressive during the past decade. The global cumulative installed PV power capacity was 229.3 GW in the end of 2015, while just 5 years earlier in 2010 it was less than 41 GW (European Photovoltaic Industry Association, 2013; SolarPower Europe, 2016). From the end of 2005, when the total PV capacity was 5.4 GW, the PV market has grown over 40 times in just one decade. In the end of 2015, the three countries with the largest cumulative PV capacities were China, Germany and Japan, respectively (SolarPower Europe, 2016). With a global total production share of over 90% in 2015, crystalline silicon is by far the most important PV technology (Fraunhofer Institute for Solar Energy Systems, 2016).

PV systems are prone to irradiance fluctuations caused by overpassing cloud shadows that are the main cause of fluctuating PV power production. As the share of PV power production increases, there is a growing potential for PV output power variability having a negative effect on the power quality and reliability of the electrical grid. Thus, with the fast growth of PV power production, technical requirements, such as ramp rate control, low voltage ride-through capability and reactive power capability, are now being mandated to accommodate large amounts of PV power production in the power systems (Eftekharnejad et al., 2013; Woyte et al., 2006; Yang et al., 2014). Although the geographic dispersion of PV power production has been found to dampen the effects of irradiance fluctuations (Lave et al., 2012; Marcos et al., 2011, 2012; Perpiñán et al., 2013), they are of special importance locally and in weak grids with high PV penetration levels. During the past years, several studies have been presented regarding the output power variation of PV systems, e.g. Hoff and Perez (2010, 2012), Marcos et al. (2011, 2014, 2016), van Haaren et al. (2014) and Yan et al. (2016). For example, up to 70% per minute variations have been recorded at a 9.5 MWp PV power plant (Marcos et al., 2011).

Solar radiation variability caused by overpassing cloud shadows has been studied by several researchers at several specific locations previously: 1 and 5 min resolution irradiance data at four sites across Colorado was used in Lave and Kleissl (2010); from 20 s to 1 min data at 24 sites in the United States was used in Perez et al. (2011); 1–30 s irradiance data from 10 locations in the United States was used in Lave et al. (2015); 1 s data from six PV plants in Spain was used in Marcos et al. (2011); 1 s resolution irradiance data from Estonia was used in Tomson (2010) and Tomson and Hansen (2011) and 1 s data from Hawaii was used in Hinkelman (2013). Solar radiation variability and irradiance transitions caused by the edges of moving cloud shadows have been studied also e.g. in Tomson (2013) and Tomson and Tamm (2006). Determination of shadow velocity has been studied, e.g. in Bosch and Kleissl (2013), Bosch et al. (2013) and Fung et al. (2014). A cloud shadow model for PV system analysis has been proposed by Cai and Aliprantis (2013).

Overpassing cloud shadows are a significant reason for the mismatch losses of PV systems. Mismatch losses occur in every PV system when interconnected PV cells have different electrical characteristics at a specific instant. Mismatch losses are mainly caused by partial shading (PS) but also by other differences in the operating conditions of PV modules, module damages and manufacturing tolerances. PS caused by moving clouds can also lead to failures in maximum power point (MPP) tracking (MPPT) thereby causing additional losses. While the PS of large-scale PV plants is mainly caused by overpassing cloud shadows, it can also exist due to, inter alia, surrounding objects, snow or soiling.

The mismatch losses of PV generators caused by PS and their mitigation have been studied in several papers, especially during the past years, e.g. in Picault et al. (2010), Potnuru et al. (2015), Rakesh and Madhavaram (2016), Shams El-Dein et al. (2013a, 2013b), Vijayalekshmy et al. (2016) and Villa et al. (2012). In these papers, mismatch losses caused by shadings with large irradiance differences between adjacent PV modules, i.e., extremely sharp shadows, have been studied. Mismatch losses under PS conditions caused by moving clouds have been studied based on irradiance measurements in Torres Lobera and Valkealahti (2013) and based on electrical measurements in Rodrigo et al. (2016).

A large amount of academic research has been conducted and is most probably ongoing related to the mitigation of the effects of PS introducing different electrical configuration schemas, shading dispersion techniques, etc. Those studies are typically based on hypothetical PS conditions lacking the knowledge of real irradiance transitions caused, for example, by moving clouds. The first objective of this thesis is to fill up that gap of knowledge by analysing the real shadings caused by moving clouds. Especially, the goal is to study the characteristics of irradiance transitions caused by the edges of cloud shadows. The second objective is to develop a mathematical model of those irradiance transitions to be used in the simulations of PV system operation.

When a cloud shadow is covering a PV array, the apparent speed of the shadow edge, i.e., the component of shadow speed normal to the shadow edge, actually defines how fast the PV array is becoming shaded. Thus, the apparent velocity of a linear shadow edge is a vital quantity in any analysis of the effects of overpassing cloud shadows on the operation of small PV systems and the arrays of large PV power plants. Still, the assumption of linearity for the shadow edge might not be valid for large PV power plants as a whole. The apparent velocity and the length of irradiance transitions have not been studied earlier.

To achieve the first two objectives of the thesis, methods to identify irradiance transitions and shading periods due to moving clouds in measured irradiance data and a method to determine apparent shadow edge velocity were developed. A shading period is defined as a combination of a decreasing and increasing irradiance transition with steady shading between them. Further, a parametrisation method of irradiance transitions caused by moving clouds was developed to make the simulations of PV system operation computationally less demanding.

This thesis presents a comprehensive study of the output power variation and mismatch losses of PV arrays caused by moving clouds. The output power variation and mismatch losses of various electrical PV array configurations were studied during the irradiance transitions identified in the measured irradiance data of the solar PV power station research plant of Tampere University of Technology (TUT). The effects of irradiance transition characteristics and the layout and geographic orientation of PV arrays on the output power variation and mismatch losses were studied and the overall effect of the mismatch losses caused by moving clouds on the energy production of PV plants was determined. The study was conducted using the developed mathematical model of irradiance transitions and an experimentally verified MATLAB Simulink model of a PV module. The developed parametrisation method of irradiance transitions was used to study the effects of the layout and geographic orientation of PV arrays on the output power variation and mismatch losses.

The main scientific contribution of the thesis can be summarised as:

- Methods to identify irradiance transitions and shading periods caused by moving clouds in measured irradiance data and a method to determine apparent shadow edge velocity were developed.

- The characteristics of irradiance transitions and shading periods caused by moving clouds were studied comprehensively.

- A mathematical model of irradiance transitions caused by moving clouds was developed and verified.

- A parametrisation method of irradiance transitions caused by moving clouds was developed and its applicability for researching the output power variation and mismatch losses of PV arrays was verified.

- The output power variation of various electrical PV array configurations during irradiance transitions caused by moving clouds was studied more comprehensively than has been done earlier. The effects of irradiance transition characteristics, PV array layout and its geographic orientation on the output power variation were studied.

- The mismatch losses of various electrical PV array configurations during irradiance transitions caused by moving clouds were studied more comprehensively than has been done earlier. The effects of irradiance transition characteristics, PV array layout and its geographic orientation on the mismatch losses caused by moving clouds were studied.

- The overall effect of the mismatch losses caused by moving clouds on the energy production of PV plants was studied.

This thesis is mainly based on the following publications:

[P1] Lappalainen, K. and Valkealahti, S. 2015. Recognition and modelling of irradiance transitions caused by moving clouds. Solar Energy, 112(2), pp. 55–67.

[P2] Lappalainen, K. and Valkealahti, S. 2016. Mathematical Parametrisation of Irradiance Transitions Caused by Moving Clouds for PV System Analysis. 32nd European Photovoltaic Solar Energy Conference and Exhibition, Munich, Germany, June 22–24, pp. 1485–1489.

[P3] Lappalainen, K. and Valkealahti, S. 2016. Analysis of shading periods caused by moving clouds. Solar Energy, 135(13), pp. 188–196.

[P4] Lappalainen, K. and Valkealahti, S. 2016. Apparent velocity of shadow edges caused by moving clouds. Solar Energy, 138(16), pp. 47–52.

[P5] Lappalainen, K. and Valkealahti, S. 2016. Effects of Irradiance Transitions on the Output Power Fluctuations of Different PV Array Configurations. IEEE Innovative Smart Grid Technologies Asia Conference, Melbourne, Australia, November 28 – December 1, pp. 705–711.

[P6] Lappalainen, K. and Valkealahti, S. 2017. Effects of irradiance transition characteristics on the mismatch losses of different electrical PV array configurations. IET Renewable Power Generation, 11(2), pp. 248–254.

[P7] Lappalainen, K. and Valkealahti, S. 2017. Effects of PV array layout, electrical configuration and geographic orientation on mismatch losses caused by moving clouds. Solar Energy, 144(4), pp. 548–555.

[P8] Lappalainen, K. and Valkealahti, S. 2017. Output power variation of different PV array configurations during irradiance transitions caused by moving clouds. Applied Energy, 190(6), pp. 902–910.

[P9] Lappalainen, K. and Valkealahti, S. 2017. Photovoltaic mismatch losses caused by moving clouds. Solar Energy, 158(18), pp. 455–461.

The author wrote the publications and carried out all the simulations and analysis. Professor Valkealahti provided comments regarding the theory and analysis and helped to refine the publications in terms of terminology and language.

The rest of the thesis is organised as follows. In Chapter 2, the backgrounds of the operation of PV power generators are introduced. The fundamentals of solar radiation and the operating principle of PV cells are presented and the most commonly used models for the electrical operation of PV cells are introduced. Further, the effects of irradiance and temperature on the operation of PV cells and the operation of PV modules under partial shading are illustrated. In the end of Chapter 2, different configurations of PV generators are presented.

Chapter 3 presents the methods to determine the characteristics of shadows of moving clouds. The developed methods for the identification of irradiance transitions and shading periods caused by moving clouds in measured irradiance data and the developed mathematical model of irradiance transitions are presented. The use of the Linear Cloud Edge (LCE) method presented by Bosch et al. (2013) to determine the velocity of shadows is illustrated and the developed method to determine apparent shadow edge velocity is presented.

In Chapter 4, the results of the study of the characteristics of shadows of moving clouds conducted using the methods presented in Chapter 3 are presented and discussed. In the beginning of the chapter, the used irradiance measurement data is presented. The characteristics of irradiance transitions and shading periods are presented, the mathematical model of irradiance transitions is verified and the results of shadow velocity and apparent shadow edge velocity are presented. In the end of the chapter, correlations between the characteristics of shadows are discussed.

Chapter 5 introduces the approach used to study the operation of PV generators. The used simulation model of PV modules, the studied PV arrays and the developed parametrisation method of irradiance transitions are presented. Furthermore, the shading of PV arrays is illustrated.

In Chapter 6, the results regarding the output power variation of PV generators caused by moving clouds are presented and discussed. The effects of irradiance transition characteristics, PV array layout and its geographic orientation on the output power variation are presented.

Chapter 7 presents and discusses the results regarding the mismatch losses of PV generators caused by moving clouds. The effects of irradiance transition characteristics, PV array layout and its geographic orientation on the mismatch losses are presented. Further, the overall effect of the mismatch losses caused by moving clouds on the energy production of PV plants is presented and discussed. Finally, the conclusions of the thesis are presented and some recommendations for future research topics are given in Chapter 8.

2 BACKGROUND OF THE THESIS

This chapter introduces the backgrounds of the operation of PV power generators. First, the fundamentals of solar radiation are presented. Then, the operating principle of p-n junction based PV cells is presented and the efficiencies of various PV technologies are discussed. After that, the most commonly used models for the electrical operation of PV cells are introduced. Further, the effects of the most important operating conditions, irradiance and temperature, on the operation of PV cells are discussed. After that, the operation of PV modules under partial shading is dealt with and it is explained why a series connection of PV cells is more prone to losses under non-uniform irradiance conditions than a parallel connection. Finally, different topologies to interface PV modules with an electrical grid as well as various electrical PV array configurations are presented.

2.1 Solar radiation

Life on the Earth depends on solar radiation that drives almost all known physical and biological cycles on the Earth. The Sun is a hot sphere of gas heated by nuclear fusion reactions in its core, which convert hydrogen nuclei into helium nuclei. This fusion process releases energy since the mass of the produced helium nuclei is lower than that of the hydrogen nuclei from which the helium nuclei are produced. The outer surface of the Sun, the photosphere, emits radiation into the space in the form of electromagnetic radiation.

The mean solar irradiance on a plane perpendicular to the radiation at the mean distance of the Earth from the Sun is called the solar constant. It has a generally accepted value of 1366 W/m^2 (Dunlop, 2007; Gueymard, 2004). The solar constant can be calculated by integrating the spectral irradiance on the outer surface of the atmosphere of the Earth over all wavelengths. In fact, the solar constant is not perfectly constant, but varies in relation to the solar activities. Solar radiation on the surface of the Earth is attenuated by the atmosphere due to such effects as Rayleigh scattering by molecules, scattering by aerosols and dust particles and absorption by atmospheric gases such as ozone, oxygen, carbon dioxide and water vapour (Wenham et al., 2007).

Rayleigh showed that the amount of scattering of solar radiation by atmospheric molecules is inversely proportional to the fourth power of the wavelength, when the sizes of particles are much smaller than the wavelength of the radiation (Fu, 2003). Thus, Rayleigh scattering affects especially the short wavelength region of the spectrum. We see blue sky since air molecules scatter solar radiation much more in the blue than in the red part of the spectrum.

The longer is the distance that solar radiation travels in the atmosphere, the more the atmosphere affects the solar radiation. The air mass (AM) describes the path length through the atmosphere that solar radiation must pass to reach the surface of the Earth. The AM is the quotient of that path length through the atmosphere and the thickness of the atmosphere. When the Sun is in the zenith, i.e., in the point in the sky directly overhead a particular location, the radiation has the shortest path through the atmosphere and the AM equals to 1.0 and is designated as AM1.0.

The radiation, that reaches the surface of the Earth, can be divided into direct and diffuse radiation. The radiation coming directly from the Sun is direct radiation and the scattered radiation coming from all the other directions is diffuse radiation. The sum of these two components as received on a horizontal plane is called global solar radiation. The diffuse component of AM1.0 radiation, when the sky is clear, i.e., there are no clouds, is about 10% (Wenham et al., 2007). The proportion increases with increasing AM or when clouds exist. Clouds are, naturally, a significant cause of solar radiation attenuation and scattering. In overcast weather, the share of diffuse radiation is typically from 90% to 100% (Tomson, 2014). Cloud amount (CA), also known as cloud cover or cloud fraction, is the fraction of the sky obscured by clouds. Global total CA is about 0.68 when considering clouds with optical depth larger than 0.1 (Stubenrauch et al., 2013).

Cloud motion has traditionally been estimated from satellite imagery (Hammer et al., 1999; Leese et al., 1971). Also methods using sky imagers have been presented, e.g. in Chow et al. (2011) and Wang et al. (2016). Since the distance between the Sun and the Earth is much larger than the distance between a cloud and the surface of the Earth, horizontal cloud velocity is typically almost equivalent to cloud shadow velocity on the ground (Fung et al., 2014). However, for example large solar zenith angles can introduce differences. While cloud velocity is useful for meteorological models it is not as useful as cloud shadow velocity for accurate analyses of PV system operation.

2.2 Photovoltaic effect and photovoltaic cells

A PV cell is a device that converts the energy of solar radiation directly into electrical energy. The operation of most PV cells is based on a p-n junction, albeit there are also PV cells that do not contain a p-n junction like dye-sensitized cells (Fonash, 2010). The simulation model of a PV cell used in this thesis is fitted to the characteristics of a polycrystalline silicon PV cell. Polycrystalline silicon was selected since, with a global total production share of over 65% in

2015, it is by far the most important PV technology (Fraunhofer Institute for Solar Energy Systems, 2016). However, similar basic behaviour would have also been found with other p-n junction based PV cells. In this section, the operating principle of PV cells based on a p-n junction is presented without going deep into semiconductor physics. The operation of PV cells has been presented in more detail, e.g. in Fonash (2010), Gray (2011), Green (1998) and Markvart (2000).

The operation of PV cells can be explained by using the energy band structure. In isolated atoms, electrons have a well-defined set of discrete energy levels available. As several atoms are brought closer together, electrons start to interact with other atoms in the molecule and these discrete energy levels spread out into the allowed bands of energy. At the absolute zero temperature, electrons occupy the lowest possible energy states. Thus, all available energy states up to a certain level are occupied. This energy level is called the Fermi level or the Fermi energy E_F. As the temperature increases, the energy of electrons increase and some electrons gain energy in excess of the Fermi level. The valence band is the highest energy band that is completely filled at the absolute zero temperature. The electrons of the valence band form bonds between the atoms. The next higher band is called the conduction band. The energy difference between the valence and conduction band is called the band gap or the energy gap E_g.

In a semiconductor at the absolute zero temperature, the Fermi level is between the valence and conduction band. Thus, the valence band is completely filled with electrons and the conduction band is completely empty. Neither a completely full nor empty energy band can contribute to current flow. If one electron from the valence band is excited into the conduction band, it is free to move there, and there is a vacant position on the valence band. An electron adjacent to the vacant position can move into it, leaving a new vacant position behind and so on. Thus, the motion of electrons is now possible on the valence band as well. This motion can be described simply as the motion of a single vacant position, called a hole, instead of describing it as the result of the movements of a number of electrons.

In 1905, Einstein postulated that light consists of discrete, independent particles of energy. These particles, the quanta of electromagnetic radiation, are called photons. This idea of the complementary nature of light is called the particle-wave duality. The energy of a photon E_p is equal to Planck's constant h times its frequency f (Young and Freeman, 2008). When light hits a material, a certain fraction of it is reflected and the remainder is transmitted into the material. The photons transmitted to the material can be absorbed by electrons exciting the electrons from occupied states to unoccupied higher-energy states. Exciting an electron from the valence band to the conduction band is possible if the energy of a photon is higher than the band gap.

In a pure semiconductor, a free electron will recombine and return to the valence band after a certain time, eliminating a valence band hole. The charge carrier lifetime in a material is the average time for recombination to occur after an electron-hole pair generation. Analogously, the charge carrier diffusion length is the average distance a charge carrier can move until recombination. For silicon, typical values for the charge carrier lifetime and diffusion length are 1 μs and 100–300 μm, respectively (Wenham et al., 2007).

Electrical properties of semiconductors are highly sensitive even to very small concentrations of impurities. Different types of semiconductor materials can be created by alloying semiconductor materials with impurity atoms (such as boron and phosphorus in case of silicon). The process is called doping. P-type semiconductor material contains additional holes and n-type material additional electrons.

In a pure semiconductor, recombination is strong since the force that separates electrons and holes is missing. Thus, the power generation of typical PV cells is based on the formation of a junction, which can separate the electrons and holes. The most typical junction is a p-n junction, which is an interface between p- and n-type semiconductor materials. When p- and n-type semiconductor materials are joined, there is a concentration difference of holes and electrons between the two types of semiconductors. Thus, electrons from the n-type material flow to the p-type material by diffusion leaving behind a positively charged region and, similarly, holes from the p-type material diffuse to the n-type material leaving behind a negatively charged region. Due to diffusion, an electric field is produced. This electric field counteracts the diffusion of the electrons and holes resulting in a drift current opposite to the diffuse current. In the thermal equilibrium, the diffusion and drift currents for both charge carrier types are exactly in balance, and thus there is no net current flow. The resulting junction region contains practically no mobile charge carriers and it is descriptively called the depletion region. The regions on either side of the depletion region where the electric field is very small are called the quasi-neutral regions. The electric field separates the created electron-hole pairs, the electrons are pulled to the n-type semiconductor and the holes to the p-type semiconductor. If the p-n junction is connected to an external load, electrons return from the n-type semiconductor to the p-type semiconductor through the load and electrical power is produced.

PV cells can be fabricated from a number of semiconductor materials. Materials are chosen mainly on the basis of their absorption characteristics and fabrication costs. Silicon (crystalline, polycrystalline and amorphous) is the most commonly used material because its absorption characteristics match fairly well to the solar spectrum and its fabrication technology is well developed (Gray, 2011). Other typical semiconductor materials used are gallium arsenide (GaAs), cadmium telluride (CdTe), copper indium gallium diselenide (CIGS) and gallium indium phosphide (GaInP). In addition to PV cells based on a single junction, multi-junction cells have been developed in order to utilise a larger part of the solar spectrum. There are also many emerging PV technologies, including dye-sensitized, perovskite, organic and quantum dot cells. The development of the best research PV cell efficiencies of different cell technologies according to NREL (2017) is shown in Fig. 2.1. The best efficiency under non-concentrated irradiance, 38.8%, has been achieved with a five-junction cell.

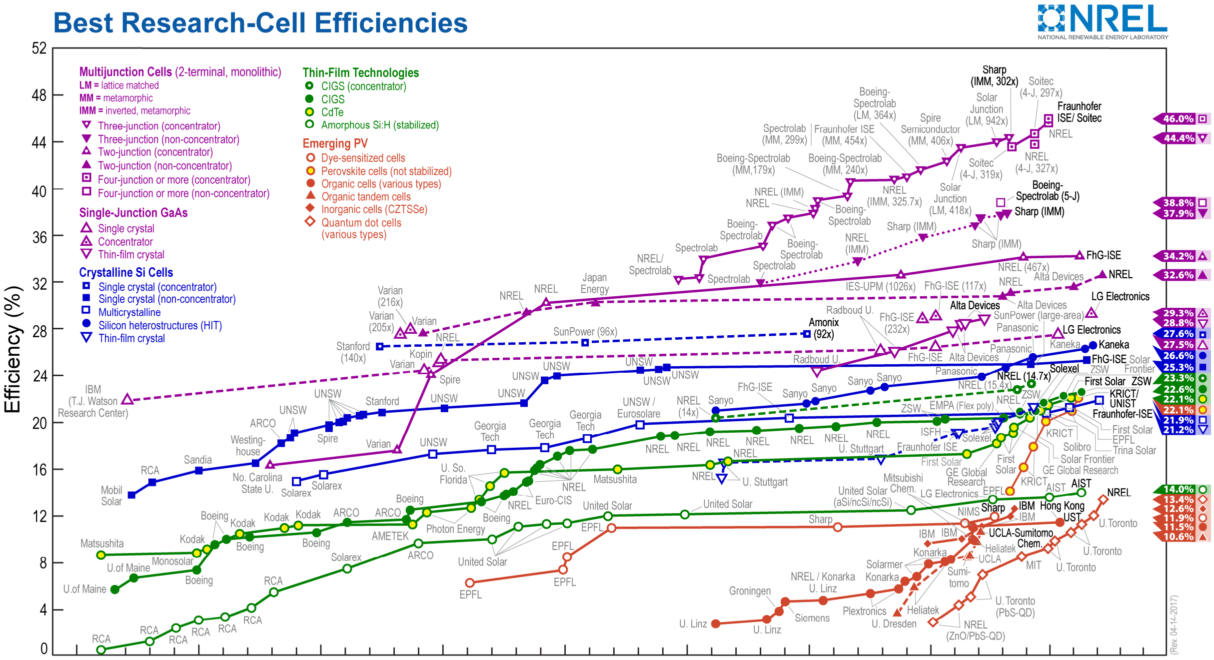

Figure 2.1. The best research PV cell efficiencies according to NREL (2017).

The main reason to the relatively low efficiencies is the fact that each absorbed photon creates only one electron-hole pair regardless of its energy. The energy of a photon may be much larger than the band gap but the resulting electron and hole are separated by only the band gap and the excess energy of the photon is dissipated as heat. This effect alone limits the maximum theoretical efficiency of a silicon PV cell to about 44% (Green, 1998). On the other hand, not every photon has enough energy to excite an electron from the valence band to the conduction band. According to Tiedje et al. (1984), the maximum theoretical efficiency of a silicon PV cell under AM1.5 global solar spectrum is 29.8%. As can be seen from Fig. 2.1, the best confirmed efficiency of a crystalline silicon PV cell under non concentrated irradiance (26.6%) is already close to that theoretical maximum.

2.3 Modelling of photovoltaic cells

Based on the extensive knowledge of semiconductor physics, the following general expression for the current produced by a PV cell can be derived:

$$I = I_{\mathrm{SC}} - I_{\mathrm{o1}}\left(e^{\frac{U}{A_1 U_{\mathrm{T}}}} - 1\right) - I_{\mathrm{o2}}\left(e^{\frac{U}{A_2 U_{\mathrm{T}}}} - 1\right), \tag{2.1}$$

where I is the current, I_{SC} the short-circuit (SC) current, U the voltage and U_{T} the thermal voltage of the PV cell (Gray, 2011). I_{o1} and I_{o2} are the dark saturation currents due to recombination in the quasi-neutral regions and in the depletion region, respectively. The thermal voltage of a PV cell can be expressed as $U_{\mathrm{T}} = kT/q$, where k is the Boltzmann constant, T the temperature of the cell and q the elementary charge. Based on Eq. (2.1), a PV cell can be modelled by an ideal current source I_{SC} in parallel with two diodes. In Eq. (2.1.), A_1 and A_2 are the ideality factors of these diodes with commonly used values of 1 and 2, respectively.

However, Eq. (2.1) neglects the effects of parasitic series and shunt resistance. The series resistance R_{s} is mainly due to the bulk resistance of the semiconductor material, the metallic contacts and interconnections, the contact resistance between the metallic contacts and the semiconductor and charge carrier transport through the top diffused layer. The shunt resistance R_{sh} is mainly due to p-n junction non-idealities and impurities near the junction, which cause partial shorting, especially near cell edges.

Adding the parasitic resistances into Eq. (2.1) leads to

$$I = I_{\mathrm{ph}} - I_{\mathrm{o1}}\left(e^{\frac{U+R_{\mathrm{s}}I}{A_1U_{\mathrm{T}}}} - 1\right) - I_{\mathrm{o2}}\left(e^{\frac{U+R_{\mathrm{s}}I}{A_2U_{\mathrm{T}}}} - 1\right) - \frac{U + R_{\mathrm{s}}I}{R_{\mathrm{sh}}}, \tag{2.2}$$

where I_{ph} is the light-generated current of the PV cell. The equivalent circuit of a PV cell with parasitic resistances based on Eq. (2.2) is shown in Fig. 2.2.

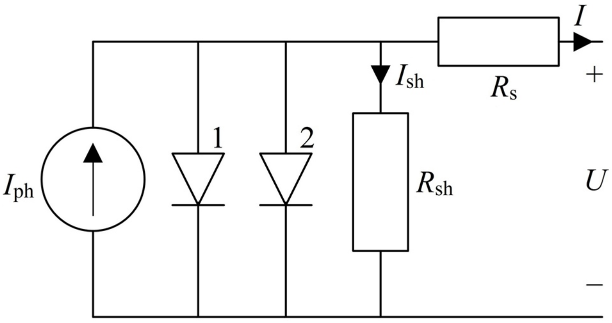

Figure 2.2. Equivalent circuit of a PV cell based on the two-diode model.

In a simplified electrical model of a PV cell, diodes 1 and 2 have been combined by ignoring recombination in the depletion region (diode 2). This is a reasonable and common assumption for a high quality PV cell (Gray, 2011). Combining the effects of the diodes using ideality factor A, which typically has a value between 1 and 2, yields the widely used relationship between the current and voltage of the PV cell

$$I = I_{\mathrm{ph}} - I_{\mathrm{o}}\left(e^{\frac{U+R_{\mathrm{s}}I}{AU_{\mathrm{T}}}} - 1\right) - \frac{U + R_{\mathrm{s}}I}{R_{\mathrm{sh}}} = I_{\mathrm{ph}} - I_{\mathrm{d}} - I_{\mathrm{sh}}, \tag{2.3}$$

where I_{o} is the dark saturation current of the cell, I_{d} the current through the diode and I_{sh} the current through the shunt resistance.

Although the two-diode model is more precise, a basic understanding of the behaviour of PV cells can be achieved via the one-diode model (Häberlin, 2012). Several authors, e.g. Mäki and Valkealahti (2014), Patel and Agarwal (2008), Sahu et al. (2016), Villalva et al. (2009) and Wang and Hsu (2011), have used the one-diode model in their researches. The equivalent circuit of a PV cell based on the one-diode model is shown in Fig. 2.3.

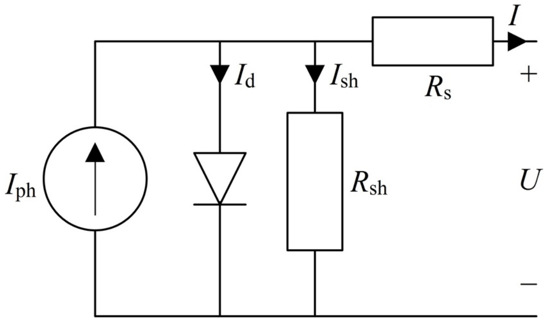

Figure 2.3. Equivalent circuit of a PV cell based on the one-diode model.

The *I–U* and *P–U* curves of a PV cell obtained by using the one-diode model are presented in Fig. 2.4. The characteristics are non-linear having only one MPP, i.e., a point at which the maximum power P_{MPP} can be produced. Other important values of the *I–U* curve are SC current I_{SC} at zero voltage and open-circuit (OC) voltage U_{OC} at zero current.

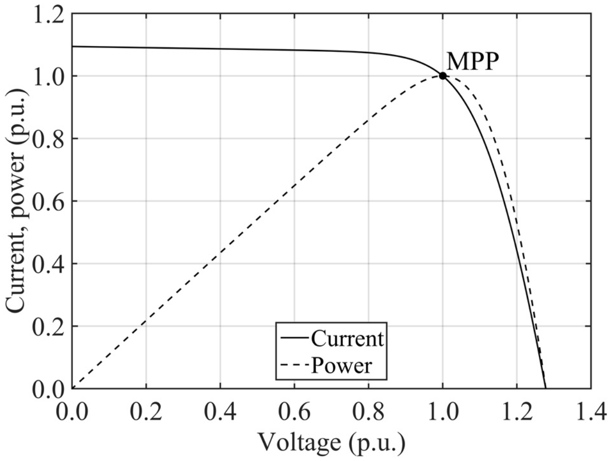

Figure 2.4. Current–voltage and power–voltage curves of a PV cell relative to the values at the MPP.

2.4 Effect of operating conditions

The *I–U* characteristic of a PV cell varies greatly with varying operating conditions. Thus, there is a need to specify the operating conditions in which PV cells are tested and rated. The most typically used test conditions are the standard test conditions (STC) which mean an irradiance of 1000 W/m^2 with AM1.5 spectrum and a cell temperature of 25 °C (Häberlin, 2012). The most important conditions relative to the operation of p-n junction based PV cells are incident irradiance and cell temperature. In this section, the effects of irradiance and temperature on the operation of PV cells are discussed based on the one-diode model.

The light-generated current of a PV cell is proportional to the flux of photons capable of creating electron-hole pairs. As the irradiance increases the photon flux increases, in the same portion, and generates a proportionately higher current. Thus, the SC current of a PV cell is directly proportional to the irradiance. The irradiance also affects the OC voltage, but the effect is much smaller. The effect of the irradiance on the *I–U* curve of a PV cell is illustrated in Fig. 2.5.

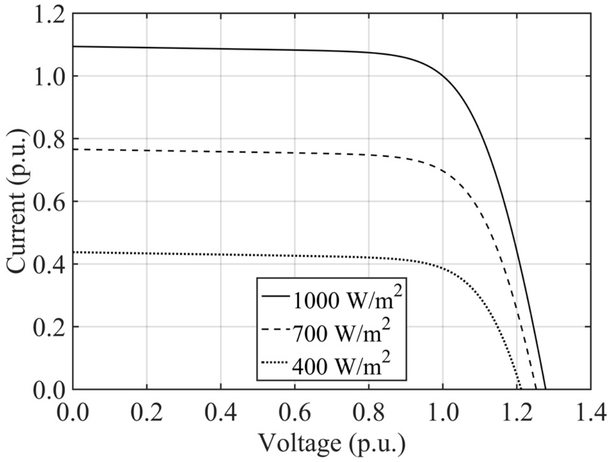

Figure 2.5. Effect of irradiance on the *I–U* curve of a PV cell relative to the values at the MPP at 1000 W/m^2. The temperature of the cell is 25 °C.

The irradiance dependencies of the SC current, OC voltage and maximum power of a PV cell are shown in Fig. 2.6. As can be seen in the figure, the OC voltage is strongly irradiance

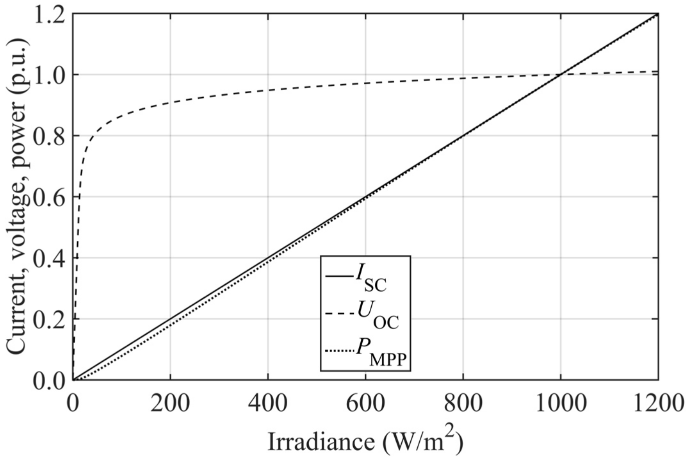

Figure 2.6. SC current, OC voltage and maximum power of a PV cell as a function of irradiance. The current, voltage and power are relative to the values at 1000 W/m^2. The temperature of the cell is 25 °C.

dependent only at the low values of the irradiance. It increases rapidly with the irradiance up to about 20 W/m^2 and is almost constant at the high values of the irradiance. The maximum power increases with the increasing irradiance, and, as presented earlier, the SC current is directly proportional to the irradiance.

The operating temperature of a PV cell depends on many factors, such as ambient temperature, incident irradiance, humidity and wind velocity as well as the physical properties of the cell. The effect of the temperature on the *I*–*U* curve of a PV cell is illustrated in Fig. 2.7. The temperature dependencies of the SC current, OC voltage and maximum power of a PV cell are shown in Fig. 2.8. As can be seen from these figures, the SC current increases and the OC voltage and maximum power decrease with the increasing temperature. The SC current increases with the temperature because the band gap energy decreases and photons with less energy are allowed to create electron-hole pairs. However, the effect of the temperature on the OC voltage

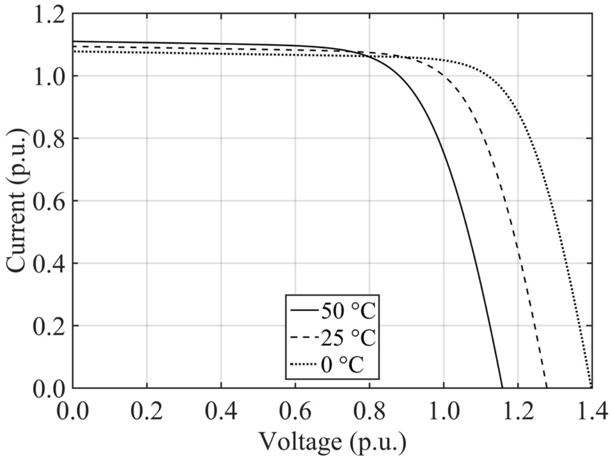

Figure 2.7. Effect of temperature on the *I*–*U* curve of a PV cell relative to the values at the MPP at 25 °C. The irradiance on the surface of the cell is 1000 W/m^2.

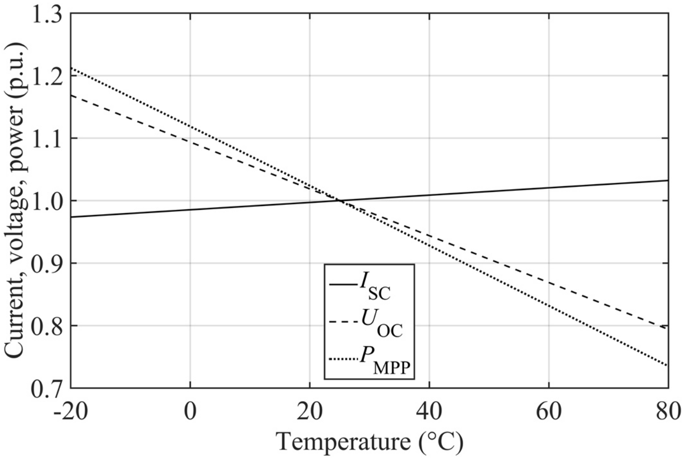

Figure 2.8. SC current, OC voltage and maximum power of a PV cell as a function of temperature. The current, voltage and power are relative to the values at 25 °C. The irradiance on the surface of the cell is 1000 W/m^2.

is significantly greater than on the SC current. The decrease of the maximum power with the increasing temperature is more rapid than that of the OC voltage.

2.5 Operation of photovoltaic modules under partial shading

Due to the low voltage and power levels of single PV cells, they are usually interconnected, in series or parallel, or both, to be used in electricity generation. Commercial crystalline Si PV cells have MPP voltage U_{MPP} ranging from around 0.45 to 0.58 V (Häberlin, 2012). Thus, PV cells are connected in series to increase the voltage level. Typically, from 32 to 72 PV cells are connected in series and encapsulated to form PV modules (Häberlin, 2012). PV modules, in turn, are the basic building blocks of PV arrays (generators) which are the power-generating units of PV power plants. Series connections of PV modules are called PV strings.

Ideally, a PV module would compose of identical PV cells with the identical characteristics. In that case, the *I–U* curve of a PV module would have the same shape as that of the individual cells, with a change in the scale of the axis. However, in practice PV cells are not identical and every cell has a unique characteristic.

The difference between the sum of the maximum powers of individual PV cells or modules of a PV system, as if they were operating separately, and the maximum power of the whole PV system is called mismatch losses. Mismatch losses exist since although a PV system would be operating in its global MPP, not all the cells or modules are operating in their own global MPPs. Mismatch losses are mainly caused by PS but also by other operating conditions differences, manufacturing tolerances, damages and degradation. In practice, some mismatch losses occur always. In this thesis, mismatch losses are calculated on a PV module level and the relative mismatch losses are calculated with respect to the sum of the maximum powers of individual modules. PS means conditions in which the cells of a PV system receive non-uniform irradiance levels due to shading. While PS of large-scale PV plants is mainly caused by overpassing cloud shadows, it can also exist due to, inter alia, surrounding objects, snow or soiling. The characteristics of shadings caused by moving clouds are discussed in Chapter 4.

In a parallel connection of PV cells, voltage is the same for all the cells and the cell with the lowest OC voltage limits the total voltage of the parallel connection. The total current of the parallel connection is the sum of the currents of the individual cells. In a series connection, current is the same for all the cells and the total voltage of the series connection is the sum of the voltages of the individual cells. The cell with the lowest SC current limits the total current of the series connection. If the current of the series connection is higher than the SC current of a shaded cell, the cell will be reverse-biased and act as a load. Then, part of the power generated by the other cells is dissipated to heat in the shaded cell. Dissipation of power in the shaded cell may lead to a phenomenon called hot-spot heating and to damaging of the cell.

Hot-spot heating can be avoided by bypass diodes which are connected in anti-parallel with certain number of PV cells. The number of cells is chosen so that hot-spots cannot be formed. Due to bypass diodes, a group of cells protected by a bypass diode can be reverse-biased only to the voltage drop at the bypass diode. In the point where the bypass diode starts to conduct, the reverse voltage of the cell group equals to the threshold voltage of the bypass diode and the current is a bit higher than the SC current of the shaded cell. The amount of the current of the series connection exceeding this biasing point is diverted through the bypass diode. Thus, the bypass diode prevents the increase of the power dissipated in the shaded cell. Bypass diodes also reduce the mismatch losses of series-connected PV cells. The use of a bypass diode for each PV cell guarantees the best protection but it increases the cost of PV modules and is far from indispensable (Häberlin, 2012; Roche et al., 1995). If only one cell is shaded, the complete cell group protected by a bypass diode is bypassed. In that case, the cell group is reverse-biased to the voltage drop at the bypass diode. Thus, the shaded cell is reverse-biased to that voltage plus the generating capability of the other cells of the group (Wenham et al., 2007). Under normal operating conditions, bypass diodes do not conduct and thus induce no power loss. However, when a bypass diode is conducting, some power is lost. Schottky diodes have been typically used as bypass diodes, but also controllable switches, which have lower power losses, can be used (Acciari et al., 2011; Pulvirenti et al., 2012). Due to bypass diodes there can be multiple maximum power points in the *I–U* curves of PV modules. That makes MPPT more complicated.

The operation of series and parallel connections of PV modules under PS is illustrated by an example involving an unshaded and a shaded PV module. The irradiance levels received by the unshaded and shaded module are 1000 and 250 W/m^2, respectively, and the temperature of the modules is 25 °C. The modules are identical and protected by three bypass diodes. The *I–U* and *P–U* curves of the modules, their series connection and their parallel connection are presented in Figs. 2.9 and 2.10, respectively.

The effect of bypass diodes is clearly visible in Figs. 2.9 and 2.10. When the current of the series connection is larger than the current of the point where the bypass diodes of the shaded module start to conduct, the voltage of the series connection is the voltage of the unshaded module minus the voltage drop in the conducting bypass diodes and the power of the series connection is somewhat less than the power of the unshaded module. When the current of the string is smaller than the current of that point, the bypass diodes of the shaded module are not conducting. In this region, the voltage of the series connection is the sum of the voltages of the unshaded and shaded module. As can be seen in Figs. 2.9 and 2.10, the series connection has two MPPs. Under non-uniform conditions a PV system can have at most as many MPPs as

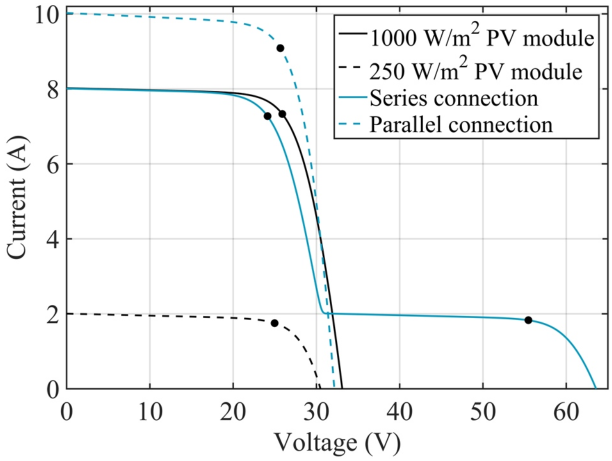

Figure 2.9. Current–voltage curves of an unshaded and a shaded PV module and their series and parallel connections. MPPs are marked with black dots. The temperature of the modules is 25 °C.

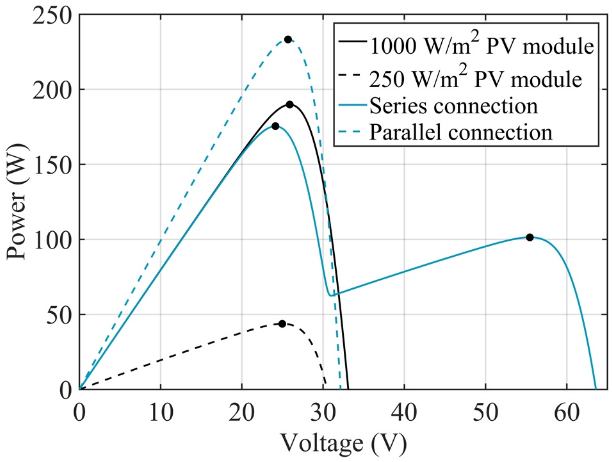

Figure 2.10. Power–voltage curves of an unshaded and a shaded PV module and their series and parallel connections. MPPs are marked with black dots. The temperature of the modules is 25 °C.

there are bypass diodes in the system. The MPP with the largest power is called the global MPP.

In the above example, the relative mismatch losses of the series and parallel connection are 24.9% and 0.16%, respectively. So, the mismatch losses of the series connection are over 150 times larger than those of the parallel connection. The reason for the big difference in mismatch losses between the series and parallel connection is the fact that the MPP current I_{MPP} changes significantly (over 75%) between the irradiance levels of 1000 and 250 W/m^2 while the MPP voltage changes only slightly (less than 4%). The behaviour of the MPP current and voltage of a PV cell as a function of irradiance is presented in Fig. 2.11. The effect of the irradiance on the MPP current and voltage is almost similar than on the SC current and OC voltage (see Fig. 2.6). The MPP current increases almost linearly with the increasing irradiance. However, the increase is substantially slower at irradiance values lower than 25 W/m^2 or so. The MPP voltage increases rapidly with the irradiance up to about 40 W/m^2 and is almost constant at the irradiance values higher than 400 W/m^2.

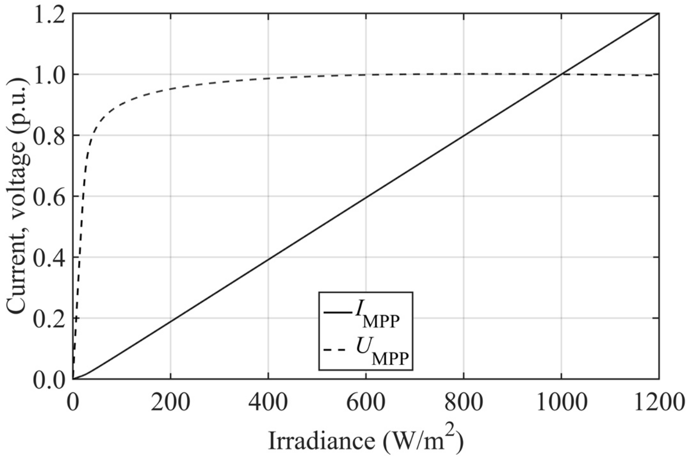

Figure 2.11. MPP current and voltage of a PV cell as a function of irradiance. The current and voltage are relative to the values at 1000 W/m^2. The temperature of the cell is 25 °C.

Due to manufacturing tolerances, the *I–U* curves of PV cells are not completely identical. Thus, the maximum power of a series connection of PV cells is always lower than the sum of the maximum powers of the individual cells. Manufacturers of PV modules try to minimise that kind of mismatch losses by incorporating into a PV module only cells whose I_{MPP} is as similar as possible. Mismatch losses caused by manufacturing tolerances have been studied, e.g. in Bishop (1988), Chamberlin et al. (1995), Lorente et al. (2014) and Massi Pavan et al. (2015).

The mismatch losses of series and parallel connections of PV modules are further demonstrated by discussing the above-presented scenario of a shaded and an unshaded PV module when the number of unshaded modules is increased. The relative mismatch losses of the series and parallel connection as a function of the number of modules in the connection are presented in Figs. 2.12 and 2.13, respectively. In the above-presented scenario, the mismatch losses of the string were the sum of the maximum power of the shaded module and the losses in the bypass diodes of the module. As the length of the string increases, only the part of the mismatch losses that is due to the losses in the bypass diodes increases. Thus, the absolute mismatch losses of the string increase slowly and the relative mismatch losses of the sting decrease with the increasing length of the string. Also the relative mismatch losses of the parallel connection decrease with the increasing number of modules in parallel. Moreover, the difference between the mismatch losses of the series and parallel connection decreases with the increasing number of modules in the connections. In the case of Figs. 2.12 and 2.13, the mismatch losses of the series connection are over 100 times larger than those of the parallel connection. While the mismatch losses of parallel connections are much smaller compared to series connections, par-

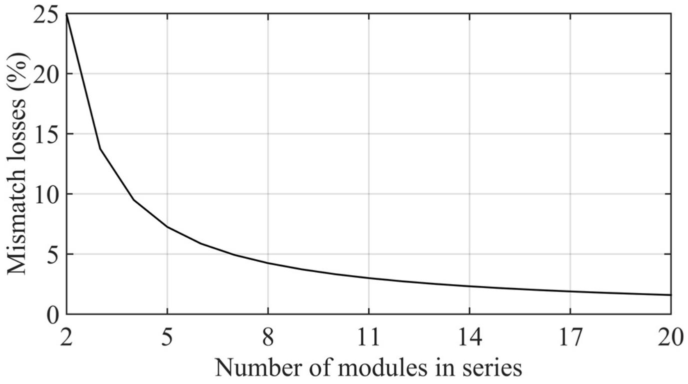

Figure 2.12. Relative mismatch losses of a PV string as a function of the number of PV modules in series when one of the modules is shaded (250 W/m^2) and the rest are unshaded (1000 W/m^2). The temperature of the modules is 25 °C.

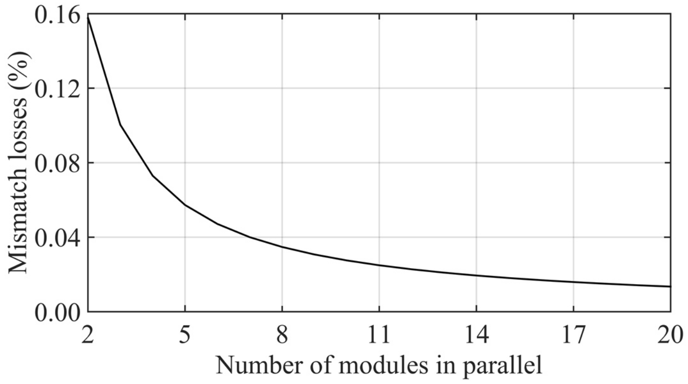

Figure 2.13. Relative mismatch losses of a parallel connection of PV modules as a function of the number of modules in parallel when one of the modules is shaded (250 W/m^2) and the rest are unshaded (1000 W/m^2). The temperature of the modules is 25 °C.

allel connections have a drawback of having higher currents. Due to higher currents compared to series connections, resistive losses are larger in parallel connections of PV modules and bigger cable diameters are needed.

2.6 Photovoltaic power systems

PV power systems can be divided into stand-alone and grid-connected systems. Stand-alone PV systems are independent of electrical grids, whereas grid-connected PV systems are power plants feeding their energy into electrical grids. Since there is a need to convert the direct current (DC) output of PV modules to alternating current (AC), which is used in most of the electrical grids, inverters are used to interface PV modules with an electrical grid. The main tasks of an inverter interfacing a PV array with a grid are to inject a sinusoidal current into the grid and to ensure that the array is operated at its global MPP. Various inverter topologies for interfacing PV modules to the grid are presented in Fig. 2.14.

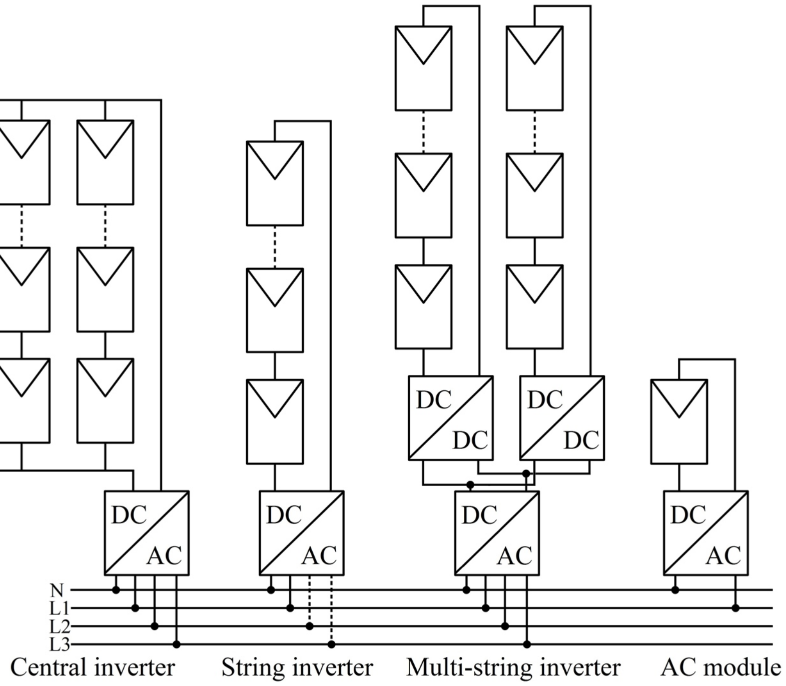

Figure 2.14. Inverter topologies of grid-connected PV systems.

The central inverter topology, widely utilised in the past, is based on a centralised inverter that interfaces a large number of PV modules to the grid. The modules are usually connected in series, to achieve a higher voltage level and thus avoid further voltage amplification, and the series connections are connected in parallel. String diodes wired in series in each string can be used to prevent reverse currents. However, string diodes are mainly used in relatively large PV arrays with numerous parallel strings (Häberlin, 2012). The central inverter topology is the lowest cost solution for megawatt-scale PV systems since large inverters have a low price per power ratio. The other benefit of this topology is simple maintenance (Picault et al., 2009). However, the central inverter topology has several drawbacks such as power losses due to centralised MPPT, mismatch losses between the PV modules, losses in the string diodes, losses and security risks in high voltage DC cables and a nonflexible design where the upgradeability is low and benefits of mass production cannot be reached (Kjaer et al., 2005; Picault et al., 2009).

The string inverter topology is a reduced version of the central inverter topology, where only one string is connected to an inverter. Nevertheless, the input voltage of the inverter may be high enough to avoid voltage amplification. Since every string is controlled individually, mismatch losses and losses due to MPPT are reduced compared to the central inverter topology. Other advantages of the string inverter topology are that there are shorter string wiring runs and no losses associated with string diodes (Kjaer et al., 2005). Thus, the overall efficiency of a system is typically higher compared to the central inverter topology, despite the fact that the efficiency of large inverters is normally higher than that of small inverters. Moreover, system modularity is increased since strings can be added one at a time (Picault et al., 2009). As a drawback, the extra inverters increase the costs of the PV system.

The team concept is a modification of the string inverter topology which aims to improve power conversion efficiency at low irradiance levels. In the team concept, DC switches have been used to cross-connect strings together. Due to these switches, strings can be combined to accept larger irradiance range of PV production and improve conversion efficiency by using only one inverter (Picault et al., 2009).

The multi-string (MS) inverter topology combines the central and string inverter topologies. Every string is interfaced with its own DC–DC converter to a common DC–AC inverter. Every PV module string is controlled individually similarly as in the string inverter topology. The MS inverter topology is easily upgradeable to a certain scale since a new string with a DC–DC converter can be plugged into the existing platform (Kjaer et al., 2005). The major disadvantages of this configuration are high investment costs and low reliability due to two power processing stages (Ahmadi et al., 2011).

The AC module is the integration of a PV module and the inverter into one electrical device. Since there is only one PV module, mismatch losses do not occur between modules but only between the cells of the module. The AC module topology is the most modular and upgradeable solution and it enables very efficient MPPT. The drawbacks of AC modules are high costs and high voltage-amplification, which may reduce the overall efficiency (Kjaer et al., 2005).

Inverter topologies can also be categorised based on the number of power processing stages. A single-stage inverter need to handle all tasks itself such as MPPT, voltage amplification and grid current control (Carrasco et al., 2006; Kjaer et al., 2005). In dual-stage inverter topologies a DC–DC converter performs MPPT and maybe voltage amplification and the DC–AC inverter controls the grid current. The above presented multi-string inverter is an example of a dual-stage inverter topology. The central inverter, string inverter and AC module topologies are usually realised as single-stage inverter topologies but can also be realised by using two power processing stages.

As mentioned earlier, a PV array of centralised inverter topology is usually composed of several PV module strings connected in parallel with each other. This electrical PV array configuration is commonly known as the series-parallel (SP) configuration. In the SP configuration, system operation monitoring is easy because currents can be measured in individual strings. In the event of a malfunction, the failed string can be simply disconnected and the fault can be localised and repaired without interrupting the operation of the intact strings (Häberlin, 2012).

Alternative PV array configurations like total-cross-tied (TCT), bridge-link (BL) and honeycomb (HC) with additional connections between PV module strings have been proposed to reduce the effects of PS. In the TCT configuration, groups of parallel-connected modules are connected in series. In the BL and HC configurations, half of the interconnections between the strings in the TCT configuration are removed. The BL and HC configurations have the advantage of having fewer interconnections than TCT thus reducing the wiring time and cost of the installation. The electrical connections for the SP, TCT, BL and HC array configurations are presented in Fig. 2.15.

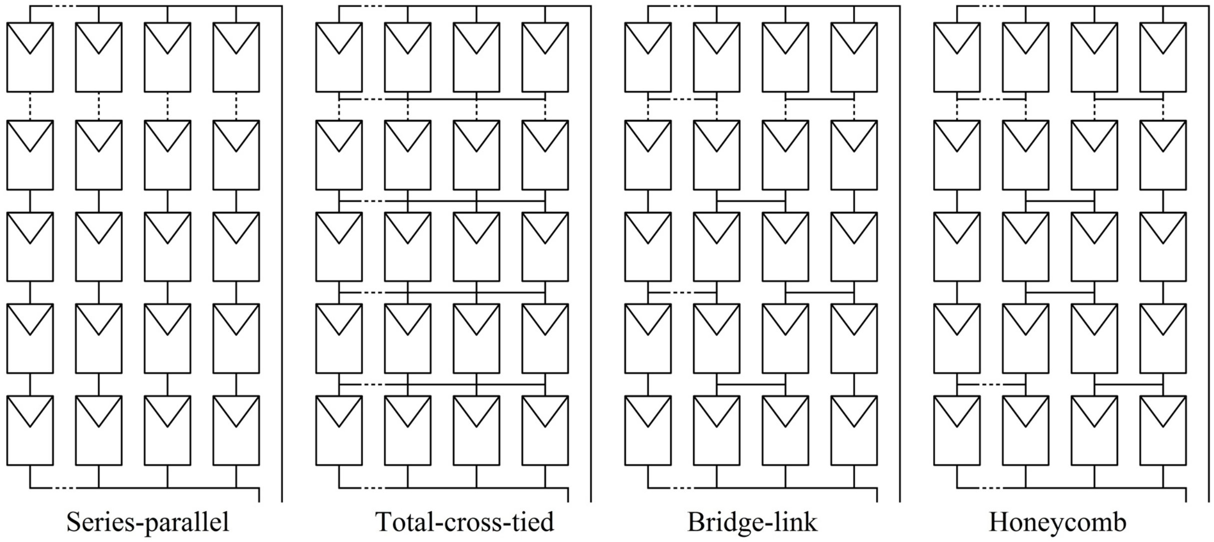

Figure 2.15. Electrical PV array configurations used with centralised inverter topology.

The addition of loops in an array increases redundancy in the circuit. That enables strings to have different current values flowing through the modules of the same string. Thus, loops partly balance out asymmetries of modules. Belhachat and Larbes (2015), Villa et al. (2012) and Wang and Hsu (2011) have presented that the TCT, BL and HC configurations have better performance under PS than the traditional SP configuration. One of the main disadvantages of array topologies with loops is the difficulty of malfunction localisation. They are also more expensive than the SP configuration.

In addition to the electrical PV array configurations presented in Fig. 2.15, several other configurations have been developed. For example, Yadav et al. (2016 and 2017) have proposed SP-TCT, BL-TCT and BL-HC configurations which are combinations of the SP, TCT, BL and HC configurations. Moreover, dynamic PV array reconfiguration has been studied, e.g. in Balato et al. (2016), Nguyen and Lehman (2008), Shams El-Dein et al. (2013b) and Tabanjat et al. (2015). The aim of dynamic PV array reconfiguration is to increase the power output of a PV array by dynamically changing the connections between the modules of the array. By dynamically reconfiguring the connections between the PV modules, mismatch losses can be reduced and MPPT can be improved, thus increasing the power production of the array. On the other hand, the required switches and sensors increase the complexity and costs of the system.

Static PV array reconfiguration is an approach where the physical locations of the modules of a PV array are changed without changing the electrical connections of the modules. This aims to disperse shadings over the array. The predefined arrangement of the modules is designed so that the shading effect is minimised for a variety of shading patterns. There has been a lot of research focusing on the static reconfiguration of PV arrays in recent years, e.g. Belhaouas et al. (2017), Potnuru et al. (2015), Rakesh and Madhavaram (2016), Sahu et al. (2016), Shams El-Dein et al. (2013a), Vijayalekshmy et al. (2016) and Yadav et al. (2016), and several different array arrangements of the TCT configuration have been proposed. The static reconfiguration of other electrical PV array configurations has also been studied, e.g. in Yadav et al. (2017).

3 CHARACTERISATION OF SHADOWS OF MOVING CLOUDS

This chapter presents the methods used to determine the characteristics of shadows of moving clouds. First, methods to identify irradiance transitions and shading periods in measured irradiance data are presented. These methods have been presented earlier in Lappalainen and Valkealahti (2015a and 2016b), respectively. After that, a mathematical model of irradiance transitions caused by moving clouds, presented earlier in Lappalainen and Valkealahti (2015a), is presented. The use of the LCE method presented by Bosch et al. (2013) to determine the speed and direction of movement of shadows from the time lags between shading of a set of three irradiance sensors is introduced. In the last section of the chapter, a method to determine apparent shadow edge velocity is presented. The method is a simplification of the LCE method and is presented earlier in Lappalainen and Valkealahti (2016c).

3.1 Identification of irradiance transitions

Full-time irradiance recordings were analysed to identify irradiance transitions caused by moving clouds. A decreasing irradiance transition is called a fall and an increasing transition is called a rise, similarly as in Tomson (2013). In order to be resistant to small insignificant irradiance fluctuations, the method to identify irradiance transitions identifies rough starting and ending points of irradiance transitions from a moving average of five seconds. Transitions were identified when the moving average of irradiance changed more than 2.5 W/(m^{2}s). A sampling frequency of 1 Hz was used in the rough identification to ensure reasonable computing time. Thereafter, for the sake of accuracy, more exact points for the start and end of the irradiance transition were searched from the vicinity of rough points from the data measured with a sampling frequency of 10 Hz. Equally high sampling frequency has not been used earlier in comprehensive analysis of irradiance transitions. The final point is the maximum (start of a fall or end of a rise) or minimum (end of a fall or start of a rise) irradiance within 0.5 s from the initial rough point.

An example of the identification of an irradiance transition is shown in Fig. 3.1. First, the rough starting point of an irradiance rise is identified in the measurement data at a sampling frequency of 1 Hz when the moving average of irradiance increases more than 2.5 W/(m^{2}s) (point 1 in Fig. 3.1 (a)). After that, the rough ending point is identified when the increase of the

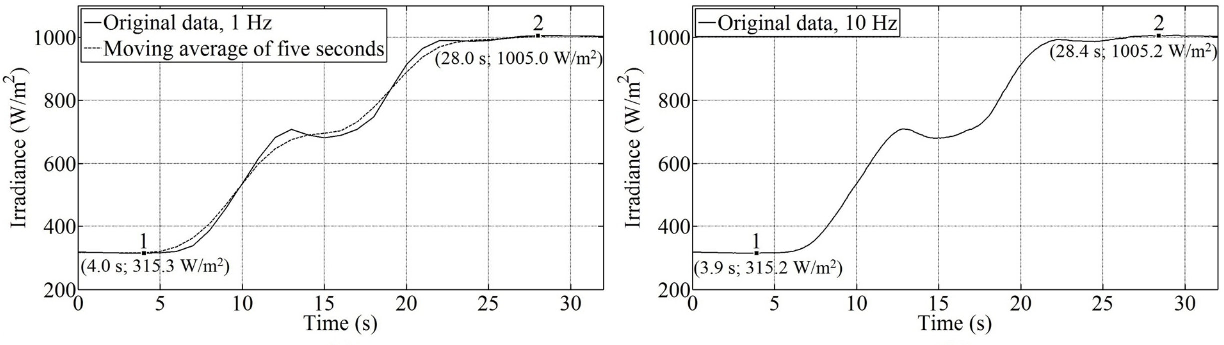

(a) (b)

Figure 3.1. (a) Measured irradiance during an irradiance rise down-sampled to a sampling frequency of 1 Hz and the moving average of five seconds as a function of time. (b) Measured irradiance at a sampling frequency of 10 Hz as a function of time. The identified rough and final starting and ending points are marked with dots in figures (a) and (b), respectively.

moving average is less than 2.5 W/(m^{2}s) (point 2 in Fig. 3.1 (a)). Thereafter, the method uses the original data at a sampling frequency of 10 Hz to find the final points for the start and end (points 1 and 2 in Fig. 3.1 (b)) of the irradiance transition from the vicinity of the rough points.

The shading strength (SS), i.e., the depth of an irradiance change with respect to the irradiance of an unshaded situation, of an irradiance transition was checked to be high enough to identify only irradiance transitions meaningful to the operation of PV generators. SS can be written as

$$\mathrm{SS} = \frac{G_{\mathrm{us}} - G_{\mathrm{s}}}{G_{\mathrm{us}}}, \tag{3.1}$$

where G_{us} is the irradiance of an unshaded situation and G_{s} the irradiance under full shading. The limit of minimum acknowledged SS was selected to be 40% because it has been shown in Lappalainen and Valkealahti (2015a) that moving shadows with lower SS have no significant effect on the operation of a PV string, which is the most sensitive PV system layout to PS. Moreover, the results of the overall effect of the mismatch losses caused by moving clouds on the energy production of PV plants, presented in Section 7.4, support this selection. In order to identify all the irradiance transitions with SS higher than the chosen limit, small enough SS limit (4%) was used in the rough identification of the transitions. The operation of the identification method was further confirmed by analysis with several irradiance sensors in Lappalainen and Valkealahti (2014).

3.2 Identification of shading periods

The method to identify irradiance transitions in measured irradiance data presented in the previous section was adapted to identify shading periods. A shading period was identified when an irradiance fall was followed by steady shading and thereafter by an irradiance rise. The three parts of shading periods are presented in Fig. 3.2, where an example of a typical shading period identified in the data of three irradiance sensors is shown.

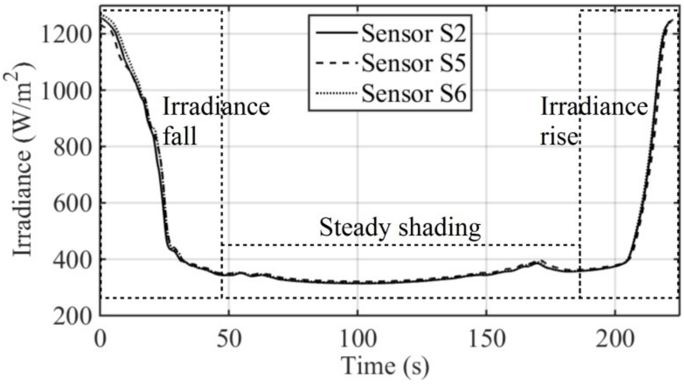

Figure 3.2. Irradiance as a function of time during a shading period measured with irradiance sensors S2, S5 and S6 at a sampling frequency of 10 Hz. For sensor numbers, consult Fig. 4.1. Shading periods measured with different sensors have been shifted to start at the same time.

To ensure that only appropriate shading periods were identified, irradiance during the steady shading period was required to differ less than 50% from the irradiance at the end of the fall and at the beginning of the rise. Also the irradiance difference between the end of the fall and the beginning of the rise had to be less than 30%. The 40% limit of minimum acknowledged SS was applied to both the falls and rises of shading periods. The SS of a shading period is defined as the average of the SSs of the irradiance fall and rise of the shading period.

3.3 Mathematical modelling of irradiance transitions

Irradiance transitions caused by moving clouds were noticed to follow roughly the shape of a sigmoid function which is commonly called an S curve. Irradiance transitions can be modelled with a modified sigmoid function as follows

$$G(t) = \frac{G_{\mathrm{us}} - G_{\mathrm{s}}}{1 + \mathrm{e}^{(t-t_0)/b}} + G_{\mathrm{s}}, \tag{3.2}$$

where G is the irradiance and t the time. Parameter b is related to the sharpness of the transition and parameter t_0 adjusts the transition time defining the midpoint of the transition. The sign of parameter b defines whether the transition is a fall or a rise.

While fitting Eq. (3.2) to measured irradiance data, the final values of the start and end points of the transition defined by the irradiance transition identification algorithm were used to obtain initial parameter values for the fitting. The time between the start and end points defined the duration of the transition and their irradiance values defined the irradiances of the unshaded and shaded situation. The transition identification algorithm was designed so that these values corresponded closely to the constant irradiance levels before and after the transitions. Therefore, to achieve a correct fit to the measured data, constant data at the levels of the final start and end values of an identified transition was added to the beginning and end of the transition, respectively. The length of the added parts of constant data was equal to the initial duration of the transition. Thereafter, parameters G_{us}, G_s, b and t_0 were used to adjust a curve fit to the measured data. In the fitting process, the root-mean-square deviation (RMSD) between the curve fit and the irradiance data was minimised.

3.4 Determination of shadow velocity

The velocity, i.e., speed and direction of movement, of shadows can be determined by using the LCE method presented by Bosch et al. (2013) by analysing the time lags between shading of a set of three irradiance sensors with known locations. In the LCE method, the following three assumptions have been made: the velocity of the shadow while passing over the irradiance sensors is constant, the shadow edge is linear across the sensor array and the shadow covers all the three sensors. For closely placed sensors these assumptions are generally satisfied. A scheme of the LCE method to determine shadow velocity from shading periods measured with sensors S_o, S_a and S_b is presented in Fig. 3.3, where d_a and d_b are the distances between sensor S_o and sensors S_a and S_b, respectively, v the shadow speed, α the angle between the direction of movement of the shadow and the line oa (line from sensor S_o to sensor S_a), θ the angle between the lines oa and ob, δ the angle between the normal to the shadow edge and the direction of movement of the shadow and β the angle between the shadow edge and the line oa.

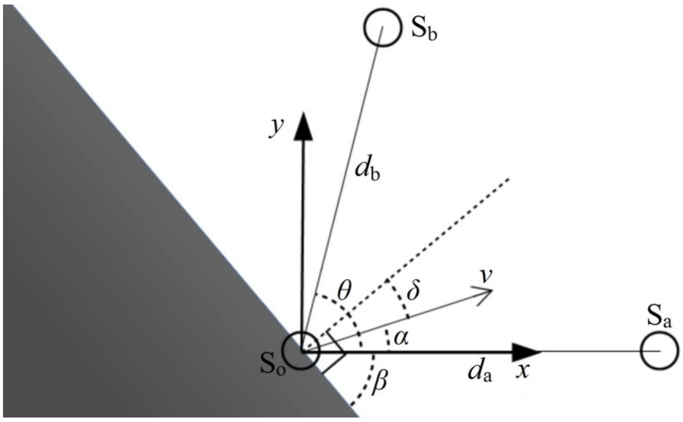

Figure 3.3. Scheme of the Linear Cloud Edge method to determine shadow velocity from a shading period measured with irradiance sensors S_o, S_a and S_b.

Angle α can be calculated from

$$\tan\alpha = \frac{-d_\mathrm{b}(t_\mathrm{a1}-t_\mathrm{a2})\sin\theta}{d_\mathrm{a}(t_\mathrm{b1}-t_\mathrm{b2})-d_\mathrm{b}(t_\mathrm{a1}-t_\mathrm{a2})\cos\theta}, \tag{3.3}$$

where t_a1 and t_b1 are the measured time lags of shading of sensors $\mathrm{S_a}$ and $\mathrm{S_b}$, respectively, after shading of sensor $\mathrm{S_o}$ during the irradiance fall and t_a2 and t_b2 are the corresponding time lags measured during the irradiance rise (Bosch and Kleissl, 2013). Shadow speed v can be written as

$$v = \frac{v_\mathrm{a}v_\mathrm{b}\sin\theta}{v_\mathrm{a}\sin\alpha + v_\mathrm{b}\sin(\theta-\alpha)}, \tag{3.4}$$

where $v_\mathrm{a} = d_\mathrm{a}/t_\mathrm{a1}$ and $v_\mathrm{b} = d_\mathrm{b}/t_\mathrm{b1}$. Shadow speed v can also be calculated by using the time lags measured during the irradiance rise, i.e., $v_\mathrm{a} = d_\mathrm{a}/t_\mathrm{a2}$ and $v_\mathrm{b} = d_\mathrm{b}/t_\mathrm{b2}$. The irradiance fall and rise have the same v and α, but different β. According to Bosch and Kleissl (2013), angle β can be calculated from

$$\tan\beta = \frac{-v_\mathrm{b}\sin\theta}{v_\mathrm{a}-v_\mathrm{b}\cos\theta}. \tag{3.5}$$

In order to define the time lags between shading of a set of three irradiance sensors, shading periods detected by all the three sensors need to be identified. First, a pair of a shading periods detected by two sensors was identified to be caused by the same shadow by the following procedure by utilising the parameters of the fitted sigmoid function of Eq. (3.2) to the identified transitions. The SSs, the unshaded situation irradiances and the durations between the midpoints t_0 of the curve fits of the irradiance falls and rises needed to be within 40% of each other. The values of parameter b and the timestamps of the midpoints of the curve fits of the falls and rises needed to be within 45% and 180 s of each other, respectively. Then, from the shading periods fulfilling these criteria, the period with the lowest RMSD between the curve fits of irradiance transitions measured with the two sensors was selected. Then, the same procedure was repeated for the shading periods identified in the measurement data of the third sensor and finally a shading period detected with all the three sensors was identified. Thereafter, the defined midpoints t_0 of irradiance falls and rises were used to obtain the time lags between shading of the three sensors.

In order to ensure that the same shadow was identified in the measurement data of all the three sensors, 15% of the unshaded situation irradiance was employed as the upper limit for the mean RMSD of the three shading periods. This limit finally ensures that the depth, duration and overall shape of the shading periods identified by the three sensors are closely identical and, accordingly, they are most likely caused by one overpassing cloud. RMSD between two irradiance transitions was calculated throughout the length of the shorter transition by shifting the transitions to start at the same time and RMSD between two shading periods was calculated as the average of the RMSDs of the falls and rises of the shading periods.

The edge of a cloud shadow is, naturally, somewhat irregular and each shadow is unique. There are irregular irradiance fluctuations especially in the beginning and end of irradiance transitions. Moreover, cloud enhancement can cause rapid increase of irradiance at the beginning of a fall or at the end of a rise (Yordanov et al., 2013). Irregular irradiance fluctuations in the beginning and end of irradiance transitions can cause uncertainty on the identification of the exact start and end points of the irradiance transitions. Thus, the values at the midpoint of the curve fit of each transition were used in the identification of shading periods detected by all the three sensors and in the determination of the time lags. In this way the most irregular parts of irradiance transitions were avoided, the shading periods detected by all the three sensors were identified consistently and the time lags between shading of the sensors were determined reliably.

In Lappalainen and Valkealahti (2016b), the above presented method and another method based on the direct analysis of the measurement data were used in the identification of shading periods detected with all the three sensors and in the determination of the time lags and the results achieved by these two methods were compared. The results show that the application of the curve fits of Eq. (3.2) works well for obtaining the time lags between cloud shading of the three sensors compared to the direct analysis of the measurement data. The use of the curve fits mitigates the effects of irregularities present on shadow edges, such as cloud enhancement of irradiance and other minor fluctuations of optical origin.

The presented method required a considerable amount of adjustment and testing of the criteria of various parameters used in the identification of shading periods detected by all the three sensors and there was no way to directly verify the correctness of the selected criteria. Although the absolute proof of the correctness of the presented method is infeasible, its functionality can be assessed based on the outcome and with respect to the other method presented in Lappalainen and Valkealahti (2016b). The results were checked to be in line with other analyses done for the same dataset (Lappalainen and Valkealahti, 2015b).

Riehl (1962) has presented that the maximum wind speed in jet streams is near 300 knots. Although the speed of a cloud shadow may differ from the speed of the cloud, that value can be considered as the maximum speed of cloud shadows. Thus, 150 m/s was employed as the upper limit of shadow speed and the shadows with higher derived speed were rejected.

3.5 Determination of apparent shadow edge velocity

The developed method to determine apparent shadow edge velocity, i.e., the component of shadow velocity normal to the shadow edge, is a simplification of the LCE method. Apparent velocity for falling and rising shadow edges can be determined from the time lags between shading of a set of three irradiance sensors with known locations by using the same three assumptions than in the LCE method (see Section 3.4). A scheme of the method to determine apparent shadow edge velocity from irradiance transitions measured with sensors S_o, S_a and S_b is presented in Fig. 3.4, where v_e is the apparent shadow edge speed, γ the angle between the line oa and the normal to the shadow edge and E_a and E_b are the apparent shadow edge points that would pass over sensors S_a and S_b if the shadow moved to the direction of its edge normal. In the method, the possible movement of a shadow parallel to its edge is ignored, because it has no visible or actual effect in the scope of the assumptions used in this study.

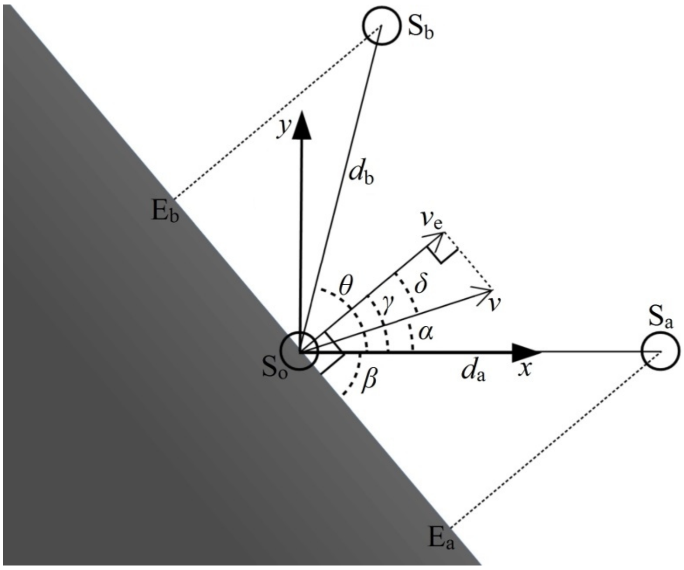

Figure 3.4. Scheme of the method to determine apparent shadow edge velocity from an irradiance transition measured with sensors S_o, S_a and S_b.

The main vectors in the Cartesian coordinate system of Fig. 3.4 needed to determine the apparent shadow edge velocity can be expressed as

$$\begin{aligned}
\boldsymbol{v} &= (v\cos\alpha,\ v\sin\alpha)\\
\boldsymbol{v}_\mathrm{e} &= (v_\mathrm{e}\cos\gamma,\ v_\mathrm{e}\sin\gamma)\\
\boldsymbol{r}_\mathrm{a} &= (d_\mathrm{a},\ 0)\\
\boldsymbol{r}_\mathrm{b} &= (d_\mathrm{b}\cos\theta,\ d_\mathrm{b}\sin\theta)\\
\hat{\boldsymbol{c}} &= (\cos\beta, \sin\beta),
\end{aligned} \tag{3.6}$$

where $\boldsymbol{r}_\mathrm{a}$ and $\boldsymbol{r}_\mathrm{b}$ are the position vectors from sensor S_o to sensors S_a and S_b, respectively, and $\hat{\boldsymbol{c}}$ is an unitary vector in the direction of the shadow edge.

Position vectors $\boldsymbol{r}_\mathrm{a}$ and $\boldsymbol{r}_\mathrm{b}$ can be expressed as

$$\begin{aligned}
\boldsymbol{r}_\mathrm{a} &= \boldsymbol{r}_{\mathrm{E_a}} + t_\mathrm{a}\boldsymbol{v}_\mathrm{e}\\
\boldsymbol{r}_\mathrm{b} &= \boldsymbol{r}_{\mathrm{E_b}} + t_\mathrm{b}\boldsymbol{v}_\mathrm{e},
\end{aligned} \tag{3.7}$$

where $\boldsymbol{r}_{\mathrm{E_a}}$ and $\boldsymbol{r}_{\mathrm{E_b}}$ are the position vectors from sensor S_o to shadow edge points E_a and E_b and t_a and t_b are the time lags it takes from the shadow to shade sensors S_a and S_b after shading sensor S_o. Applying the cross product with $\hat{\boldsymbol{c}}$ to Eqs. (3.7) leads to

$$\boldsymbol{v}_\mathrm{a} \times \hat{\boldsymbol{c}} = \boldsymbol{v}_\mathrm{e} \times \hat{\mathbf{c}} \tag{3.8a}$$

$$\boldsymbol{v}_\mathrm{b} \times \hat{\boldsymbol{c}} = \boldsymbol{v}_\mathrm{e} \times \hat{\boldsymbol{c}}, \tag{3.8b}$$

where $\boldsymbol{v}_\mathrm{a} = \boldsymbol{r}_\mathrm{a}/t_\mathrm{a}$ and $\boldsymbol{v}_\mathrm{b} = \boldsymbol{r}_\mathrm{b}/t_\mathrm{b}$. Eqs. (3.8a) and (3.8b) can be solved as

$$\boldsymbol{v}_\mathrm{a} \times \hat{\boldsymbol{c}} = \boldsymbol{v}_\mathrm{b} \times \hat{\boldsymbol{c}}. \tag{3.9}$$

Angle β can be solved from Eq. (3.8a) as

$$\tan\beta = \frac{-v_\mathrm{e}\sin\gamma}{v_\mathrm{a} - v_\mathrm{e}\cos\gamma} \tag{3.10}$$

and from Eq. (3.9) as

$$\tan\beta = \frac{-v_\mathrm{b}\sin\theta}{v_\mathrm{a} - v_\mathrm{b}\cos\theta}. \tag{3.11}$$

By combining Eqs. (3.10) and (3.11), v_e can be solved as

$$v_\mathrm{e} = \frac{v_\mathrm{a}v_\mathrm{b}\sin\theta}{v_\mathrm{a}\sin\gamma + v_\mathrm{b}\sin(\theta - \gamma)}. \tag{3.12}$$

Angle γ can be written as

$$\gamma = 90^\circ - \beta. \tag{3.13}$$

Identification of irradiance transitions detected by all the three sensors was done by applying the method to identify shading periods detected by all the three sensors presented in the previous section. The SSs, the unshaded situation irradiances and the values of parameter t_0 of the curve fits of the irradiance transitions needed to be within 40% of each other. The values of parameter b and the timestamps of the midpoints of the curve fits needed to be within 45% and 180 s of each other, respectively. In order to ensure that the same shadow edge was identified in the measurement data of all the three sensors, 15% of the unshaded situation irradiance was employed as the upper limit for the mean RMSD of the three irradiance transitions.

In some cases, where a tiny cloud or a small fraction of a cloud is shading the area of the sensors, only one or two sensors of the sensor triplet can identify an irradiance transition. If only two sensors of the sensor triplet identify an irradiance transition, there is a risk that the third sensor identifies another almost similar transition taking place soon before or after. In that kind of situations, the used method might erroneously identify the transitions to be due to the same shadow edge. In such erroneous identifications, one of the timestamps of the shading of the sensors usually differs clearly from the other two timestamps which are close to each other. This results in relatively slow apparent shadow edge speed and apparent movement direction nearly perpendicular to one of the sensor triplet sides. These erroneous identifications were ignored by discarding shadow edges with apparent speed lower than 0.8 m/s and apparent movement direction in 5° range from the directions perpendicular to the sides of the sensor triplet. Further, shadow edges with erroneously high apparent speed (over 150 m/s) were rejected. The same upper limit was used for shadow speed and the reasoning behind this limit is presented in Section 3.4.

The above mentioned erroneous identifications of irradiance transitions could be avoided by using more than one sensor triplet. Unfortunately, the used sensor network did not provide that option. The method presented in the previous section to identify shading periods detected by all the three sensors (movement of shadows) is not as sensitive to that kind of erroneous identifications as is the presented method used to identify apparent movement of single shadow edges, because it utilises both the falling and rising transitions of shading periods. Moreover, shading periods do not occur as often as irradiance transitions, and hence the probability that two almost similar shading periods occur in a given time frame is much lower.

The presented method required a considerable amount of adjustment and testing of the criteria of various parameters used in the identification of irradiance transitions detected by all the three sensors. Corresponding criteria were successfully used to identify shading periods detected by three sensors. The results presented in Lappalainen and Valkealahti (2016b) show that the application of the curve fits of Eq. (3.2) works well for obtaining the time lags between cloud shading of the three sensors compared to the direct analysis of the measurement data.

4 CHARACTERISTICS OF SHADOWS OF MOVING CLOUDS

This chapter presents and discusses the results of the study of the characteristics of shadows of moving clouds. The study was conducted using the methods presented in Chapter 3. In the first section of this chapter, the TUT solar PV power station research plant and the used irradiance measurement data are introduced. After that, the characteristics of irradiance transitions and shading periods are presented, the mathematical model of irradiance transitions is verified and the results of shadow velocity and apparent shadow edge velocity are presented. Finally, correlations between the characteristics of shadows are discussed. Most of the results presented in this chapter have been presented earlier in Lappalainen and Valkealahti (2015a, 2016a, 2016b and 2016c).

4.1 Measurement data

15 months (457 days) of data of the TUT solar PV power station research plant (Torres Lobera et al., 2013) measured by irradiance sensors S2, S5 and S6 with a sampling frequency of 10 Hz was analysed. The chosen dataset contains all the months of the years 2011–2014 with good summer time insolation conditions for PV power production from which comprehensive measurements (over 95% of the time) are available. Good insolation conditions during the chosen period enhance the applicability of the results to other locations. Data of winter months was not used due to weak insolation conditions and possible snow cover. During the chosen period, the solar noon air mass was lower than 2.4.

The used sensor triplet was chosen so that the irradiance sensors are closely placed at the same altitude and form approximately a right-angled triangle. The used irradiance sensors were photodiode-based SP Lite2 pyranometers (Kipp&Zonen) mounted with a tilt angle of 45° from the horizontal plane and oriented nearly towards due south. The used irradiance sensors were shaded due to a nearby building in the morning during the studied period. However, the effects of shadings due to the building on the presented results are not significant. Furthermore, occasional shadings may have occurred due to other reasons than clouds like the actions of humans and birds. However, the probability of these cases can be assumed to be minimal compared to shadings due to clouds. The description of the used sensor triplet is presented in Table 4.1. The used irradiance sensors have been marked on the layout scheme of the TUT solar PV power station research plant presented in Fig. 4.1. The research plant contains a mesh of irradiance and module temperature sensors providing detailed information on the operating conditions of PV modules. The analyses of identified irradiance transitions and shading periods are based on the measurement data of sensor S5. The data of the sensor triplet formed by sensors S2, S5 and S6 was used to analyse shadow movement and the apparent movement of shadow edges.

Table 4.1. Description of the used sensor triplet. Consult Fig. 4.1 for sensor numbers.

Sensor S_o	S2
Sensor S_a	S5
Sensor S_b	S6
d_a	5.84 m
d_b	7.12 m
θ	87.69°

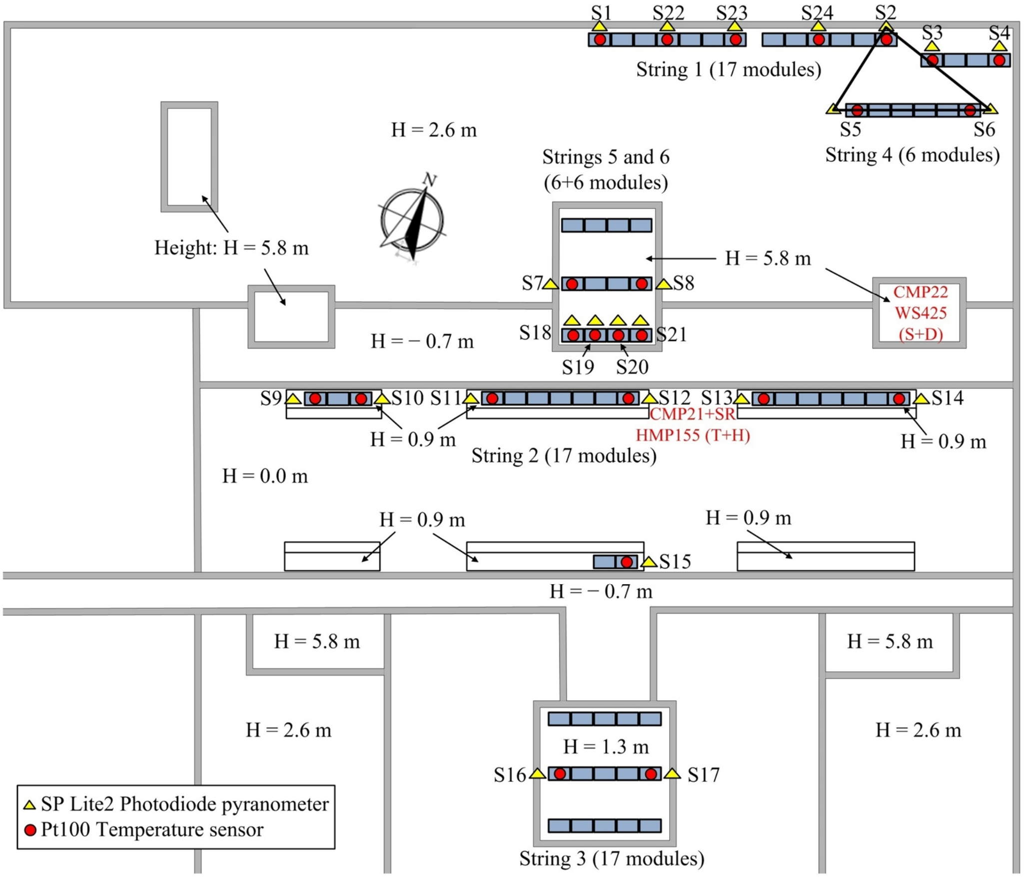

Figure 4.1. Layout scheme of the TUT solar PV power station research plant. The used sensor triplet is marked with a black triangle on the top right corner.

4.2 Characteristics of irradiance transitions

By using the irradiance transition identification method presented in Section 3.1 and a 10% limit for minimum SS, a total of 140,018 irradiance transitions, consisting of 69,688 falls and 70,330 rises, were identified in the data measured with sensor S5. Only one identified fall and one rise were clearly caused by some other reason than a moving cloud and were rejected. The relative numbers of the identified falls and rises are presented as a function of the limit of minimum acknowledged SS in Fig. 4.2. The relative number of the identified irradiance transitions decreases with the increasing SS limit. As can be seen in the figure, most of the clouds are optically quite thin causing only slight attenuation of irradiance. The two lines in Fig. 4.2 are, in practice, on top of each other meaning that there are no considerable differences between the numbers of the identified falls and rises. This is an expected result, since an irradiance fall due to a shadow of a moving cloud is mostly followed by an irradiance rise when the shadow moves away. However, this is not always the case which explains the small difference between the numbers of the identified falls and rises. At the same time, this shows that the developed identification method of irradiance transitions works quite systematically.

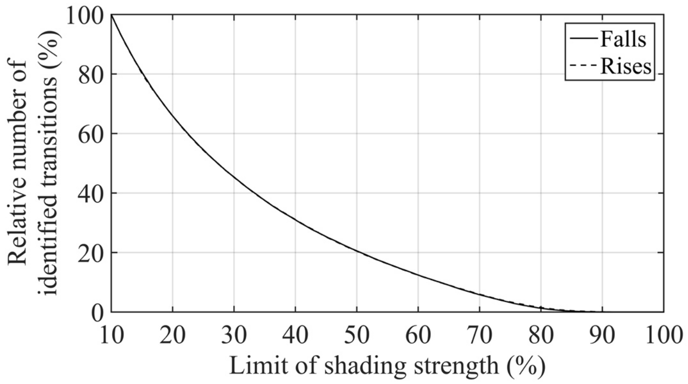

Figure 4.2. Relative numbers of identified irradiance falls and rises as a function of the limit of minimum acknowledged shading strength.

When the 40% limit for minimum SS was used, a total of 43,456 irradiance transitions, consisting of 21,592 falls and 21,864 rises, were identified. The monthly numbers, average SSs and average durations of the identified falls and rises have been compiled in Table 4.2. The maximum number of irradiance transitions occurring during one month was 4420 on July 2012 and the minimum number was 1450 on April 2014. The mean monthly number was around 2900. However, clear trends in the monthly numbers of the irradiance transitions cannot be observed. Only spring months (April and May) appear to have less irradiance transitions than summer (June, July and August) or autumn (September), which is in line with common experience on the local weather. In the rest of this chapter, the 40% limit of minimum acknowledged SS is used, i.e., only the irradiance transitions with SS of over 40% are discussed.

Table 4.2. Monthly numbers, average shading strengths and average durations of the identified irradiance falls and rises.

Year	Month	Number of falls	Number of rises	Average SS of falls (%)	Average SS of rises (%)	Average duration of falls (s)	Average duration of rises (s)
2011	8	1656	1690	56.90	56.41	17.75	20.31
2011	9	1252	1266	58.01	58.47	18.75	19.53
2012	4	932	929	56.29	56.76	16.21	17.94
2012	5	1660	1713	57.48	57.55	15.84	18.54
2012	6	1610	1646	59.03	58.57	15.86	19.68
2012	7	2185	2235	57.68	57.40	15.87	17.86
2012	9	2096	2105	58.89	59.63	14.31	15.22
2013	5	1158	1178	56.92	56.73	15.84	18.93
2013	6	1737	1756	57.82	57.83	16.05	19.05
2013	7	1778	1832	56.89	56.89	14.70	16.35
2013	8	1710	1689	59.06	59.18	15.90	17.50
2013	9	924	934	57.23	57.18	19.50	20.80
2014	4	721	729	55.05	54.80	20.53	21.12
2014	5	1153	1127	57.95	58.69	17.26	19.61
2014	6	1020	1035	55.92	55.77	19.01	22.15
Total		21,592	21,864	57.62	57.66	16.49	18.61

The distributions of the numbers of identified irradiance falls and rises in a day are presented in Fig. 4.3. The number of days decreases with the increasing number of transitions in a day. The maximum number of identified transitions in a day was 900, consisting of 449 falls and 451 rises, on June 18th 2012. On the other hand, there were less than 10 transitions during 125 out of 457 days and 55 days with no identified transitions. These days were either almost or fully clear sky or overcast days. The mean number of irradiance transitions occurring during one day was 95.1 and the median 49.

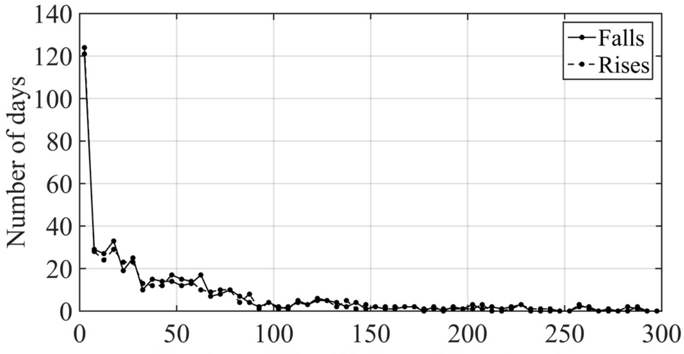

Figure 4.3. Distributions of the numbers of identified irradiance falls and rises in a day.

The largest observed SS was 95.0% for both the falls and rises. When the 40% limit of minimum acknowledged SS was used, the average SS was 57.6% and 57.7% for the falls and rises, respectively. The distributions of the SS for all the identified irradiance falls and rises are presented in Fig. 4.4. No major differences existed between the irradiance falls and rises. The SS was more than 90% only in 0.1% of all the transitions and more than 80% in 4.5% of the cases. In 90% of the transitions, the SS was lower than 75.4%. As can be seen from Table 4.2, the monthly average SS has no clear trend.

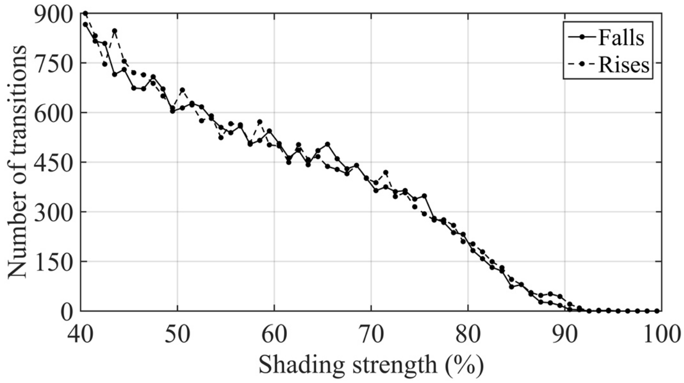

Figure 4.4. Distributions of the shading strength of all the identified irradiance falls and rises.

The distributions of the irradiance of an unshaded situation for all the identified irradiance falls and rises are presented in Fig. 4.5. Only minor differences existed between the identified irradiance falls and rises. The mean values of the irradiance of the unshaded situation for the falls and rises were both about 727 W/m^2. The unshaded situation irradiance was from 600 to 1000 W/m^2 in about 50% of all the identified transitions. This indicates that a major part of irradiance transitions takes place around noon.

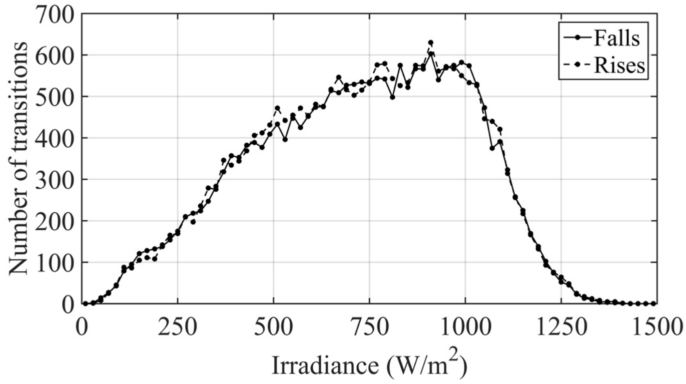

Figure 4.5. Distributions of the unshaded situation irradiance of all the identified irradiance falls and rises.

The duration of the irradiance transitions varied from 1.0 to 290.2 s and from 1.3 to 217.3 s for the falls and rises, respectively. So, a transition can happen in a second or it can take several minutes. The average durations of the falls and rises were 16.5 and 18.6 s, respectively. The total time taken by all the transitions was about 212 h and, on the average, almost half an hour in a day. The distributions of the duration for all the identified irradiance falls and rises are presented in Fig. 4.6. Only 2.3% of all the transitions were longer than 60 s and 0.4% longer than 120 s. In all, 90% of the transitions were shorter than 33.4 s. The monthly average duration of the transitions (see Table 4.2) has no clear trend either.

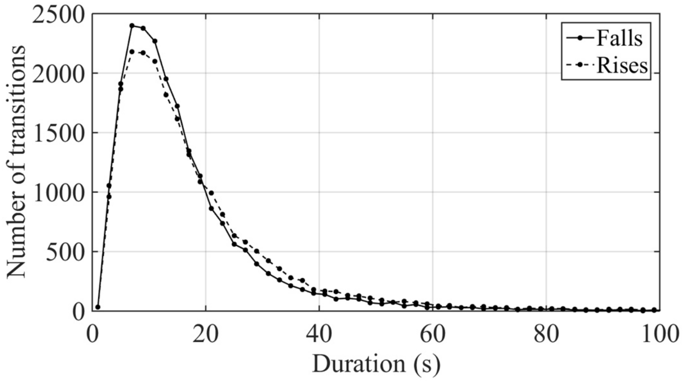

Figure 4.6. Distributions of the duration of all the identified irradiance falls and rises.

The maximum instantaneous rates of change of irradiance during the transitions were 4534 and 4448 W/(m^{2}s) for the falls and rises, respectively. Thus, irradiance transitions caused by moving clouds can be very fast. However, the average rate of change of irradiance during all the transitions was 26.2 W/(m^{2}s). The relative average rate of change of irradiance with respect to instantaneous irradiance was 5.5 %/s.

The distributions of the solar hour angle, i.e., time from the solar noon in degrees, in the beginning of all the identified irradiance falls and rises are presented in Fig. 4.7. For 78.4% of the transitions, the solar hour angle was between –50° and 50°. The largest number of transitions took place around the solar noon, which is typically the hottest period of the day with the highest solar irradiance, and the number of transitions distributed quite symmetrically around it. The lowest observed solar hour angle of an irradiance transition was –87° and the largest 115°. The used irradiance sensor was shaded due to a nearby building in the morning during the studied period. Therefore, the irradiance transitions with solar hour angle lower than –87° were not

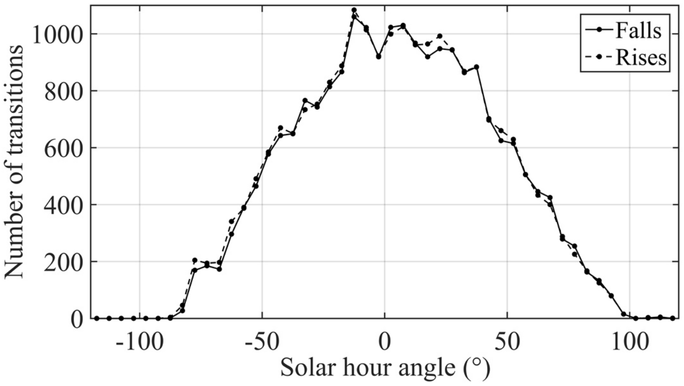

Figure 4.7. Distributions of the solar hour angle in the beginning of all the identified irradiance falls and rises.

detected. However, irradiance transitions were identified within a solar hour angle span of over 200°. Thus, during some of the transitions, the sun was shining from behind the used irradiance sensor.

The distributions of the solar elevation angle in the beginning of all the identified irradiance falls and rises are presented in Fig. 4.8. The smallest observed solar elevation angle was 2.43° and the largest 51.95°, which is near the maximum value of solar elevation angle on the latitude of Tampere. Solar elevation angle was higher than 30° for 74.3% of the transitions. The distributions of the solar elevation angle of the irradiance falls and rises in Fig. 4.8 are in line with the distributions of the solar hour angle in Fig. 4.7. The main finding from Figs. 4.7 and 4.8 is that irradiance transitions were mostly observed around the noon when the solar elevation angle and the received irradiance are the highest.

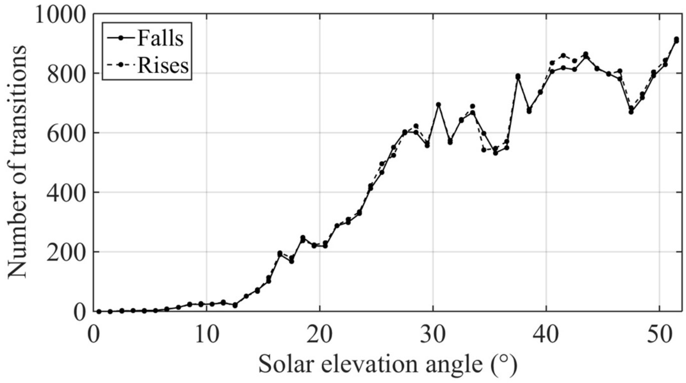

Figure 4.8. Distributions of the solar elevation angle in the beginning of all the identified irradiance falls and rises.

In conclusion, only minor differences existed between the studied characteristics of the identified irradiance falls and rises. The only noticed remarkable difference was that the average duration of the irradiance rises was clearly longer than that of the falls. However, there were only small differences between the duration distributions of the falls and rises. The shapes of the distributions of all the other studied characteristics were almost identical for the falls and rises.

4.3 Parameters of the mathematical model of irradiance transitions

The distributions of the SS for all the identified irradiance falls and rises based on the curve fits of Eq. (3.2) are presented in Fig. 4.9. There were no major differences between the distributions of the SSs obtained by the curve fitting or directly from the measurements (Fig. 4.4) but they were the same within the statistical accuracy. The average SSs for the falls and rises based

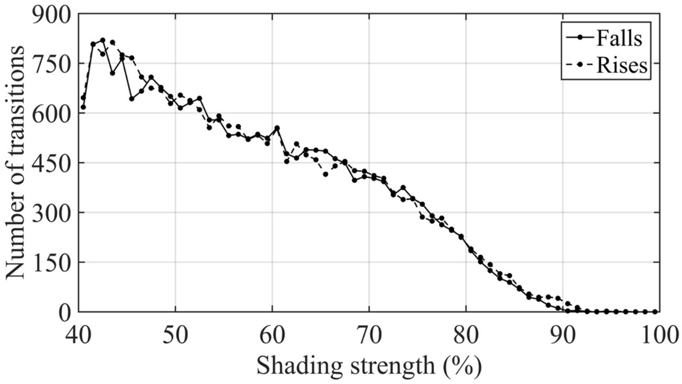

Figure 4.9. Distributions of the shading strength of all the identified irradiance falls and rises based on the curve fits of Eq. (3.2).

on the curve fitting were 57.7% and 57.8%, respectively. These values are very close to those defined directly from the measured values of the identified transitions.

The SSs based on the curve fitting differ a little bit from those based directly on the measured irradiance data since the values of the irradiance in shaded and unshaded situations were not fixed for the fit. Therefore, some curve fits achieved slightly lower or higher SS than was initially obtained based on the experimental data and the distributions in Fig. 4.9 differ slightly from the corresponding distributions in Fig. 4.4. Accordingly, some curve fits of the transitions just over the 40% limit of minimum acknowledged SS (according to the initial identification) provided SSs slightly below 40%. That is why the first values of the distributions in Fig. 4.9 are lower than in Fig. 4.4. The distributions of the relative difference between the SSs based on the curve fitting and on the measured values with respect to the latter for all the identified irradiance falls and rises are presented in Fig. 4.10. There are only negligible differences in the distributions between the falls and rises. The average differences for the falls and rises were only 0.91% and 0.90%, respectively. As can be seen in Fig. 4.10, the SS of an irradiance transition based on the curve fitting tends to be a bit higher than the experimental value.

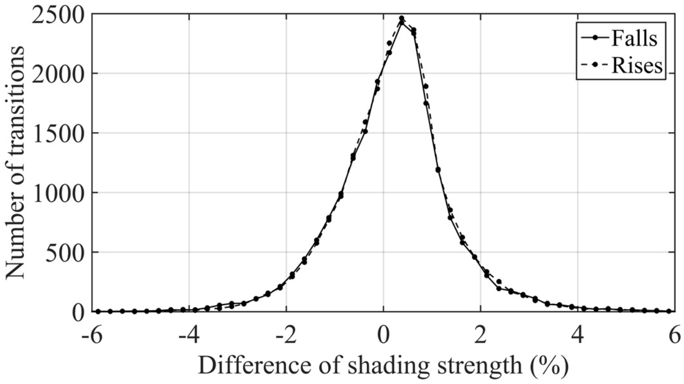

Figure 4.10. Distributions of the relative difference between the shading strengths based on the curve fits of Eq. (3.2) and on the measured values for all the identified irradiance falls and rises.

Parameter *b* is related to the steepness of irradiance transitions, so that an irradiance transition is the sharper the smaller is the absolute value of parameter *b*. Around half of the irradiance change of a curve fit happens during a time span of 2.2 times the absolute value of *b* around the midpoint of the transition. The sign of parameter *b* defines whether the transition is a fall (positive values) or a rise (negative values). The distributions of the obtained absolute value of *b* for all the identified irradiance falls and rises are presented in Fig. 4.11. There are only minor differences in the distributions between the falls and rises. However, small absolute values of *b* were more frequent for the falls than for the rises. The average value of parameter *b* was 1.84 and –2.10 s for the falls and rises, respectively. These differences between the falls and rises are in line with the finding presented in Section 3.2 that the average duration of the rises was longer than that of the falls. Parameter *b* obtained a lower absolute value than 5 s in 96.0% and 94.4% of all the identified irradiance falls and rises, respectively.

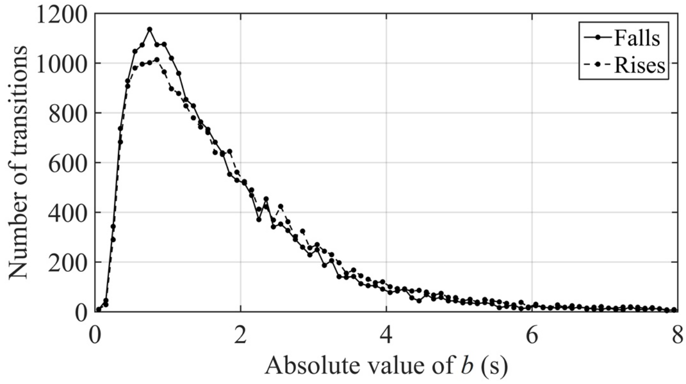

Figure 4.11. Distributions of the obtained absolute value of parameter *b* for all the identified irradiance falls and rises.

The distributions of the relative differences in the irradiance change and the irradiances of the unshaded and shaded situation between the curve fits and the measured transitions with respect to the latter for all the identified irradiance transitions are presented in Fig. 4.12. The

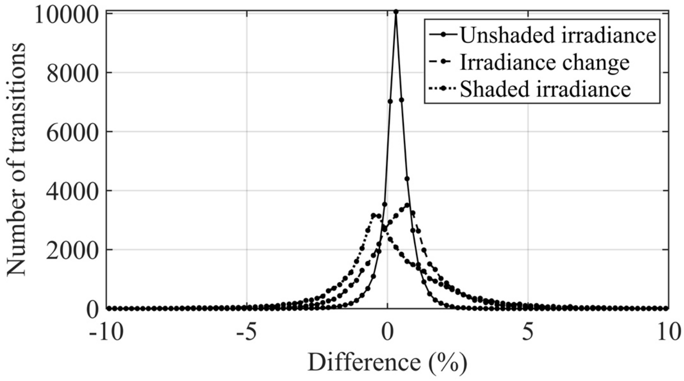

Figure 4.12. Distributions of the relative difference in the unshaded situation irradiance, irradiance change and shaded situation irradiance for all the identified irradiance transitions between the use of the curve fits of Eq. (3.2) and the direct use of the measured values.

differences in all the three variables were small for most of the transitions. The difference in the unshaded situation irradiance was typically smaller than the differences in the other two variables. The absolute value of the relative difference in the irradiance change was smaller than 1% and 3% for 59.1% and 94.6% of all the irradiance transitions. The corresponding proportions for the irradiances of the unshaded and shaded situations were 89.5% and 99.8%, and 53.1% and 88.9%, respectively. The average relative differences for the irradiance change and the irradiances of the unshaded and shaded situations were 1.1%, 0.5% and 1.4%, respectively. Again, there were only negligible differences between the irradiance falls and rises.

As can be seen from Fig. 4.12, the irradiance change based on the curve fitting tended to be a bit higher than the initially identified irradiance change during the transition similarly as the SS in Fig. 4.10. Correspondingly, the irradiance of an unshaded situation of the curve fits was, on the average, larger and the irradiance of a shaded situation smaller than those of the identified transitions. The small differences between the measured irradiance transitions and their curve fits demonstrate that the modified sigmoid function describes the transitions well.

4.4 Accuracy of the mathematical model of irradiance transitions

The accuracy of the curve fits of Eq. (3.2) was further evaluated by RMSD analysis. The distributions of the RMSD of the curve fit to the measured irradiance data for all the identified irradiance falls and rises are presented in Fig. 4.13 (a). The distributions for the falls and rises are almost identical and only minor differences due to the statistical nature of this study can be observed. The average RMSDs for the falls and rises were 11.7 and 11.5 W/m^2, respectively. For 90% of all the irradiance transitions, the RMSD of the curve fit was smaller than 24.5 W/m^2 and the smallest RMSD was around 0.1 W/m^2.

The distributions of the normalised root-mean-square deviation (NRMSD) of the curve fit to the measured irradiance data for all the identified irradiance falls and rises are presented in Fig. 4.13 (b). NRMSD was calculated by normalising RMSD to the range of the observed data, i.e., by dividing the RMSD by the irradiance change during the irradiance transition. Again, the distributions for the falls and rises are almost identical. The largest NRMSDs for the falls and rises were 16.8% and 23.6% and the average NRMSDs 2.7% and 2.6%, respectively. For 90% of all the transitions, the NRMSD of the curve fit was smaller than 5.0%. These NRMSD values indicate that the modified sigmoid function describes the irradiance transition well in most of the cases.

The monthly average RMSDs and NRMSDs of the curve fit for the identified irradiance falls and rises are presented in Table 4.3. Clear trends in the monthly average RMSDs or

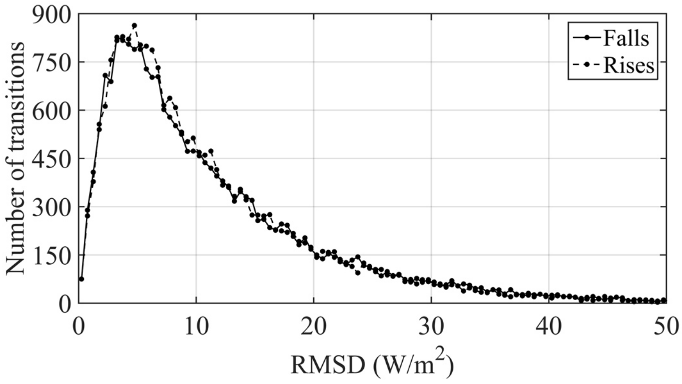

(a)

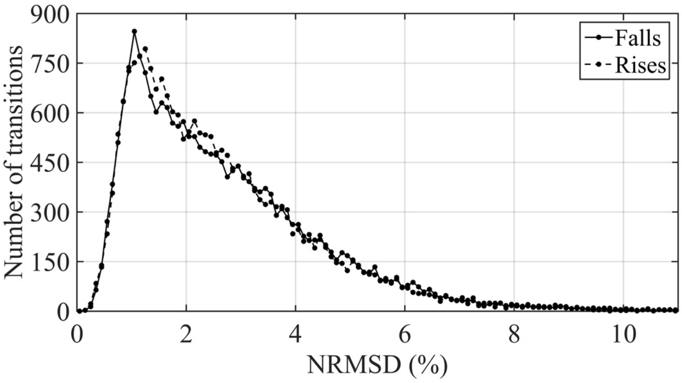

(b)

Figure 4.13. Distributions of RMSD (a) and NRMSD (b) between the measured values and the curve fit of Eq. (3.2) for all the identified irradiance falls and rises.

Table 4.3. Monthly average RMSDs and NRMSDs between the measured irradiance data and the curve fit of Eq. (3.2) for the identified irradiance falls and rises.

Year	Month	Average RMSD for falls (W/m^2)	Average RMSD for rises (W/m^2)	Average NRMSD for falls (%)	Average NRMSD for rises (%)
2011	8	12.37	11.37	2.70	2.55
2011	9	11.24	10.89	2.79	2.70
2012	4	13.26	13.81	2.97	3.04
2012	5	11.35	11.18	2.52	2.51
2012	6	12.62	12.07	2.58	2.54
2012	7	12.34	11.56	2.79	2.66
2012	9	11.91	12.08	2.90	2.92
2013	5	11.47	11.13	2.57	2.49
2013	6	11.41	10.90	2.59	2.53
2013	7	12.20	12.11	2.78	2.80
2013	8	11.01	11.26	2.60	2.63
2013	9	9.25	8.66	2.51	2.39
2014	4	9.85	9.33	2.63	2.48
2014	5	12.32	12.19	2.75	2.73
2014	6	11.92	11.85	2.59	2.66
Total		11.75	11.46	2.69	2.65

NRMSDs of the curve fits cannot be observed. This demonstrates that the shape of the irradiance transitions seems to be independent of the time of the year.

Two examples of identified irradiance transitions and the curve fits of Eq. (3.2) to the measured data are presented in Fig. 4.14 to demonstrate the feasibility of the mathematical irradiance transition model. In Fig. 4.14 (a), the curve fit has a typical RMSD of 15.2 W/m^2 and NRMSD is 1.8%. For about 75% and 38% of all the identified transitions, the RMSD and NRMSD, respectively, was smaller than this. In Fig. 4.14 (b), an example of an accurate curve fit with RMSD of 1.6 W/m^2 and NRMSD of 0.3% is presented. For about 4% of the transitions, the RMSD is even lower than this. These examples demonstrate that the mathematical model of Eq. (3.2) describes the overall behaviour of irradiance transitions due to moving clouds quite realistically in the majority of the cases. Although the characteristics of irradiance transitions caused by moving clouds vary a lot, most of the transitions can be modelled accurately by using the parameters based on measured irradiance values. Thus, the use of the model is not regionally bounded and the model can be applied globally. Only in a tiny number of cases the mathematical model fails to describe the irradiance transition properly. In these cases, there are typically substantial irradiance fluctuations during the transition.

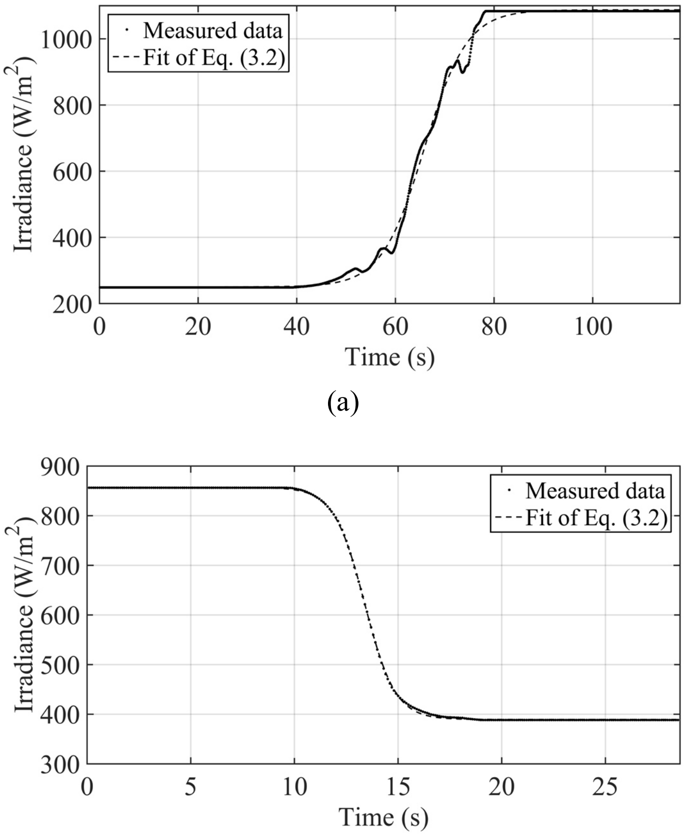

(a)

(b)

Figure 4.14. Two examples of identified irradiance transitions and the curve fits of Eq. (3.2) to the measured data.

4.5 Characteristics of shading periods

The total number of shading periods identified in the irradiance data of sensor S5 was 11,899. Only one of the identified periods was clearly caused by some other reason than a moving cloud and was rejected. As presented in Section 3.2, the criteria of various parameters were used in the identification of shading periods in order to identify only shading periods caused by moving clouds. The 40% minimum limit of SS was applied to select only shading periods meaningful to the operation of PV generators. Therefore, the results represent only the shading periods selected for this study, not shading periods caused by clouds in general.

The maximum number of shading periods occurring during one month was 1256 on September 2012 and the minimum number was 364 on April 2014. The mean monthly number was 793. However, clear trends in the monthly numbers of the shading periods cannot be observed. Only spring months appear to have less shading periods than summer or autumn similarly as was in the case of irradiance transitions (Section 4.2). The monthly average SS of the shading periods varied only marginally around the mean value of 59.5% without clear trends. Similarly, the monthly average duration of the shading periods varied around the mean value of one minute without any observable annual trend.

The maximum number of identified shading periods in a day was 326, on June 18th 2012. On the other hand, there were less than 10 shading periods during 220 out of 457 days and 108 days with no identified shading periods, which were either almost or fully overcast or clear sky days. The mean number of shading periods occurring during one day was 26.0 and the median 10. These results mean that the daily time of shading periods varied from zero to over five hours with a mean daily time close to half an hour, when the average duration of the shading periods is taken into account.

The distribution of the SS for all the identified shading periods is presented in Fig. 4.15. When the 40% limit of minimum acknowledged SS was applied, the average SS was 59.5%. The average SSs of the falls and rises of the identified shading periods were 59.6 and 59.3%, respectively. The largest observed SS was 95.0%. As can be seen in Fig. 4.15, majority of the SSs are located around or below the average value with a tail in the distribution on high SSs. This means that very dark clouds leading to SSs over 70 to 80% are quite rare and clouds with high transparency occur more often. The SS was more than 90% only in 0.1% and more than 80% in 3.9% of all the identified shading periods. In 90% of the shading periods, the SS was lower than 74.5%. The relative number of shading periods with SS of slightly over 40% in Fig. 4.15 is smaller than in Fig. 4.4 where corresponding distributions are presented separately for irradiance falls and rises. The reason for the difference is that the 40% minimum limit of SS was applied to both the falls and rises of the shading periods. The shading periods where the SS of the fall was over 40% and the SS of the rise was below 40%, or vice versa, were ignored.

For the same reason, the average SSs of the shading periods and their falls and rises were little higher than reported for the irradiance falls and rises in Section 4.2.

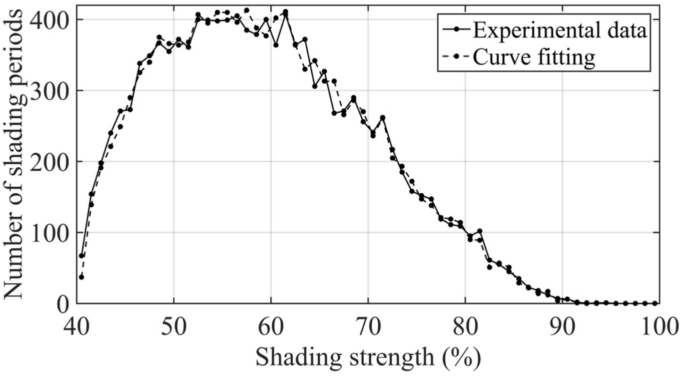

Figure 4.15. Distributions of the shading strength of all the identified shading periods based on the experimental data and on the curve fits of Eq. (3.2).

The distribution of the SS for all the identified shading periods is also presented in Fig. 4.15 based on the values achieved by the curve fitting. As presented earlier, the SSs based on the curve fitting can differ from those based directly on the experimental data because the values of the irradiance in shaded and unshaded situations were not fixed. Thus, some curve fits achieved slightly lower or higher SSs than were initially identified based on the experimental data. However, one can notice that there are no major differences between the distributions obtained by these two methods. The average SS of the identified shading periods based on the curve fitting was 59.6% which is very close to the one based on the measured values showing that the modified sigmoid function describes the irradiance transitions very well in accord with the direct analysis of the experimental data.

The difference in SS between the irradiance falls and rises for all the identified shading periods with respect to the SS of the shading period, i.e., the average of the SSs of the irradiance fall and rise, is presented in Fig. 4.16. For 70% of the shading periods, the difference in the SS between the fall and rise was lower than 18.9%, and the mean difference was 14.5%. As presented earlier, the differences in the SS between the falls and rises is the reason why the number of the shading periods in Fig. 4.15 decreases strongly with the decreasing SS below 50%.

The duration of the identified shading periods varied from 4.2 to 4900 s, and the average duration was 60.2 s. So, a shading period can happen in five seconds or it can take almost 1.5 h. The distribution of the duration for all the identified shading periods is presented in Fig. 4.17. The total time taken by all the identified shading periods was about 199 h and, on the average, almost half an hour in a day. 89% of the shading periods were shorter than 120 s and only around 0.6% of the shading periods were longer than 10 min. In 52.5% of the shading periods, the rise lasted longer than the fall. That finding is in line with the result of Section 4.2 that the duration of the irradiance rises is typically longer than that of the falls.

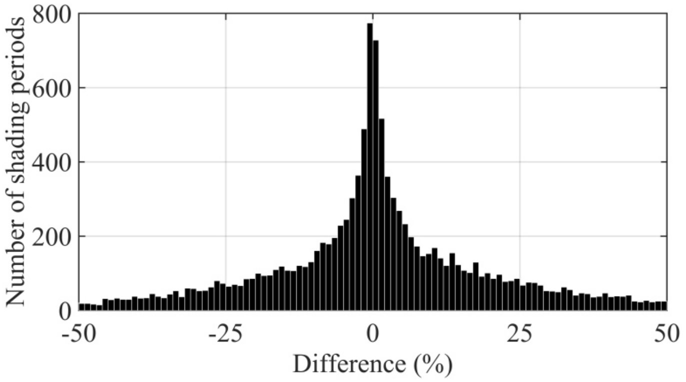

Figure 4.16. Distribution of the difference in the shading strength between the falls and rises of all the identified shading periods.

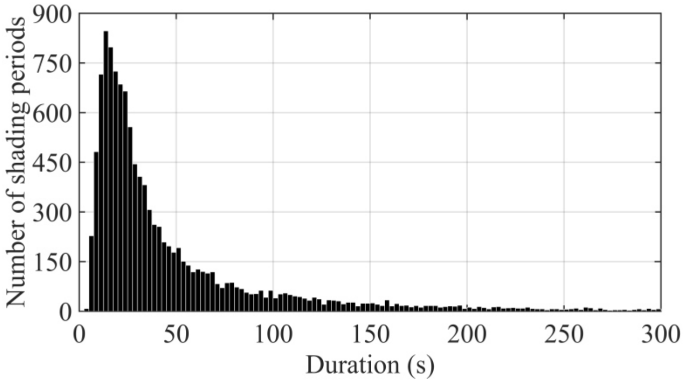

Figure 4.17. Distribution of the duration of all the identified shading periods.

The distribution of the solar hour angle in the beginning of all the identified shading periods is presented in Fig. 4.18. The shape of the distribution is almost similar than in the case of irradiance transitions in Fig. 4.7. The solar hour angle was between –50° and 50° for 79.8% of the shading periods. The largest number of shading periods took place around the solar noon. The lowest observed solar hour angle of a shading period was –83° and the highest 114°. As pre-

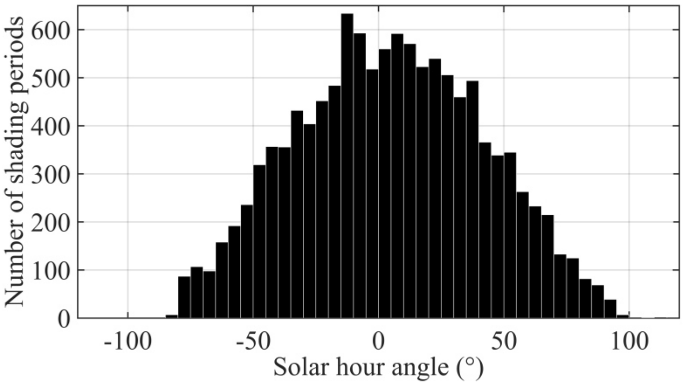

Figure 4.18. Distribution of the solar hour angle in the beginning of all the identified shading periods.

sented earlier, the used irradiance sensor was shaded due to a nearby building in the morning during the studied period, and thus the shading periods with solar hour angle lower than –83° were not detected.

The distribution of the solar elevation angle in the beginning of all the identified shading periods is presented in Fig. 4.19. Also the shape of the distribution of the solar elevation angle is almost similar than in the case of irradiance transitions (Fig. 4.8). The smallest observed solar elevation angle of a shading period was 2.48° and the largest 51.95°. Solar elevation angle was higher than 30° for 75.2% of the shading periods. The distribution of the solar elevation angle is in line with the distribution of the solar hour angle in Fig. 4.18.

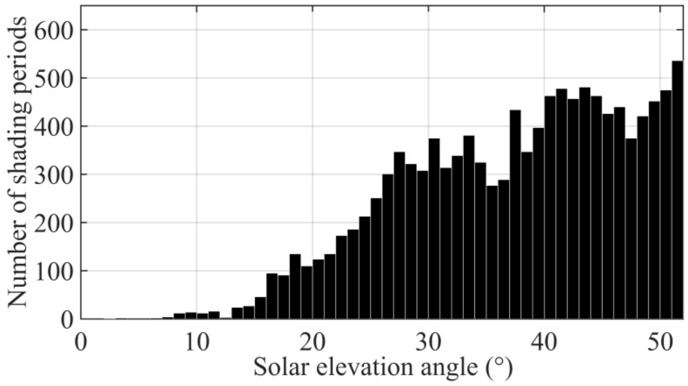

Figure 4.19. Distribution of the solar elevation angle in the beginning of all the identified shading periods.

4.6 Shadow velocity

A total of 7893 shading periods were identified in the measurement data by the sensor triplet formed by sensors S2, S5 and S6. The number of shading periods identified by all the three sensors is considerably smaller than the number of shading periods identified by a single sensor S5. First impression is that the difference is big, but a close look makes it understandable. For example, in some cases where a tiny cloud or a small fraction of a cloud is shading the area of the sensors, only one or two sensors of the sensor triplet can detect a shading period leading to rejection of the shading period for the determination of the shadow velocity. As presented in Section 3.4, the same criteria were applied independently for the shading periods identified by the three sensors and small differences in the measured irradiances could easily lead to rejection of a shading period identified by one of the sensors. 89 identified shading periods were rejected because of erroneously high speed.

The speed of shadows varied greatly being between 5 and 20 m/s for 81.0% of all the identified shadows. The average speed of shadows was 13.1 m/s. The distribution of the speed for all the identified shadows is presented in Fig. 4.20.

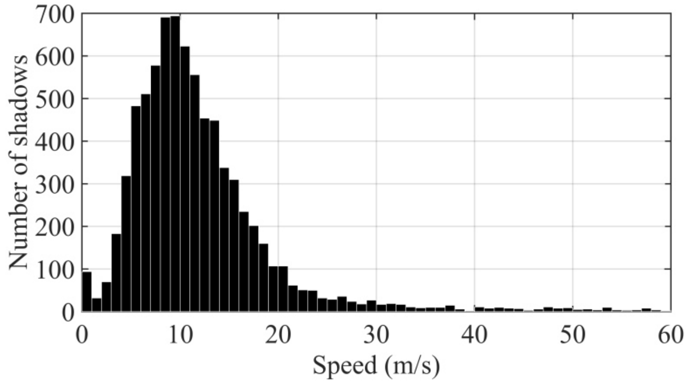

Figure 4.20. Distribution of the speed of all the identified shadows.

The polar histogram of the direction of movement for all the identified shadows is presented in Fig. 4.21. The angles indicate the direction in which the shadows are going. The dominant movement direction of the shadows was towards the directions from north-east to east. The share of the shadows moving towards the directions from north to south-east (angle from 0° to 135°) was 71.2%. This is in line with local knowledge of wind blowing commonly from south-west directions in the Tampere region on summer time. The more detailed distribution of the direction of movement of the shadows is presented in Fig. 4.22.

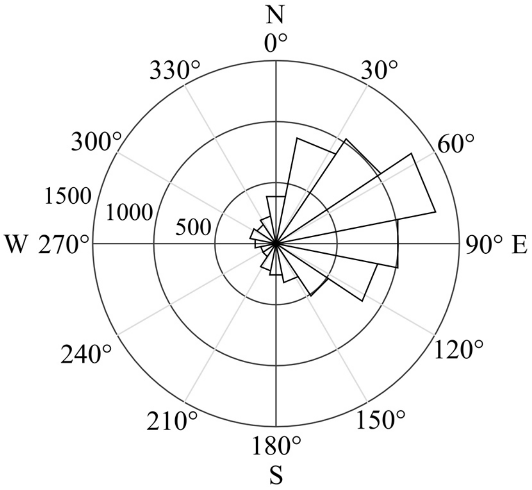

Figure 4.21. Polar histogram of the direction of movement of all the identified shadows.

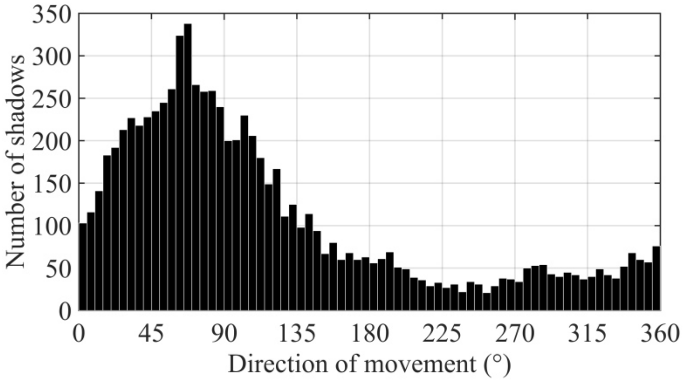

Figure 4.22. Distribution of the direction of movement of all the identified shadows.

4.7 Apparent shadow edge velocity

A total of 27,210 irradiance transitions, consisting of 13,241 falls and 13,969 rises, were identified in the measurement data by all the sensors, S2, S5 and S6, of the used sensor triplet. The numbers of the falls and rises identified by all the three sensors are considerably lower than the numbers identified by a single sensor S5. This is an expected consequence of the used method. As presented earlier, in some cases where a tiny cloud or a small fraction of a cloud is shading the area of the sensors, only one or two sensors of the sensor triplet can notice an irradiance transition leading to rejection of the transition for the determination of the apparent shadow edge velocity. Moreover, the same criteria were applied independently for the irradiance transitions identified by the three sensors and small differences in the transitions could lead to rejection of an irradiance transition identified by one of the sensors. Only one identified transition was rejected because of erroneously high apparent speed.

The distributions of the apparent speed for all the identified falling and rising shadow edges are presented in Fig. 4.23. The overall shape of the distributions is the same. The apparent shadow edge speed varied greatly being lower than 20 m/s in 97.9% and 98.2% of all the falls

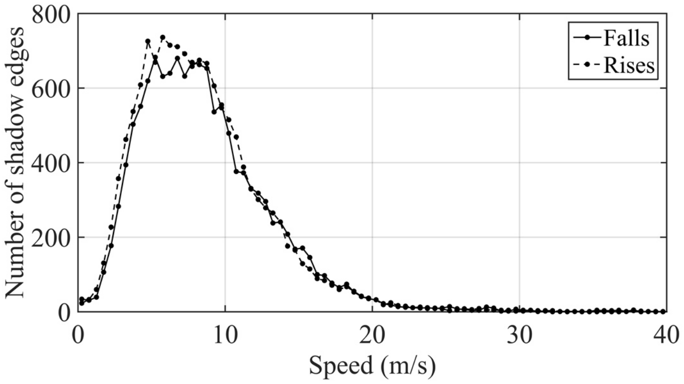

Figure 4.23. Distributions of the apparent speed of all the identified falling and rising shadow edges.

and rises, respectively. The average speed was 8.7 and 8.4 m/s for the falls and rises, respectively. The average apparent speed of shadow edges was roughly two thirds of the average speed of cloud shadows presented in Section 4.6. This difference is essential from the PV system operation point of view since PS of PV generators is actually caused by the apparent movement of shadow edges. Clear trends indicating annual variation in the monthly average apparent speeds of shadow edges cannot be observed.

The polar histograms of the apparent direction of movement for all the falling and rising shadow edges are presented in Fig. 4.24. The histograms are quite similar. The shape of the histograms is also quite similar with the corresponding histogram of the shadow movement in Fig. 4.21. Also the dominant direction of apparent shadow edge movement seems to be towards the directions from north-east to east. The share of the shadow edges moving towards the directions from north to south-east (angle from 0° to 135°) was 65.8% and 65.4% for the falls and rises, respectively. The more detailed distributions of the apparent direction of movement for the falling and rising shadow edges are presented in Fig. 4.25.

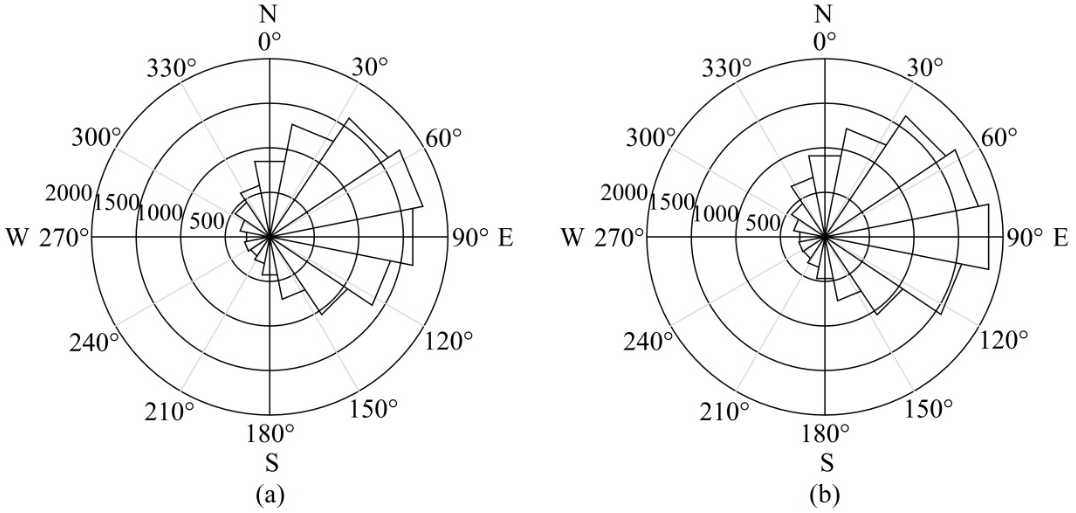

Figure 4.24. Polar histograms of the apparent direction of movement of all the identified falling (a) and rising (b) shadow edges.

The distributions of the apparent direction of movement of the shadow edges are quite similar to the one of the shadow movement presented in Fig. 4.22. The explanation of the differences can be obtained from Fig. 4.26 where the distributions of the angle between the directions of shadow movement and apparent shadow edge movement, i.e. angle δ, for the falling and rising edges of all the identified shadows are presented. The average value of angle δ was 36.0° and 36.7° for the falls and rises, respectively, and the largest observed values were almost 90°. The distributions of angle δ imply that the shadow edge is often distributed along the normal of the shadow velocity. Thus, both the apparent shadow edge movement and the shadow movement must yield quite similar results. However, the wide distribution of angle δ implies that the distributions of the apparent direction of movement of the shadow edges are more

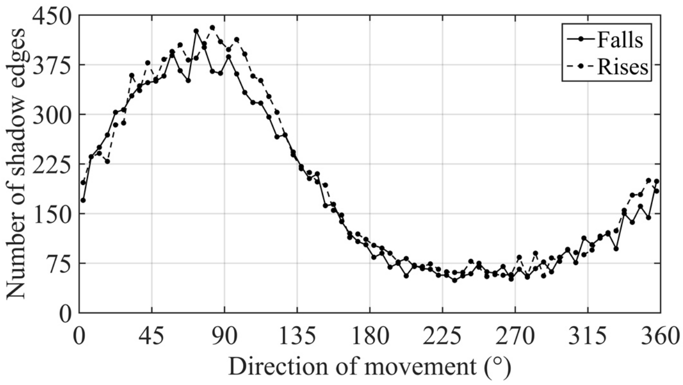

Figure 4.25. Distributions of the apparent direction of movement of all the identified falling and rising shadow edges.

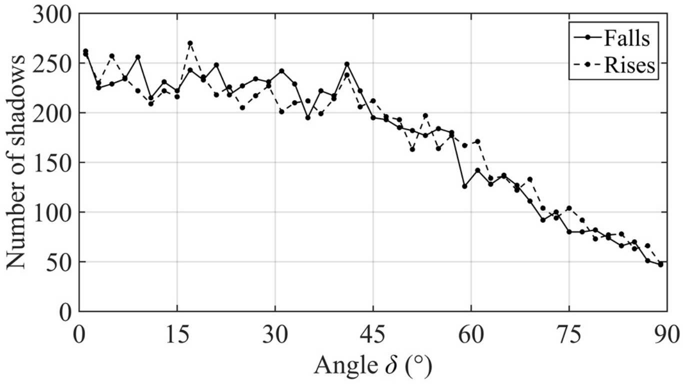

Figure 4.26. Distribution of angle δ of the falling and rising edges of all the identified shadows.

spread out than the corresponding distribution for the shadow movement, which is more concentrated around the directions from north to south-east. The same explanation of the differences can be obtained also from Fig. 8 in Bosch et al. (2013) where the polar histograms for the direction of shadow movement and for angle β are presented. Differences in the speeds and directions of movement between shadows and shadow edges highlight the significance of the use of apparent shadow edge velocity in respectable analyses of the effects of overpassing cloud shadows on the operation of PV power systems.

4.8 Length of shadows and shadow edges

The distribution of the length for all the identified shadows in their direction of movement is presented in Fig. 4.27. Shadow length was calculated by multiplying the mean duration of a shading period defined from the measurements of the three sensors by the shadow speed. The average shadow length was 759 m. From a practical point of view, it is important to notice that the average shadow diameter of almost 1 km means that even the largest PV power plants are widely affected by the shadows. The median shadow length was 315 m and the peak of the length distribution was between 100 and 250 m.

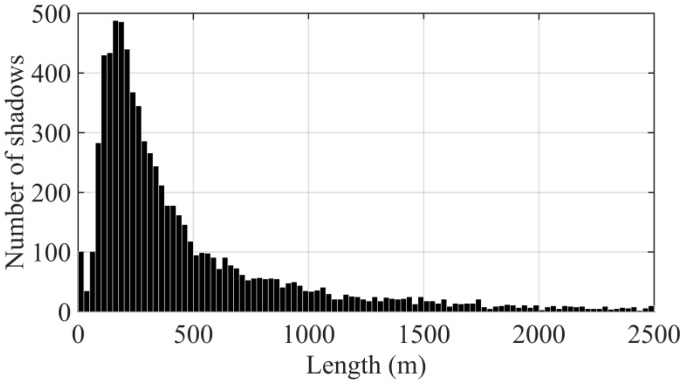

Figure 4.27. Distribution of the length of all the identified shadows in their direction of movement.

The distributions of the length for all the identified falling and rising shadow edges are presented in Fig. 4.28. The maximums of the distributions are around 60 m with long tails at large lengths. The distributions for the falls and rises are in practice similar. The average lengths of the falls and rises were 142 and 146 m and the medians 98 and 106 m, respectively. The small differences in the distributions and average values between the falls and rises are in line with the finding presented in Section 4.2 that the average duration of the rises is longer than of the falls. The average length of the shadow edges was roughly 20% of the average length of shadows in their direction of movement.

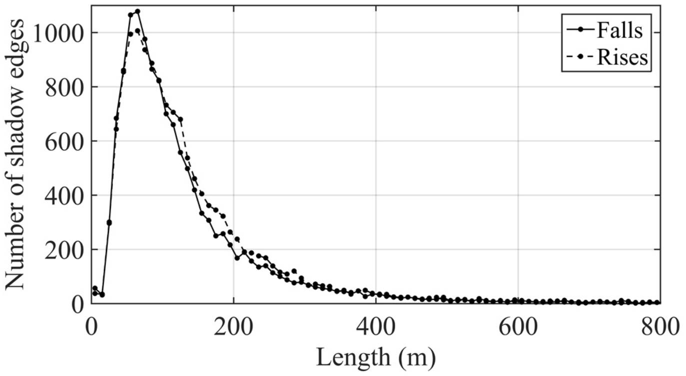

Figure 4.28. Distributions of the length of all the identified falling and rising shadow edges.

From a practical point of view, it is important to notice that an irradiance transition with the average length of almost 150 m can cover a PV array feeding the biggest utility-scale PV inverters. Thus, irradiance transitions with these lengths can cause mismatch losses and other problems on the operation of PV power plants of all sizes. Based on the presented results of the lengths of shadows and shadow edges, it seems evident that the shadows of moving clouds inflict a considerable amount of power fluctuations for the PV power plants of all sizes. It is also evident that the shadows of moving clouds cause gentle irradiance transitions leading typically to only minor irradiance differences between adjacent PV modules. In particular in large-scale PV plants, shadings are mostly caused by moving clouds, and sharp shadows, which are typically caused by nearby objects, can be considered as rare worst-case scenarios.

4.9 Correlation between the characteristics

In this section, the correlations between the SS, duration, parameter *b*, apparent speed and apparent direction of movement of shadow edges were studied. The dependence of these shadow edge characteristics on the time of the day, i.e., solar hour angle, was also studied. The study was based on all of the 27,210 irradiance transitions identified in the measurement data by all the sensors of the used sensor triplet. Moreover, the correlation between the SS and the length of shadows and shadow edges was studied. The mean values of the measurements of the three sensors were used as SS, duration and parameter *b* for each transition. The solar hour angles were calculated for the beginnings of the irradiance transitions as identified by sensor S5.

The knowledge of the existence of correlations between the shadow edge characteristics is essential for the modelling of the shading of PV arrays. By utilising Eq. (3.2), irradiance transitions can be defined using five variables: SS, duration, parameter *b*, apparent speed and apparent direction of movement. If no correlations exist, all the five characteristics are needed to define irradiance transitions. However, if there are strong correlations between some of the characteristics, the irradiance transitions can be defined using fewer characteristics.

The distributions of the SS and parameter *b* for all the irradiance transitions identified in the measurement data by all the three sensors are presented in Figs. 4.29 (a) and (b), respectively. These distributions differ slightly in shape from the corresponding distributions of Figs. 4.4 and 4.11 since in those all the irradiance transitions identified by a single sensor S5 were considered. The same criteria were applied independently for all the irradiance transitions identified by the three sensors. Thus, the SS of the transitions needed to be over the 40% limit based on all the three sensors, i.e., a transition was ignored if its SS was below the limit based on even a single sensor. Because of this, the proportion of transitions with slightly over 40% SS in Fig. 4.29 (a) is remarkable lower than in Fig. 4.4. The median values of the SS, duration, parameter *b* and apparent speed of all the irradiance transitions identified by all the three sensors are presented in Table 4.4. The median values of the SS, *b* and apparent speed were used in the simulations of Chapters 5–7 to represent a typical cloud shadow edge.

The correlation between the absolute value of *b* and the experimentally obtained duration of all the irradiance transitions identified by all the three sensors is presented in Fig. 4.30. The scatter plots for the falls and rises were in broad terms similar. The Pearson correlation coeffi-

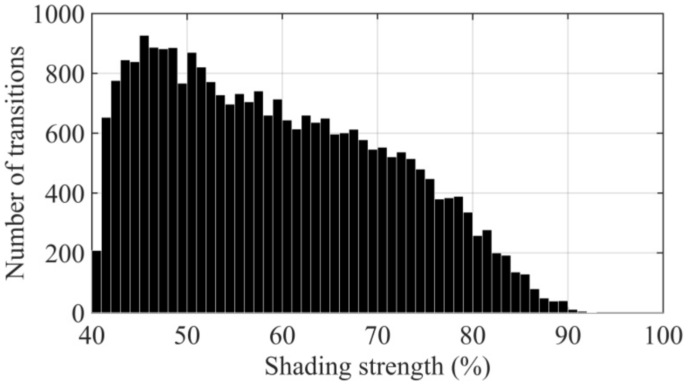

(a)

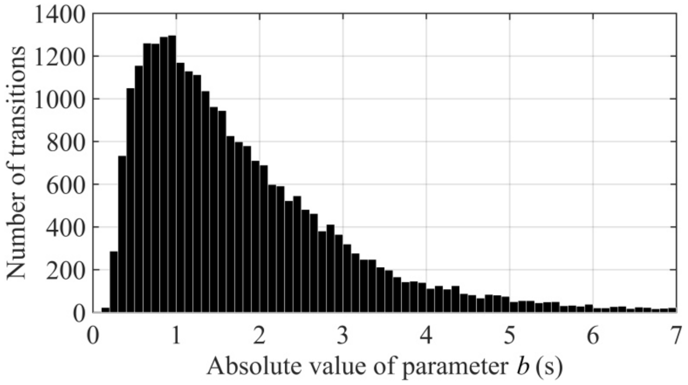

(b)

Figure 4.29. Distributions of the shading strength (a) and parameter *b* (b) of all the irradiance transitions identified by all the sensors of the used sensor triplet.

Table 4.4. Median values of the SS, duration, parameter *b* and apparent speed of all the irradiance transitions identified by all the sensors of the used sensor triplet.

Variable	Value
SS	57.8%
Duration	14.2 s
b	1.48 s
Speed	7.86 m/s

cient (PCC) was 0.806 showing that parameter *b* and the duration of the transitions are closely related. Linear least squares regression for *b* and the experimentally obtained duration led to regression coefficient of 7.67. The linear regression line represents the behaviour of the variables quite well even though the duration values are dispersed especially at small values of *b* as can be seen in Fig. 4.30 (b). The regression coefficients for the falls and rises were 7.48 and 7.84, respectively.

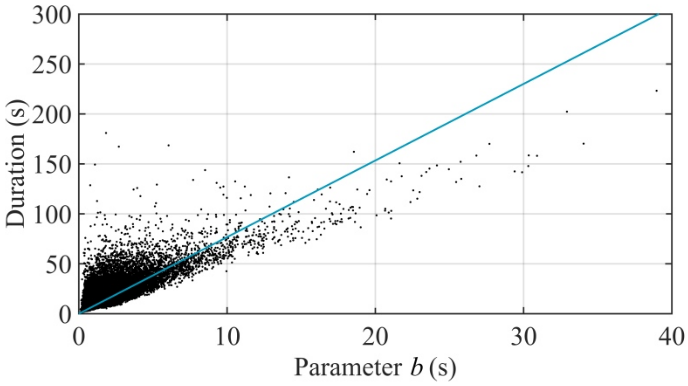

(a)

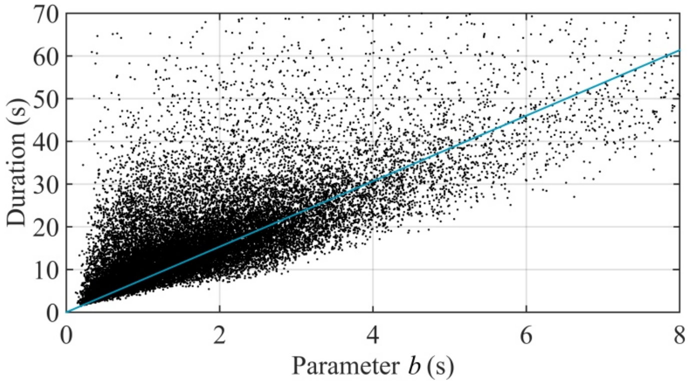

(b)

Figure 4.30. (a) Scatter plot and linear regression line between the absolute value of *b* and the experimentally obtained duration of all the irradiance transitions identified by all the sensors of the used sensor triplet. (b) Blow-up of the plot at small values of *b* and duration.

The scatter plot between the SS and solar hour angle of all the irradiance transitions identified by all the three sensors is presented in Fig. 4.31. As presented earlier, the used irradiance sensors were shaded due to a nearby building in the morning during the studied period, and thus the irradiance transitions with solar hour angle lower than –87° were not detected. The largest observed SS decreased with the increasing solar hour angle at angles over 60°. That means that irradiance transitions with very high SS were not measured in the evenings. However, correlation between the SS and solar hour angle cannot be observed, which means that the SS does not depend on the time of the day. There were only negligible differences between the irradiance falls and rises.

The scatter plot between the duration and solar hour angle of all the irradiance transitions identified by all the three sensors is presented in Fig. 4.32. The duration had no correlation with the solar hour angle. There were only negligible differences between the scatter plots for the irradiance falls and rises.

The scatter plot between the apparent speed and the solar hour angle of all the identified shadow edges is presented in Fig. 4.33. The plots for the falls and rises were in broad terms

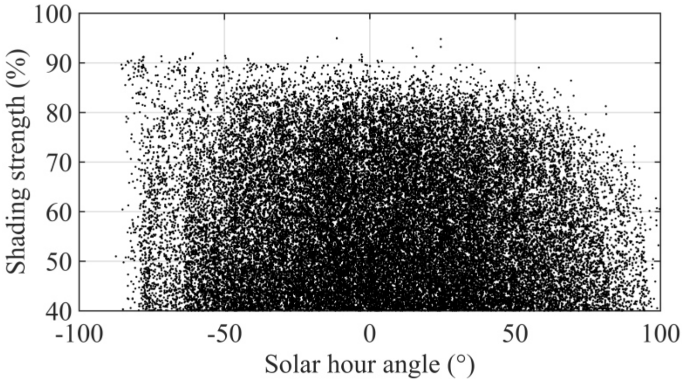

Figure 4.31. Scatter plot between the shading strength and solar hour angle of all the irradiance transitions identified by all the sensors of the used sensor triplet.

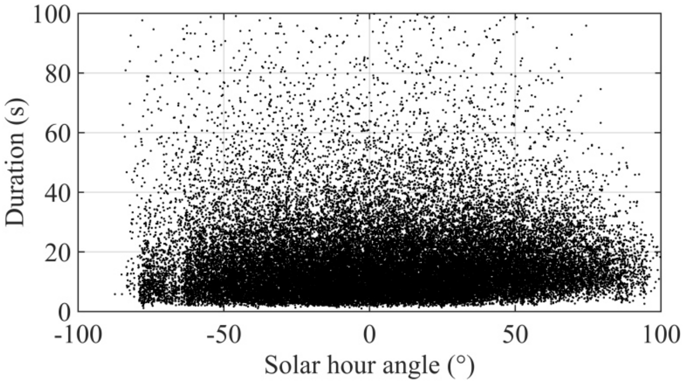

Figure 4.32. Scatter plot between the duration and solar hour angle of all the irradiance transitions identified by all the sensors of the used sensor triplet.

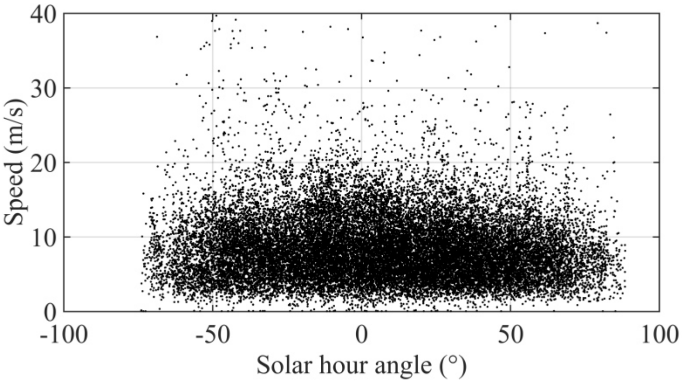

Figure 4.33. Scatter plot between the apparent speed and the solar hour angle of all the identified shadow edges.

similar. Correlation between the apparent speed and the solar hour angle cannot be observed, i.e., the apparent speed does not depend on the time of the day.

The scatter plot between the apparent direction of movement and solar hour angle of all the identified shadow edges is presented in Fig. 4.34. There were only negligible differences be-

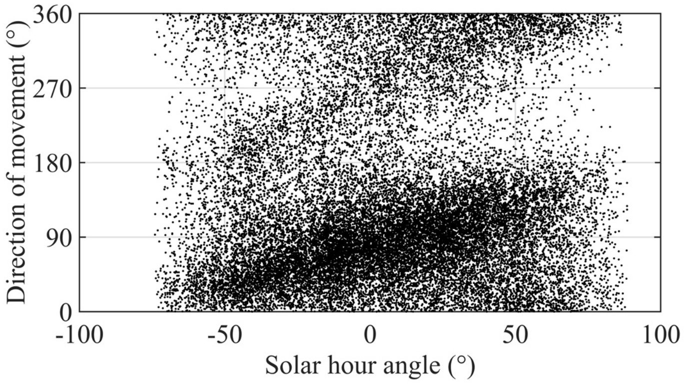

Figure 4.34. Scatter plot between the apparent direction of movement and the solar hour angle of all the identified shadow edges.

tween the plots for the irradiance falls and rises. No clear correlation between the apparent direction of movement and the solar hour angle of the shadow edges can be observed. However, there seems to be a weak tendency to have higher values for the apparent direction of movement with the increasing solar hour angle, i.e., before noon the directions are mostly towards north-east directions and in the afternoon more towards south-east directions.

The scatter plot between the SS and apparent direction of movement of all the shadow edges is presented in Fig. 4.35. The falls and rises provided almost identical scatter plots. The median and quantiles of the SS were almost constant showing that there were no correlation between the SS and apparent direction of movement of the shadow edges.

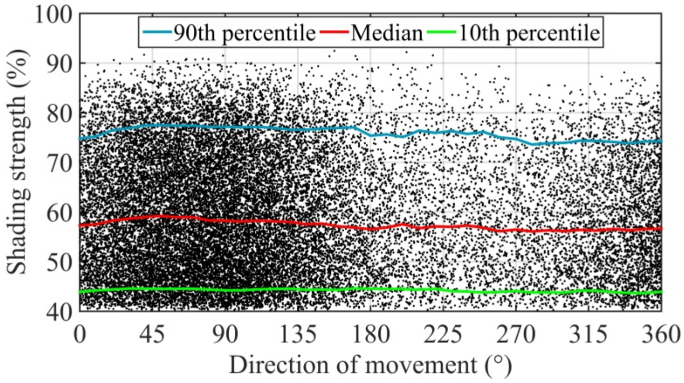

Figure 4.35. Scatter plot between the shading strength and the apparent direction of movement of all the identified shadow edges.

The scatter plot between the apparent speed and direction of movement of all the shadow edges is presented in Fig. 4.36. There were only negligible differences between the scatter plots of the irradiance falls and rises. The median and quantiles of the apparent speed were almost constant but achieved a bit higher values with directions of around 70° which were the most common directions of movement of the shadow edges. However, no considerable correlation between the apparent speed and direction of movement of the shadow edges can be observed.

Moreover, the apparent direction of movement of the shadow edges has no correlation with the duration of the irradiance transitions either.

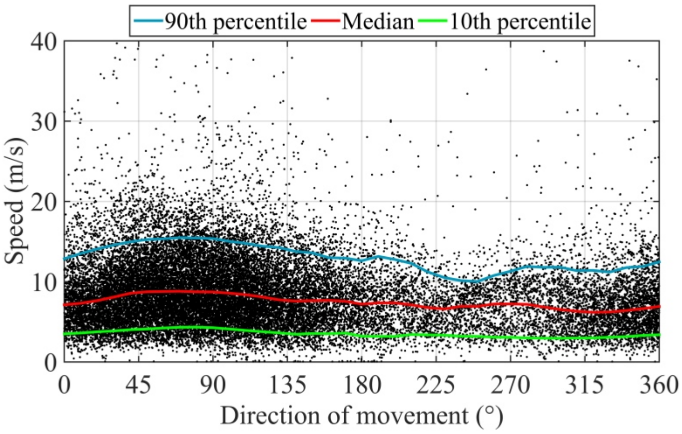

Figure 4.36. Scatter plot between the apparent speed and direction of movement of all the shadow edges.

The scatter plot between the SS and shadow length in the direction of movement of the shadows is presented in Fig. 4.37 (a). There was no clear dependence between these two char-

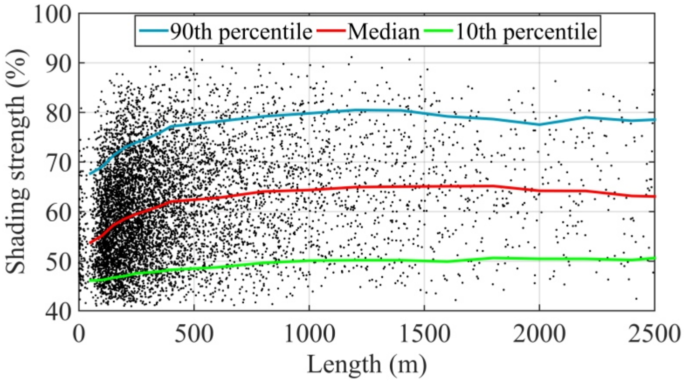

(a)

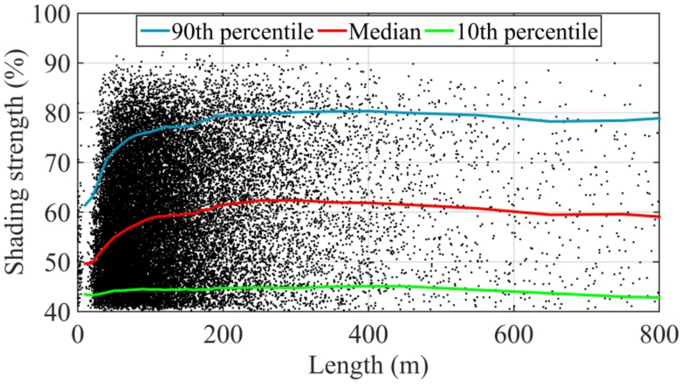

(b)

Figure 4.37. Scatter plots between the shading strength and the length of all the identified shadows in their direction of movement (a) and of all the identified shadow edges (b).

acteristics. The median and quantiles of the SS were constant, in practice, for shadows wider than 400 m or so. Their values decreased with the decreasing shadow length only at lengths below 400 m and very high values of SS did not appear with small lengths.

The scatter plot between the SS and length of all the irradiance transitions identified by all the three sensors is presented in Fig. 4.37 (b). The plots for the falls and rises were almost identical. The median and quantiles of the SS were constant for transitions wider than 100 m or so. However, their values decreased with the decreasing length at small lengths, similarly than was noticed for the shadow length in the direction of shadow movement. This indicates that the opacity of the cloud is independent on the length of the transition region, or vice versa, when the transition region is wide, but narrow irradiance transitions are more often caused by optically thin clouds.

No correlation was noticed between SS, duration, apparent speed and apparent direction of movement of shadow edges or between the corresponding characteristics of whole shadows either. The PCCs for all the combinations of the SS, duration, *b*, apparent speed and apparent direction of movement of the shadow edges are presented in Table 4.5. The PCCs were calculated from all the irradiance transitions detected by all the three sensors. As presented earlier, parameter *b* and the duration of irradiance transitions are closely related. Since the SS has no correlation with the duration of the irradiance transitions or with the apparent speed or direction of movement of the shadow edges, the exact value of the applied limit of minimum SS has no significant effect on the shapes of the distributions of these characteristics or of the length of the shadow edges.

Table 4.5. Pearson correlation coefficients for the shading strength, duration, *b* and apparent speed and direction of movement of the shadow edges.

Variables		PCC
SS	Duration	0.169
SS	*b*	−0.045
SS	Speed	−0.074
SS	Direction of movement	−0.052
Duration	*b*	0.806
Duration	Speed	−0.183
Duration	Direction of movement	0.070
b	Speed	−0.194
b	Direction of movement	0.086
Speed	Direction of movement	−0.145

The results of Table 4.5 mean that, by utilising Eq. (3.2), irradiance transitions can be defined using four variables: SS, parameter *b*, apparent speed and apparent direction of movement. The simulation approach for the modelling of the shading of PV arrays is illustrated in Section 5.3 and a parametrisation method of irradiance transitions in Section 5.4.

5 MODELLING OF THE OPERATION OF PV POWER GENERATORS

This chapter introduces the approach used to study the operation of PV generators. First, the used experimentally verified simulation model of PV modules is presented. After that, the studied PV arrays are presented and the shading of PV arrays is illustrated. In the last section of the chapter, a parametrisation method of irradiance transitions is presented. The parametrisation method has been presented and its applicability in PV system analysis has been demonstrated earlier in Lappalainen and Valkealahti (2016a). The applicability of the parametrisation method has been further contemplated relative to output power fluctuation and mismatch losses analyses in Lappalainen and Valkealahti (2017c and 2017b), respectively.

5.1 Simulation model for the PV modules

An experimentally verified MATLAB Simulink model of a PV module based on the model presented by Villalva et al. (2009) was employed in this study. The model is based on the widely used one-diode model of a PV cell that provides the relationship of Eq. (2.3) between the current and voltage of the PV cell. The simulation model for a PV module was obtained by scaling the parameter values used in the model of a PV cell by the number of PV cells in the PV module N_s. The thermal voltage of the PV module can be expressed as $U_T = N_s kT/q$. Bypass diodes of the PV module were modelled using Eq. (2.3) by assuming that the light-generated current I_{ph} is zero and the shunt resistance R_{sh} is infinite. The temperature of the bypass diodes was assumed to be constant and the same as the module temperature. The dark saturation current $I_{o,\,bypass}$, the series resistance $R_{s,\,bypass}$ and the ideality factor A_{bypass} of the bypass diodes were determined by means of curve fitting to a measured I–U curve of a Schottky diode.

The characteristics of the simulation model were fitted to the characteristics of the NAPS NP190GKg PV modules used in the TUT solar PV power station research plant. The NP190GKg module is composed of 54 series-connected polycrystalline silicon PV cells and three bypass diodes, each connected in anti-parallel with 18 cells. Its electrical characteristics given by the manufacturer in STC are presented in Table 5.1 and the parameter values of the simulation model for the PV modules and the bypass diodes in Table 5.2. The results of the simulations could slightly change if different PV modules were used as a reference. However, the basic behaviour would not change because the electrical characteristics of crystalline silicon PV modules do not differ substantially. The used simulation model is, naturally, a simplification of the reality containing simplifications and assumptions. However, it enables fast computation and is accurate enough for the analysis that is presented in this thesis. The experimental verification of the simulation model has been presented in Mäki et al. (2012).

Table 5.1. Electrical characteristics of the NAPS NP190GKg PV module for SC, OC and MPP in STC.

Parameter	Value
$I_{\mathrm{SC,\,STC}}$	8.02 A
$U_{\mathrm{OC,\,STC}}$	33.1 V
$P_{\mathrm{MPP,\,STC}}$	190 W
$I_{\mathrm{MPP,\,STC}}$	7.33 A
$U_{\mathrm{MPP,\,STC}}$	25.9 V

Table 5.2. Parameter values of the simulation model for the NAPS NP190GKg PV module and the bypass diodes.

Parameter	Value
A	1.30
R_{s}	0.329 Ω
R_{sh}	188 Ω
A_{bypass}	1.50
$R_{\mathrm{s,\,bypass}}$	0.02 Ω
$I_{\mathrm{o,\,bypass}}$	3.20 μA

5.2 PV arrays

The studied electrical PV array configurations were SP, TCT and MS. The electrical connections for the SP and TCT configurations, based on the central inverter topology, are presented in Fig. 2.15. The MS array configuration consists of individually controlled PV module strings and is based on the MS inverter topology presented in Fig. 2.14. These electrical array configurations were selected since SP and MS are commonly applied in PV installations, whereas TCT is frequently reported to improve PV array performance under PS compared to SP (Belhachat and Larbes, 2015; Gautam and Kaushika, 2002; Picault et al., 2010; Rakesh and Madhavaram, 2016; Villa et al., 2012; Wang and Hsu, 2011). The results obtained for the MS array configuration are applicable also for the string inverter topology (see Fig. 2.14) based PV plants where PV strings are controlled individually. Wiring losses and the effects of string diodes, possibly used in the SP configuration, were not taken into account in this study.

In the studied PV arrays, the series-connected PV modules were placed in straight strings of equal length to form a rectangle. The distance between the adjacent strings was 2.0 m, and there were no gaps between the series-connected modules. The PV modules were mounted at a tilt angle of 45° from the horizontal plane. The east-west orientation, i.e., an array orientation where the PV strings are placed from east to west, was used as a basic array orientation for the simulations. This basic orientation of the strings was denoted by angle 0° and the angle increased clockwise.

Various array layouts were studied, while the total number of PV modules stayed constant at 168. The longest string selected was 28 modules since it is near the string length in typical PV arrays that are feeding inverters in utility-scale PV power plants. The total number of modules was restricted by the need for reasonable computing time. Since PV arrays are the operational units of large PV power plants, the results achieved for these array sizes are largely valid for larger PV power plants as well. The nominal power of the studied arrays under STC was 31.92 kWp. The studied array layouts and their dimensions are presented in Table 5.3. The dimensions of the arrays were calculated using the dimensions of the NAPS NP190GKg PV modules (length: 1475 mm, width: 986 mm).

Table 5.3. Numbers of modules, the dimensions and the diagonals of the studied PV array layouts.

Number of modules (parallel × series)	Dimensions (m)	Diagonal (m)
6 × 28	14.2 × 41.3	43.7
8 × 21	19.6 × 31.0	36.6
12 × 14	30.4 × 20.7	36.7
14 × 12	35.8 × 17.7	39.9
21 × 8	54.6 × 11.8	55.9
28 × 6	73.5 × 8.9	74.1

The layouts with the longest strings, 6 × 28, 8 × 21 and 12 × 14, were used as basic layouts in the studies of the output power variation and mismatch losses of PV arrays. The layouts with shorter strings, 14 × 12, 21 × 8 and 28 × 6, were studied in Sections 6.3 and 7.3 where the effects of PV array layout and its geographic orientation on the output power variation and mismatch losses, respectively, were analysed in more detail.

5.3 Shading of a PV array

By utilising Eq. (3.2), irradiance transitions can be defined using four variables: SS, parameter *b* and apparent speed and direction of movement. As presented in Section 4.9, these characteristics have no correlation with each other. The duration of a transition was calculated by multiplying *b* by the experimentally obtained regression coefficient of 7.67, and parameter t_0 was then calculated from the duration. Almost 96% of the irradiance change of an irradiance transition defined by Eq. (3.2) happens during this time span. The average length of the identified irradiance transitions calculated from *b* and the apparent speed was 116 m and the duration of the identified irradiance transitions, that was calculated from the values of *b*, varied from 0.96 to 420 s.

For PV systems with physical and electrical array configurations having two orthogonal lines of symmetry, like the ones studied in this thesis, a shading situation caused by an overpassing irradiance fall is symmetrical to a situation that is caused by a similar overpassing irradiance rise. Thus, the absolute value of parameter *b* for the identified irradiance transitions was used in the simulations. The symmetry of the array configurations also reduces the amount of studied apparent movement directions of the shadow edges. When the configuration has two orthogonal lines of symmetry, the amount of apparent movement directions reduces to 90°. The symmetry of the studied array configurations further limits the amount of different array orientations to 180°.

The simulations were conducted using time steps of 0.1 s and the irradiance at the centre of each PV module with an accuracy of 0.1 W/m^2 was used as the irradiance of that module during a time step. A simulation period started when a shadow edge moved over the first module of the PV array and ended when the shadow edge had moved across the array, i.e., when all the modules of the array were again uniformly shaded. In order to simplify the computation, the PV array was chosen to be under the constant STC irradiance of 1000 W/m^2 before each irradiance fall. Moreover, the temperature of the PV modules was chosen as the constant STC temperature of 25 °C. During fast irradiance transitions, the changes of PV module temperatures are small having only a negligible effect on the operation of the modules. The duration of the simulation periods for the basic array layouts varied from 2.5 to 1038 s, depending on the characteristics of the shadow edge and the dimensions of the PV array. The average duration of the simulation periods (irradiance transitions) and the average rate of change of irradiance during the simulation periods are presented for different areas in Table 5.4.

Table 5.4. Average values for the duration and rate of change of irradiance for the irradiance transitions for different PV array areas. The rate of change of irradiance was calculated with respect to 1000 W/m^2.

Area	Duration (s)	Rate of change of irradiance (%/s)
Point	15.16	3.76
6 × 28 modules	21.46	2.66
8 × 21 modules	20.89	2.73
12 × 14 modules	20.94	2.72

The shading of a PV array is illustrated in Fig. 5.1, where the irradiance levels received by the modules of the 12 × 14 PV array during one time step are presented. The chosen time step is the midpoint of PS caused by the movement of a typical shadow edge over the PV array. The median values of the identified shadow edges, presented in Table 4.4, were used for the SS, *b* and apparent speed of the shadow edge and the apparent movement direction of the shadow edge was 45°, i.e., towards north-east. Four modules of the array are marked with letters from A to D in Fig. 5.1 (a) and the irradiance levels used for these modules, i.e., the irradiances at the centres of the modules, are shown in Fig. 5.1 (b) where the irradiance transition is presented.

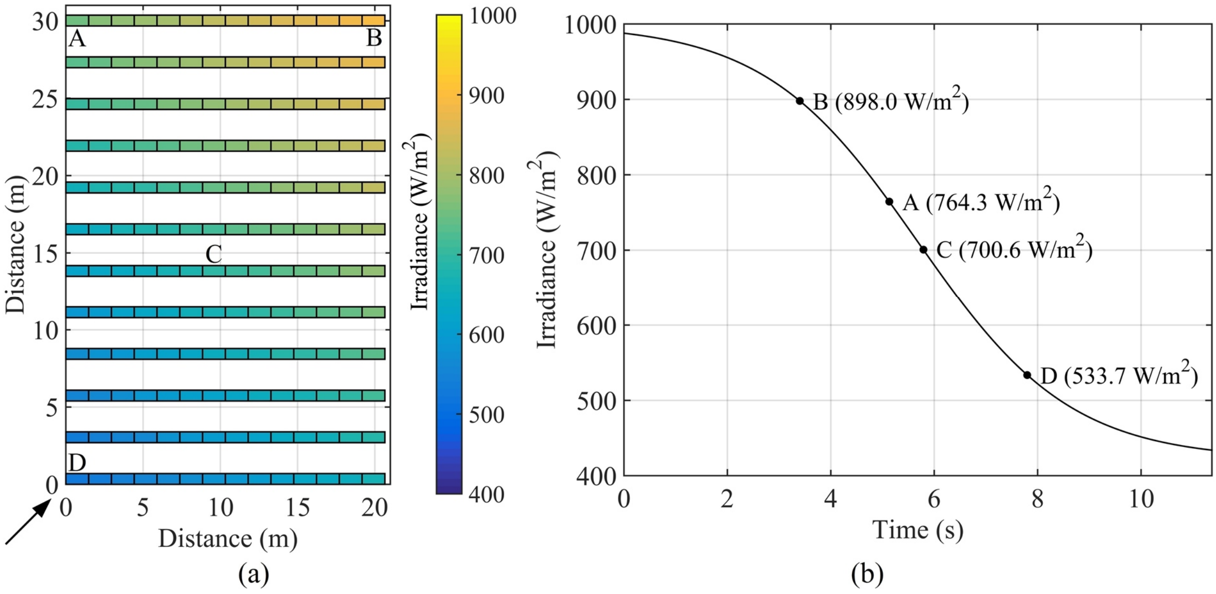

Figure 5.1. (a) Irradiance levels received by the modules of a 12 × 14 PV array at the midpoint of partial shading caused by the movement of a typical shadow edge over the array. The apparent movement direction of the shadow edge is denoted by an arrow on the bottom left corner. (b) Irradiance at a single point during the irradiance transition caused by the typical shadow edge.

As can be seen in Fig. 5.1 (a), irradiance differences between adjacent PV modules are small. The largest irradiance received by the modules is 898.0 W/m^2 (module B) and the smallest is 533.7 W/m^2 (module D). The irradiance difference between modules B and D during an irradiance transition is the largest when the midpoint of the transition is in the middle of the array. In Fig. 5.1, this very moment is presented. Thus, the irradiances received by the modules of the entire array are within 370 W/m^2 during a typical irradiance transition. Modules A and B are located in the opposite ends of a single string. Irradiance difference between these modules is only 133.7 W/m^2. The mean difference between the adjacent modules of this string is 10.3 W/m^2. It is obvious that this small irradiance differences within a PV string do not lead to large mismatch losses. The relative mismatch losses of this string are 1.9%. The relative mismatch losses of the array with the SP configuration during the time step presented in Fig. 5.1 and during the whole irradiance transition are 3.1% and 1.0%, respectively.

5.4 Parametrisation of irradiance transitions

Irradiance transitions can be parametrised by four variables: SS, *b*, apparent speed and apparent direction of movement. In the parametrisation process, the apparent direction of movement was divided into ten groups at regular intervals of 10°. The other variables were divided into groups by picking two values of a variable at a range of a certain margin from the end points of the cumulative distribution function (quantiles) and then dividing the space between the selected variable values to regular intervals. The margins and the numbers of groups used for the SS, *b* and apparent speed were chosen based on the error caused by the parametrisation with respect to the initial values.

The mean absolute errors of the initially obtained values with respect to the median values of the corresponding groups of the SS, *b* and apparent speed are presented in Tables 5.5–5.7, respectively, with different margins and numbers of groups. It seems that the error caused by the parametrisation decreases with the increasing number of the groups and that there is an optimal margin for each number of the groups which decreases with the increasing number of the groups. Errors for *b* and the apparent speed are higher than for the SS, because the shapes of their distributions are less flat (see Figs. 4.23 and 4.29). Therefore, their parameter value ranges were divided into more groups than that of the SS to achieve small enough errors close to the error of the used combination for the SS.

Based on the errors presented in Tables 5.5–5.7, the SS, *b* and apparent speed were divided into 5, 10 and 8 groups, respectively, and the median value of each group was used to represent that group. Thus, the total number of possible combinations of the variables was 4000, which is

Table 5.5. Mean absolute errors (%) of the initially obtained values of SS with respect to the median values of the corresponding groups with different margins and numbers of groups. The smallest error with each number of the groups is bolded and the error of the used combination is underlined.

		Margin (%)					
		1.5	2.0	2.5	3.0	3.5	4.0
Number of groups	5	3.92	3.89	3.87	3.86	**3.86**	3.86
	6	3.27	3.24	3.23	3.23	**3.23**	3.23
	7	2.82	2.80	2.79	**2.79**	2.79	2.80
	8	2.50	2.49	2.48	**2.47**	2.47	2.48
	9	2.22	2.21	**2.21**	2.21	2.22	2.23
	10	1.99	**1.98**	1.98	1.98	1.99	2.00

Table 5.6. Mean absolute errors (%) of the initially obtained values of *b* with respect to the median values of the corresponding groups with different margins and numbers of groups. The smallest error with each number of the groups is bolded and the error of the used combination is underlined.

		Margin (%)					
		1.5	2.0	2.5	3.0	3.5	4.0
Number of groups	5	21.70	21.54	21.29	21.11	21.03	21.01
	6	18.99	18.85	18.68	18.58	18.50	**18.48**
	7	16.94	16.88	16.74	16.69	16.67	**16.66**
	8	15.41	15.39	15.31	**15.29**	15.32	15.31
	9	14.11	14.14	**14.07**	14.09	14.13	14.20
	10	**13.07**	13.13	13.14	13.14	13.20	13.29

Table 5.7. Mean absolute errors (%) of the initially obtained values of apparent speed with respect to the median values of the corresponding groups with different margins and numbers of groups. The smallest error with each number of the groups is bolded and the error of the used combination is underlined.

		Margin (%)					
		1.5	2.0	2.5	3.0	3.5	4.0
Number of groups	5	13.31	13.22	13.15	**13.11**	13.11	13.12
	6	11.53	11.46	11.43	**11.40**	11.42	11.46
	7	10.26	10.22	**10.21**	10.21	10.24	10.30
	8	9.27	9.23	**9.21**	9.23	9.29	9.35
	9	8.42	**8.41**	8.43	8.48	8.53	8.62
	10	7.81	**7.80**	7.82	7.88	7.95	8.04

a feasible number of cases for simulating PV system operation compared to the initial number of the identified transitions of 27,210.

The used parameter values and the shares (weights) of the identified irradiance transitions falling into chosen groups of the variables are presented in Table 5.8. The identified irradiance transitions fell more evenly into the groups of the SS than of the other variables as could be expected based on the shapes of their distributions. The biggest differences between the shares of different groups exist in the case of *b*. This is expected since it has the most skew distribution.

The use of the parametrisation is computationally less demanding than the direct use of irradiance transitions or their curve fits and thus enables more demanding and complex simulations of the operation of PV systems. The parametrisation is particularly practical in studies with different PV array orientations since the turning of PV array with respect to the distribution of the apparent movement direction of shadow edges does not require further simulations, i.e., the results for all the array orientations can be achieved from the ones of one orientation by scaling them with the numbers of transitions in different variable groups.

Table 5.8. Parameter values used in the parametrisation and the shares of the identified irradiance transitions falling into the groups.

SS		*b*		Speed		Direction of movement	
Value (%)	Share (%)	Value (s)	Share (%)	Value (m/s)	Share (%)	Value (°)	Share (%)
45.59	28.4	0.61	24.9	3.51	17.4	0.00	4.2
53.78	22.0	1.09	19.2	5.45	17.6	10.00	9.0
61.87	18.9	1.53	15.0	7.19	17.5	20.00	9.6
69.66	16.3	1.97	11.5	8.92	16.1	30.00	10.2
78.45	14.4	2.42	8.6	10.64	11.2	40.00	10.8
		2.86	6.2	12.44	7.7	50.00	11.2
		3.31	3.9	14.15	5.2	60.00	12.3
		3.76	2.6	17.69	7.4	70.00	12.6
		4.22	1.9			80.00	13.3
		5.95	6.3			90.00	6.7

The applicability of the parametrisation method for researching the output power variation and mismatch losses of PV arrays was verified by comparing the results obtained by the direct use of the curve fits of Eq. (3.2) and the use of the parametrisation method. The comparison was done with all the identified irradiance transitions for the PV array layout with the longest PV module strings, i.e., the 6 × 28 modules array, which has the largest mismatch losses. The average duration of the simulation periods obtained by using the parametrisation method was about 19.6 s which is about 8.5% shorter than the one obtained by the direct use of the curve fits. The reason for this is that the parametrisation method restricts the duration of the longest simulation periods in which the value of *b* is larger or the value of speed is smaller than the values used in the parametrisation. The longest simulation period was 57.7 s when the parametrisation method was used while it was over 900 s when the curve fits were used directly. Consequently, also the amount of energy produced during all the identified irradiance transitions obtained by the use of the parametrisation method was lower than the one based on the direct use of the curve fits. The difference between the two methods was around 8% for all the electrical PV array configurations. The comparison of the average power of different electrical configurations during all the identified irradiance transitions between the two methods is presented in Table 5.9. The differences were very small.

The comparisons of the output power variation and mismatch losses obtained by the direct use of the curve fits and the use of the parametrisation method are presented in Tables 5.10 and 5.11, respectively. The largest differences between the two methods occurred during irradiance transitions with very small or large values of *b* or speed which were either smaller than the lowest or larger than the highest value used in the parametrisation method. Since the largest mismatch losses are caused by transitions with very small values of *b* and speed, the use of the

Table 5.9. Comparison of the average power of the 6 × 28 modules array during all the identified irradiance transitions between the direct use of curve fits and the use of the parametrisation method. The powers were calculated with respect to the nominal power of the array and the difference between the two methods with respect to the direct use of the curve fits.

Electrical configuration	Direct use of curve fits (%)	Parametrisation method (%)	Difference (%)
SP	67.26	67.51	0.37
TCT	67.35	67.56	0.32
MS	67.38	67.55	0.25

Table 5.10. Comparison of the power variations of the 6 × 28 PV array layout during all the identified irradiance transitions between the direct use of curve fits and the use of the parametrisation method. The rates of change in power were calculated with respect to the nominal power of the array and the difference between the two methods with respect to the direct use of the curve fits.

	Electrical configuration	Direct use of curve fits	Parametrisation method	Difference (%)
Average rate of change in power (%/s)	SP, TCT and MS	2.71	2.96	9.14
Average of the maximum instantaneous rates of change in power for all the irradiance transitions (%/s)	SP	11.63	11.33	2.63
	TCT	11.79	11.48	2.69
	MS	11.65	11.36	2.49

Table 5.11. Comparison of the relative mismatch losses of the 6 × 28 PV array layout during all the identified irradiance transitions between the direct use of curve fits and the use of the parametrisation method. The difference between the two methods was calculated with respect to the direct use of the curve fits.

Electrical configuration	Direct use of curve fits (%)	Parametrisation method (%)	Difference (%)
SP	4.04	3.56	11.73
TCT	3.92	3.49	10.82
MS	3.87	3.52	9.15

parametrisation method underestimate mismatch losses slightly. That can be seen from Table 5.11, where the relative mismatch losses obtained using the curve fits directly are of the order of 10% larger than those obtained using the parametrisation method. The difference in the average rate of change in power during all the identified irradiance transitions between the two methods was around 9%. However, the differences in the averages of the maximum instantaneous rates of change in power for all the irradiance transitions were reasonably small. Moreover, the differences between different array shapes and electrical configurations were largely in line with the results achieved by the direct use of the curve fits. In conclusion, the parametrisation process provides a good overall average description of power transitions and mismatch losses caused by cloud shadings and is accurate enough for the analysis that is presented in this thesis.

Naturally, the error caused by the parametrisation can be reduced by increasing the number of the variable groups. However, that makes the use of the parametrisation method computationally more demanding and thus reduces the usability of the method. The method can be quite easily applied to different weather conditions by adjusting the numbers and representative values of the variable groups to local weather conditions. Thus, the use of the parametrisation method is not regionally bounded which increases the applicability of the method.

6 OUTPUT POWER VARIATION CAUSED BY MOVING CLOUDS

This chapter presents and discusses the results of the study of the output power variation of PV generators caused by moving clouds. The effects of irradiance transition characteristics, SS, sharpness, apparent speed and apparent direction of movement, on the output power variation were studied and the results of this study are presented in Section 6.1. The output power variation was also studied during all of the 27,210 identified irradiance transitions by directly using the curve fits of Eq. (3.2). These results are presented in Section 6.2. Further, the effects of PV array layout and its geographic orientation on the output power variation were studied by using the parametrisation method of irradiance transitions presented in Section 5.4. The results of these analyses are presented in Section 6.3. Most of the results presented in this chapter have been presented earlier in Lappalainen and Valkealahti (2016d and 2017c). Output power variation of a PV array was studied by analysing the rate of change in the power of the array which was calculated with respect to the nominal power of the array.

An example of the irradiance and output power fluctuations and the mismatch losses during PS caused by the movement of a cloud shadow edge over a PV array is presented in Fig. 6.1. The SS of the shadow edge was 85%, *b* 0.97 s, apparent speed 4.4 m/s and the apparent direction of movement 10° from the direction parallel to the PV strings of the array. As can be seen in the figure, the PV output power decreases clearly steeper than the irradiance does. The difference between the irradiance and output power fluctuations resulted mostly from the mismatch losses, as demonstrated by the combined curve of the mismatch losses and output power.

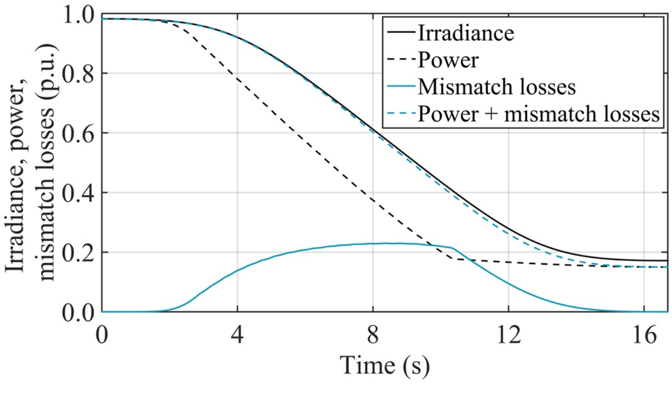

Figure 6.1. Average irradiance, output power and mismatch losses for the 6 × 28 PV array layout with the SP configuration during partial shading caused by the movement of a shadow edge over the array. Irradiance is with respect to 1000 W/m^2 and power and mismatch losses to the nominal power of the array.

The combined power curve is only slightly below the irradiance curve. The remaining small difference is caused by the fact that the relative power of a uniformly shaded PV module is lower than the relative irradiance falling on the module when that irradiance is lower than the STC irradiance. This basic behaviour of silicon PV cells is presented in Fig. 2.6. In view of the simplifications of the used simulation model, the behaviour of the maximum power of a uniformly shaded PV array is identical to that in Fig. 2.6. Hence, as can be seen in Fig. 6.1, at the beginning of the transition, the relative power is at the same level with the relative irradiance, but at the end of the irradiance transition, when all the modules are uniformly shaded, the relative power of the array is lower than the relative irradiance. Thus, the relative change of power is larger than the one for irradiance, i.e., the average rate of change of power during irradiance transitions is larger than the average rate of change of irradiance.

The average rate of change in power is the same for all the electrical PV array configurations since the PV array is under constant irradiance before and after each irradiance fall, i.e., there is no difference in the power between the configurations in the beginning or end of simulation periods. Similarly, there are no differences between the instantaneous rates of change in the power of the studied electrical array configurations when a shadow edge moves parallel to the PV strings since in that case every configuration behaves like a single PV string. Differences in the instantaneous rates of change of power between the electrical configurations, existing with other movement directions of shadow edges, are caused by mismatch losses.

6.1 Effects of irradiance transition characteristics on output power variation

The effects of the SS, sharpness (parameter *b*), apparent speed and apparent direction of movement of irradiance transitions on the output power variation of 6 × 28, 8 × 21 and 12 × 14 PV arrays were studied by changing the value of the studied variable while keeping the values of the other variables fixed. The applied variable value ranges were based on the experimentally obtained values (Chapter 4). The median values of the identified shadow edges presented in Table 4.4 were applied as the fixed values of the SS, *b* and apparent speed in the simulations. By using these values, the typical duration and length of irradiance transitions were 11.4 s and 89.4 m, respectively, and the duration of a corresponding simulation period varied between 12.5 and 20.8 s depending on the dimensions of the array (Table 5.3) and the apparent movement direction of the shadow edge. The duration of the simulation periods varied from 1.9 to 199 s while changing the values of parameter *b* and apparent speed over their ranges.

The average rate of change in power for all the studied PV generators during a typical irradiance transition is presented as a function of the apparent direction of movement of the shadow edge in Fig. 6.2. Angle 0° denotes perpendicular and 90° parallel movement with respect to the PV strings. The average rate of change in power is dependent on the length of the simulation period. Because the diameter of the PV array varies with direction, i.e., the array layout is not circular, the time it takes for a shadow edge to move over the PV generator depends on the apparent direction of movement of the shadow edge. Thus, the average rate of change in power is the largest when the diameter of the array is the smallest and, correspondingly, the smallest when the diameter is the largest. However, as can be seen in Fig. 6.2, the effect of the apparent direction of movement of the shadow edge on the average rate of change in PV output power is quite small. For that reason, the results of the effects of SS, *b* and apparent speed are presented only for perpendicular shadow edge movement.

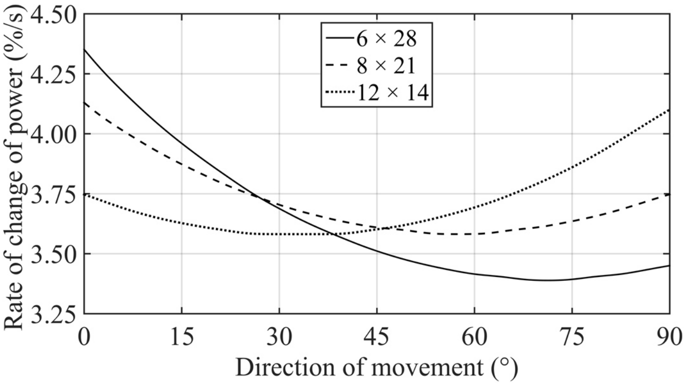

Figure 6.2. Average rate of change in the power of three PV array layouts during partial shading caused by the movement of a typical shadow edge over the PV array as a function of the apparent direction of movement of the shadow edge.

The average rate of change in power for all the studied PV generators during a typical irradiance transition is presented as a function of the SS in Fig. 6.3 for perpendicular shadow edge movement. In line with the behaviour of maximum power as a function of irradiance in Fig. 2.6, the average rates of change in power increased almost linearly with the increasing SS.

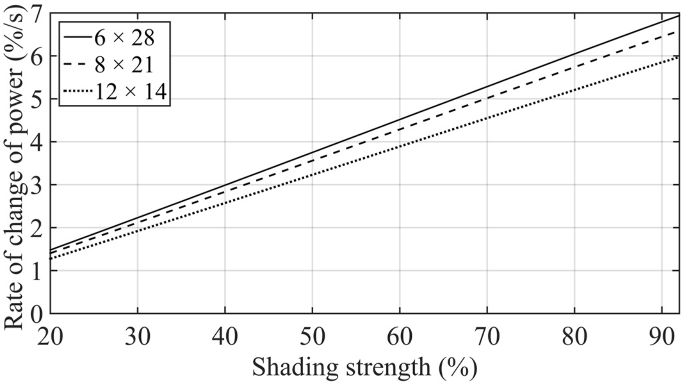

Figure 6.3. Average rate of change in the power of three PV array layouts as a function of the shading strength during partial shading caused by the movement of a typical shadow edge over the PV array perpendicular to the strings.

The average rate of change in power for all the studied PV generators during a typical irradiance transition is presented as a function of parameter *b* in Fig. 6.4 for perpendicular shadow edge movement. The rates of change of power decreased with increasing *b* which is understandable because the higher is *b*, the gentler is the irradiance transition, i.e., the lower is the rate of change of irradiance. The average rates of change of power were remarkable large with small values of *b*.

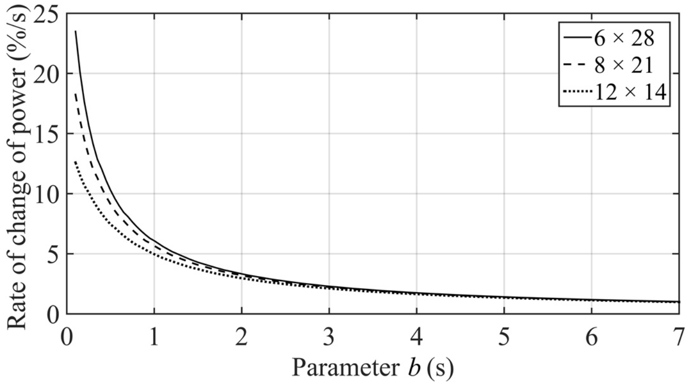

Figure 6.4. Average rate of change in the power of three PV array layouts as a function of parameter *b* during partial shading caused by the movement of a typical shadow edge over the PV array perpendicular to the strings.

The average rate of change in power for all the studied PV generators during a typical irradiance transition is presented as a function of the apparent speed of the shadow edge in Fig. 6.5 for perpendicular shadow edge movement. The average rates of change increased with the increasing speed levelling off at high speeds.

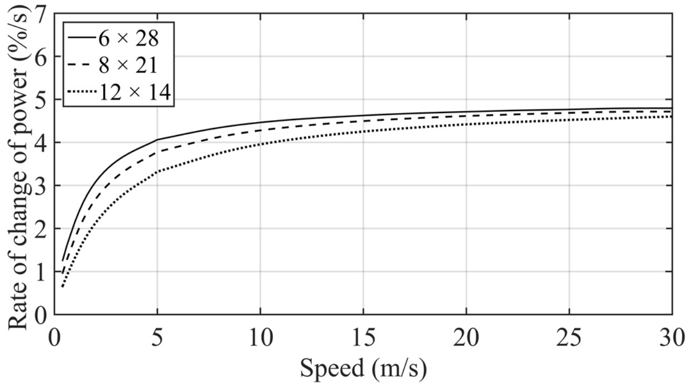

Figure 6.5. Average rate of change in the power of three PV array layouts as a function of the apparent speed during partial shading caused by the movement of a typical shadow edge over the PV array perpendicular to the strings.

The average rate of change in power in Figs. 6.3–6.5 is the highest for the 6 × 28 PV array layout since it has the smallest dimension for perpendicular shadow edge movement. However, the differences between the array layouts were mostly small and the biggest differences existed with very small values of *b*.

6.2 Output power variation during identified irradiance transitions

The output power variation of 6 × 28, 8 × 21 and 12 × 14 PV arrays with the SP, TCT and MS electrical configurations and the typical east-west orientation was studied by analysing the rate of change in power during all the identified irradiance transitions. The study was conducted by directly using the curve fits of Eq. (3.2). The average rate of change in power during all the identified irradiance transitions, the maximum average rate of change in power during a single irradiance transition and the average of the maximum instantaneous rates of change in power for all the identified irradiance transitions are presented for all the studied PV arrays in Table 6.1. The average rate of change of power for all the studied PV arrays during the transitions was between 2.7 and 2.8 %/s. The average rates of change in power were somewhat larger than the corresponding average rates of change in irradiance (Table 5.4) as rationalised earlier. The average rate of change in power was the smallest for the 6 × 28 modules array, which had the longest diagonal, but the differences were marginal.

Table 6.1. Power variation of the studied PV arrays during all the identified irradiance transitions with respect to the nominal power of the array.

Electrical configuration	Layout	Average rate of change in power (%/s)	Maximum average rate of change in power during an irradiance transition (%/s)	Average of the maximum instantaneous rates of change in power for all the irradiance transitions (%/s)
SP	6 × 28	2.71	24.6	11.6
SP	8 × 21	2.79	23.2	11.8
SP	12 × 14	2.78	26.5	11.2
TCT	6 × 28	2.71	24.6	11.8
TCT	8 × 21	2.79	23.2	12.0
TCT	12 × 14	2.78	26.5	11.5
MS	6 × 28	2.71	24.6	11.7
MS	8 × 21	2.79	23.2	11.8
MS	12 × 14	2.78	26.5	11.3

The largest observed instantaneous rate of change in power (during one time step of 0.1 s) was around 75 %/s. That large variation in PV output power caused by moving clouds has not been presented earlier. However, the use of the mathematical model of Eq. (3.2) smoothed the irradiance transitions and reduced the largest instantaneous rates of change of irradiance compared to actual irradiance transitions. Thus, even larger instantaneous rates of change can be expected to occur in the MPP power of real PV systems.

Only some negligible differences existed in the maximum instantaneous rates of change for different electrical configurations. The reason for the small differences between the electrical PV array configurations is that shadows of moving clouds produce gentle irradiance transitions causing typically only minor irradiance differences between adjacent PV modules. However, shadows caused by nearby objects, which are typically much sharper than cloud shadows, may bring about certain differences between the electrical PV array configurations. Thus, it must be emphasised that, in this thesis, only shadings due to moving clouds have been studied, and thus the results of this chapter concern power variation during irradiance transitions caused specifically by moving clouds. These results mean that in locations where shadows of nearby objects do not exist, the electrical configurations of PV arrays will have only minor effects on the power variation of the system. Thus, from an output power variation point of view, one can just use the simplest configuration. This finding is valid also for large utility-scale PV power plants with multiple PV arrays since these arrays are their operational units. Because of the insignificant differences in the power variation of different electrical array configurations, only the SP configuration is considered in the rest of this chapter.

The relative cumulative frequency of the rate of change in the power of the three different array layouts of the SP configuration during all the identified irradiance transitions is presented in Fig. 6.6. The differences between different array layouts were very small, but yet bigger than the negligible differences between the electrical SP, TCT and MS configurations with the same array layout. As can be seen in Fig. 6.6, the rate of change in the power was most of the time low while large variations also seldom took place. 50% of the time the rate of change in the power was over 1.2 %/s, and 10% of the time it was over 7.1 %/s. However, a typical 10 %/min requirement of grid operators for PV power ramp rate limit was exceeded by the studied PV arrays most of the time during the studied irradiance transitions. This aspect indicates clearly that PV power variation caused by cloud shadows can be a clear problem for power systems.

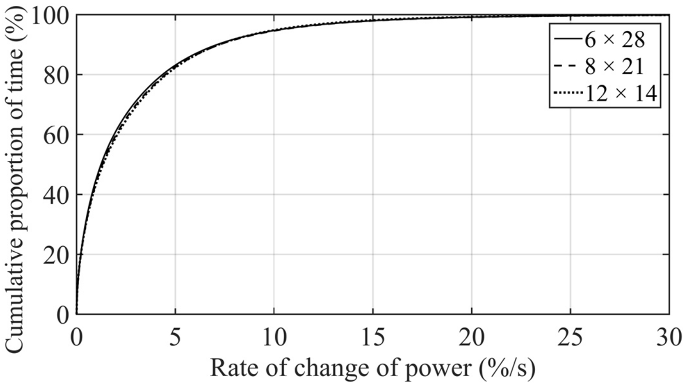

Figure 6.6. Relative cumulative frequency of the rate of change in the power of three PV array layouts of the SP configuration during all the identified irradiance transitions.

6.3 Effects of the PV array layout and orientation on output power variation

The effects of PV array layout and its geographic orientation on PV output power variation were studied by using the parametrisation method of irradiance transitions. The average rate of change in power for six different PV array layouts with the SP electrical configuration during all the identified irradiance transitions is presented as a function of the array orientation in Fig. 6.7. The average rate of change in power was the highest for the 8 × 21 and 12 × 14 modules layouts which were closest to the shape of a square (see Table 5.3). The lowest rate of change in power was for the 28 × 6 modules array, which was the most elongated array with the shortest strings of PV modules.

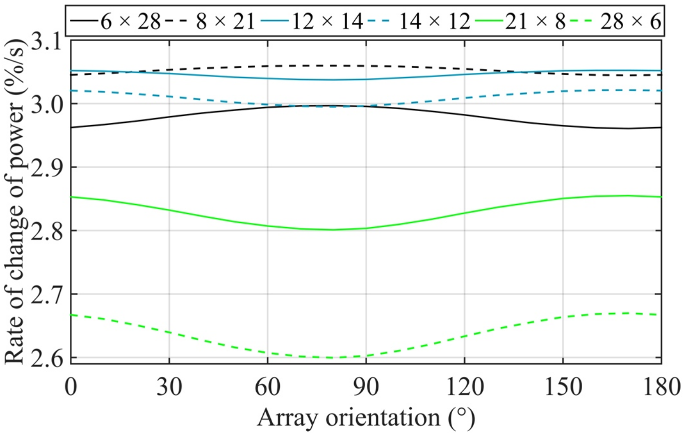

Figure 6.7. Average rate of change in the power of six PV array layouts of the SP configuration as a function of the array orientation during all the identified irradiance transitions. Angle 0° denotes the basic east-west orientation of the PV strings and the angle increases clockwise.

The orientation of the PV arrays with respect to the dominant direction of movement of the shadow edges had quite a small effect on power variation (compare Figs. 6.7 and 4.25). The reason is that the average length of the shadow edges was over 140 m, i.e., much longer than the dimensions of the studied PV arrays, and thus, the effects of irradiance variation on power production are smoothed. This aspect is also seen in Fig. 6.7 on a smaller scale. When the shadow edges move dominantly along the shorter dimension of a PV array, the output power varies slightly more than when they move dominantly along the longer dimension of the array. The effect of array orientation is the stronger the more elongated is the array shape. The smoothing of the power fluctuations increases with the increasing diagonal length of a PV array. This aspect is further in line with the results that the power of the 28 × 6 PV array layout varied clearly less than the others since it had the longest diagonal (see Table 5.3). These findings of the effect of array orientation have practical importance in the design of PV installations in locations where shadow edges have a clearly dominant apparent direction of movement.

In order to further demonstrate the smoothing of power fluctuations with increasing PV array dimensions, the average rate of change in power is presented as a function of the length of the diagonal of the array in Fig. 6.8 for the east-west oriented SP configuration. The average rate of change in the power decreased almost linearly with the increasing diagonal length. The curve fit of Fig. 6.8 gets a value of 3.40 %/s at the diagonal length of one module (1.77 m). That value is smaller than the average rate of change of irradiance at a single point (Table 5.4), indicating that the average rate of change in power is not truly subject to linear but instead more like exponential decay on a larger scale of diagonal.

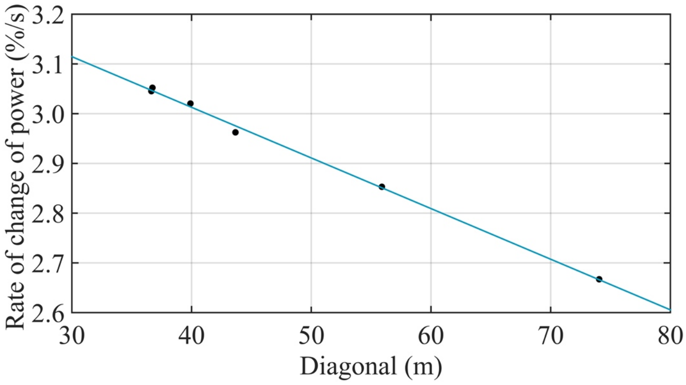

Figure 6.8. Average rate of change in the power of the east-west oriented SP configuration as a function of the length of the diagonal of the PV array and a linear fit to the results.

In large PV power plants, the size of the PV arrays is determined by the size of the used inverters. Thus, the decay of the average rate of change in power presented in Fig. 6.8 is not directly applicable to PV plants with multiple arrays. However, the average rate of change in the power of a large PV power plant decreases with an increasing number of PV arrays since the power fluctuations of the arrays do not happen simultaneously, thus reducing the total output power variation of the plant.

7 MISMATCH LOSSES CAUSED BY MOVING CLOUDS

In this chapter, the results regarding the mismatch losses of PV generators caused by moving clouds are presented and discussed. The results of the study of the effects of irradiance transition characteristics, SS, sharpness, apparent speed and apparent direction of movement, on the mismatch losses are presented in Section 7.1. The mismatch losses were also studied during all the identified irradiance transitions by directly using the curve fits of Eq. (3.2). These results are presented in Section 7.2. The effects of PV array layout and its geographic orientation on the mismatch losses were studied by using the parametrisation method of irradiance transitions and the results are presented in Section 7.3. Further, the overall effect of the mismatch losses caused by moving clouds on the energy production of PV plants was studied and the results of this study are presented in Section 7.4. Most of the results presented in this chapter have been presented earlier in Lappalainen and Valkealahti (2017a, 2017b and 2017d).

The mismatch losses of a PV array were calculated as the difference between the sum of the global MPP powers of the PV modules of the array, as if they were operating separately, and the global MPP power of the array. Relative mismatch losses were calculated with respect to the sum of the global MPP powers of the PV modules.

When a linear shadow edge moves perpendicular to the strings of a PV array, each string of the array is under uniform irradiance conditions. Thus, no mismatch losses occur in the MS configuration, where the strings are operated individually, and the mismatch losses of the SP and TCT configurations are equal and negligible. The relative mismatch losses of the SP and TCT configurations are presented as a function of PV string length during PS caused by the movement of a typical shadow edge (median values of Table 4.4) over the PV array perpendicular to the strings in Fig. 7.1. The total number of PV modules stayed constant at 168, while different string lengths were studied. In this way, all the array layouts of Table 5.3 were studied. The relative mismatch losses decreased with the increasing string length. This is plausible since all the mismatch losses resulted from mismatch between the PV strings, and the number of the strings, as well as the irradiance differences between the strings, increased while their length decreased.

When a linear shadow edge moves parallel to the strings of a PV array, every string of the array is under identical irradiance conditions with each other. Thus, each array configuration behaves like a single series connected PV string and the mismatch losses of all the configurations are equal. When the apparent shadow edge movement direction is 45°, most of the mis-

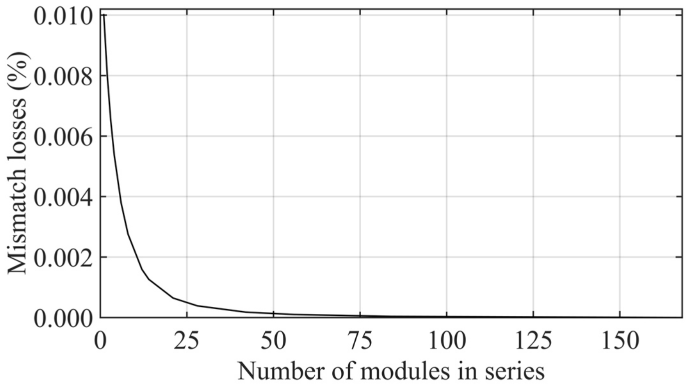

Figure 7.1. Relative mismatch losses of the SP and TCT configurations as a function of the PV array string length during partial shading caused by the movement of a typical shadow edge over the PV array perpendicular to the strings. The total number of PV modules in the array is constant 168.

match losses in the SP and TCT configurations result from the irradiance differences within the series connections. The relative mismatch losses of the SP, TCT and MS configurations are presented as a function of the string length during PS caused by the movement of a typical shadow edge, with apparent movement direction of 45° and 90°, over the PV array in Fig. 7.2. In these cases, the mismatch losses increased with the increasing string length since the irradiance differences within the series connections increased with the increasing string length. In the case of 45° apparent shadow edge movement direction, the differences between the electrical PV array configurations were minimal. The mismatch losses for the perpendicular apparent shadow edge movement in Fig. 7.1 are more than two orders of magnitude smaller than for the other two directions of movement in Fig. 7.2. The basic behaviour of the mismatch losses caused by shadow edges with these three apparent movement directions is illustrated in more detail in Lappalainen et al. (2013a and 2013b).

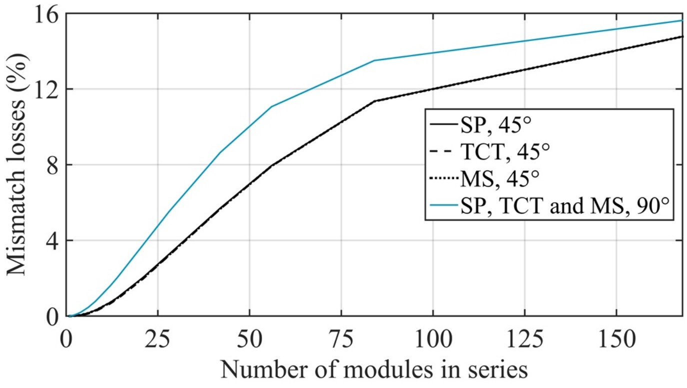

Figure 7.2. Relative mismatch losses of the SP, TCT and MS configurations as a function of the PV array string length during partial shading caused by the movement of a typical shadow edge, with apparent movement direction of 45° and 90°, over the PV array. Angle 90° denotes parallel movement with respect to the PV strings. The total number of PV modules in the array is constant 168.

7.1 Effects of irradiance transition characteristics on mismatch losses

The effects of the SS, sharpness (parameter *b*), apparent speed and apparent direction of movement of irradiance transitions on the mismatch losses of PV generators caused by moving clouds were studied by a similar approach than was used in the case of the output power variation in Section 6.1. The effect of each variable was studied by changing the value of the variable while keeping the values of the other variables fixed. The applied variable value ranges were based on the experimentally obtained values (Chapter 4). The median values of the identified shadow edges presented in Table 4.4 were applied as the fixed values of the SS, *b* and apparent speed in the simulations. The effects of the SS, *b* and apparent speed were studied with three apparent movement directions of shadow edges. The studied PV array layouts were 6 × 28, 8 × 21 and 12 × 14.

The relative mismatch losses of all the studied PV generators during a typical irradiance transition are presented as a function of the apparent direction of movement of the shadow edge in Fig. 7.3. The relative mismatch losses increased with the increasing angle between the apparent direction of movement of the shadow edge and the direction perpendicular to the PV strings from almost zero to about 5.5% for the longest PV module strings. This is plausible since all the PV modules in each string are under the same irradiance when the shadow edge moves perpendicular to the strings and irradiance differences within the strings increase with the increasing angle. There were only minor differences between the studied electrical PV array configurations, which means that the mismatch losses are almost independent of the electrical PV array configuration during irradiance transitions caused by moving clouds. The differences between the electrical configurations were the biggest at angles around 45°. Furthermore, it is notable that the relative mismatch losses increased considerably with the increasing

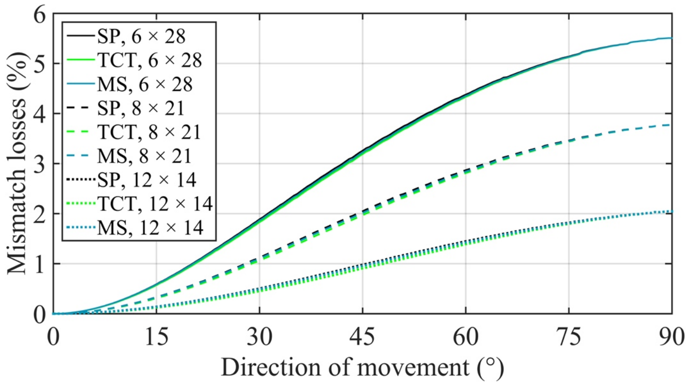

Figure 7.3. Relative mismatch losses of the SP, TCT and MS configurations during partial shading caused by the movement of a typical shadow edge over the PV array as a function of the apparent direction of movement of the shadow edge. Angle 0° denotes perpendicular and 90° parallel movement with respect to the PV strings.

length of the strings being almost three times larger for the PV arrays having strings of 28 PV modules than for the arrays having strings of 14 modules. The reason for this is that irradiance differences between the modules of a string increases with the increasing physical string length.

The relative mismatch losses of all the studied PV generators during a typical irradiance transition are presented as a function of the SS in Fig. 7.4 for apparent directions of movement of 0°, 45° and 90°. The relative mismatch losses increased with the increasing SS and with the

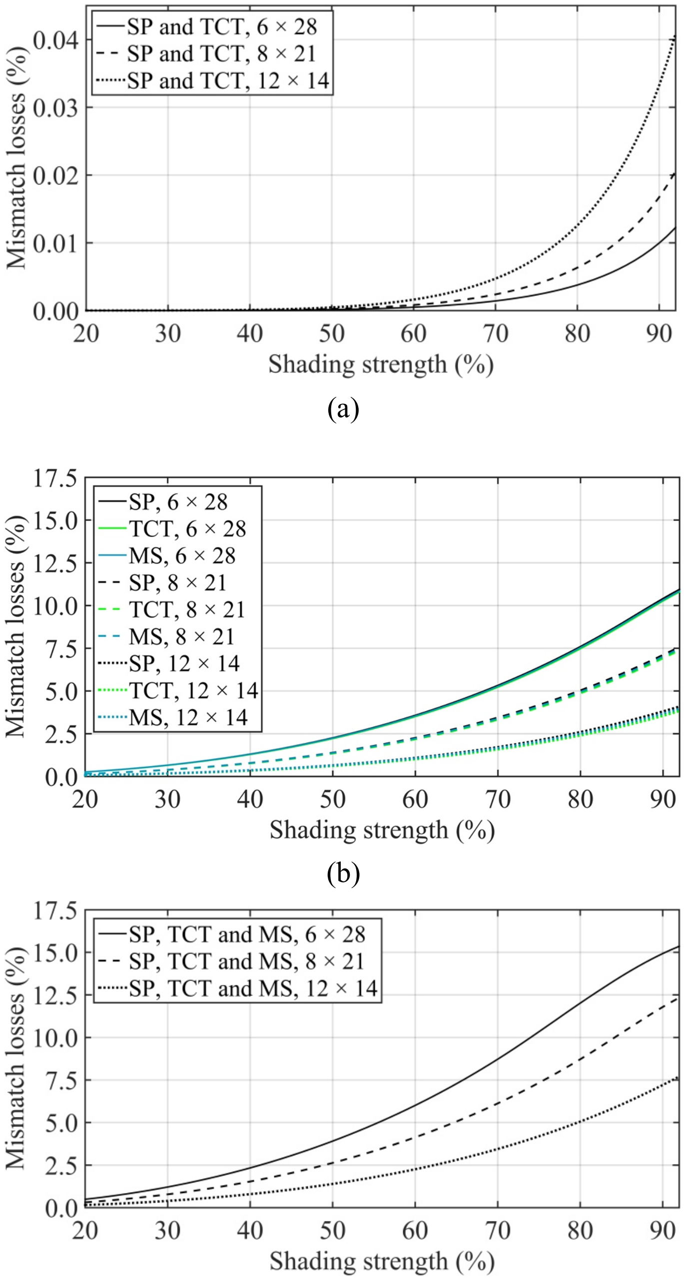

(a)

(b)

(c)

Figure 7.4. Relative mismatch losses of the SP, TCT and MS configurations as a function of the shading strength during partial shading caused by the movement of a typical shadow edge, with apparent movement directions of 0° (a), 45° (b) and 90° (c), over the PV array.

increasing angle between the apparent direction of movement and the direction perpendicular to the PV strings. The relative mismatch losses increased also with the increasing length of the strings, except in the case of perpendicular shadow edge movement (Fig. 7.4 (a)). When a shadow edge moves perpendicular to the strings, each string is under uniform irradiance conditions and the relative mismatch losses increase with the increasing number of the strings. As presented earlier, the mismatch losses of SP, TCT and MS configurations are identical in the case of parallel shadow edge movement. With the other directions, the differences between the electrical configurations were minimal. Note that the mismatch losses were more than two orders of magnitude smaller for the perpendicular direction of movement than for the other two directions.

The relative mismatch losses of all the studied PV generators during a typical irradiance transition are presented as a function of parameter *b* in Fig. 7.5 for apparent directions of movement of 0°, 45° and 90°. The mismatch losses decreased with increasing *b* which is understandable because the higher is *b*, the gentler is the irradiance transition, i.e., the smaller are the irradiance differences between adjacent PV modules. Again, the relative mismatch losses increased with the increasing angle between the apparent direction of movement and the direction perpendicular to the strings and, in the case of Figs. 7.5 (b) and (c), with the increasing length of the strings. In practice, there were no differences between the electrical PV array configurations at values of *b* higher than 1 s. However, some differences between the electrical configurations existed at small values of *b*. A fold can be seen in the relative mismatch losses of the MS configuration at small values of *b* in Fig. 7.5 (b) (apparent direction of movement of 45°). This is in accord with the results of Lappalainen et al. (2013a and 2013b) that the relative mismatch losses of the MS configuration turn down as the length of the PV strings increase with respect to the length of the irradiance transition in the case of diagonal shadow edge movement across the PV array.

The relative mismatch losses of all the studied PV generators during a typical irradiance transition are presented as a function of the apparent speed of the shadow edge in Fig. 7.6 for apparent directions of movement of 0°, 45° and 90°. Since the length of an irradiance transition is calculated as the product of the duration and apparent speed of the transition, both the apparent speed and parameter *b* have an effect on the length of the transition. Thus, the behaviour of the mismatch losses as a function of the apparent speed is qualitatively similar than as a function of *b* (Fig. 7.5) and the same phenomena can be observed by studying the mismatch losses as functions of these variables. The relative mismatch losses decreased with the increasing speed and, again, increased with the increasing angle between the apparent direction of movement and the direction perpendicular to the strings and, in the case of the apparent directions of movement of 45° and 90°, with the increasing length of the strings. In practice, there were no differences between the electrical PV array configurations except at slow apparent speeds.

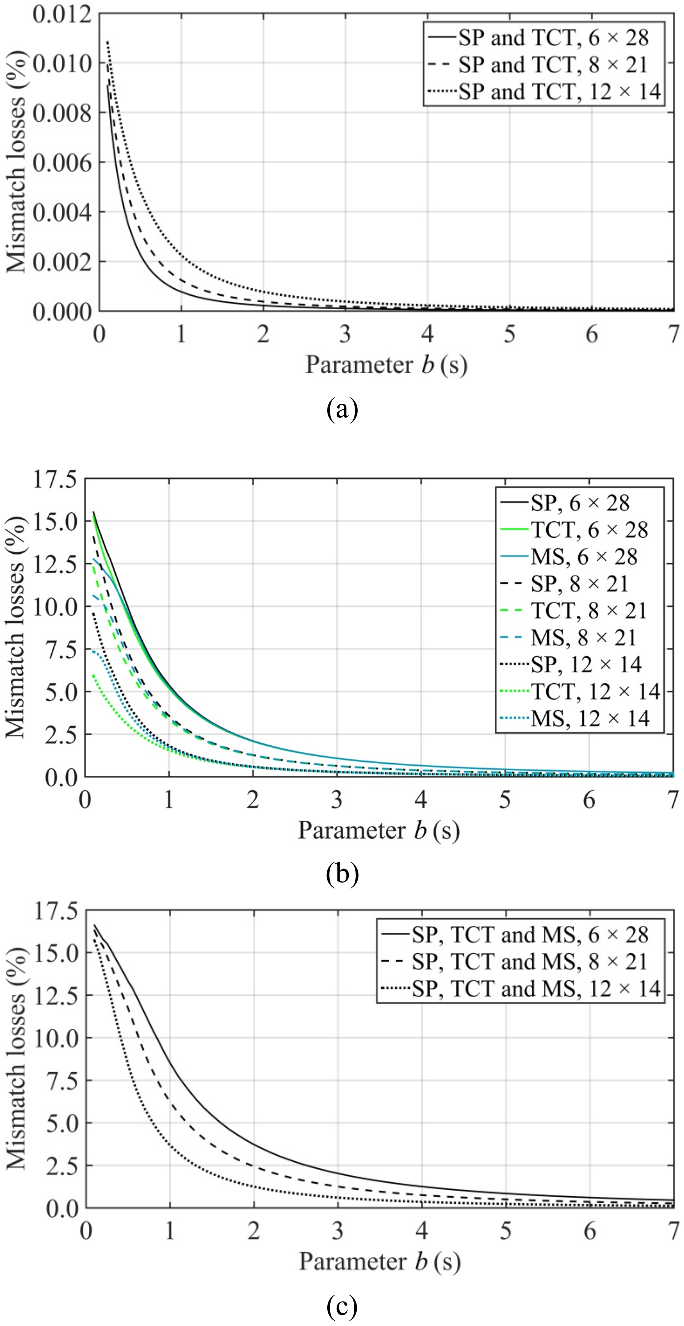

Figure 7.5. Relative mismatch losses of the SP, TCT and MS configurations as a function of parameter *b* during partial shading caused by the movement of a typical shadow edge, with apparent movement directions of 0° (a), 45° (b) and 90° (c), over the PV array.

Only minor differences in the mismatch losses were observed between the studied electrical PV array configurations. The reason for this is that the length of a typical irradiance transition region is much longer than the diameters of the PV arrays, i.e., there are typically only small irradiance differences between the interconnected PV modules. Only the steepest and fastest shadow edges bring about some differences on the operation of different PV array configura-

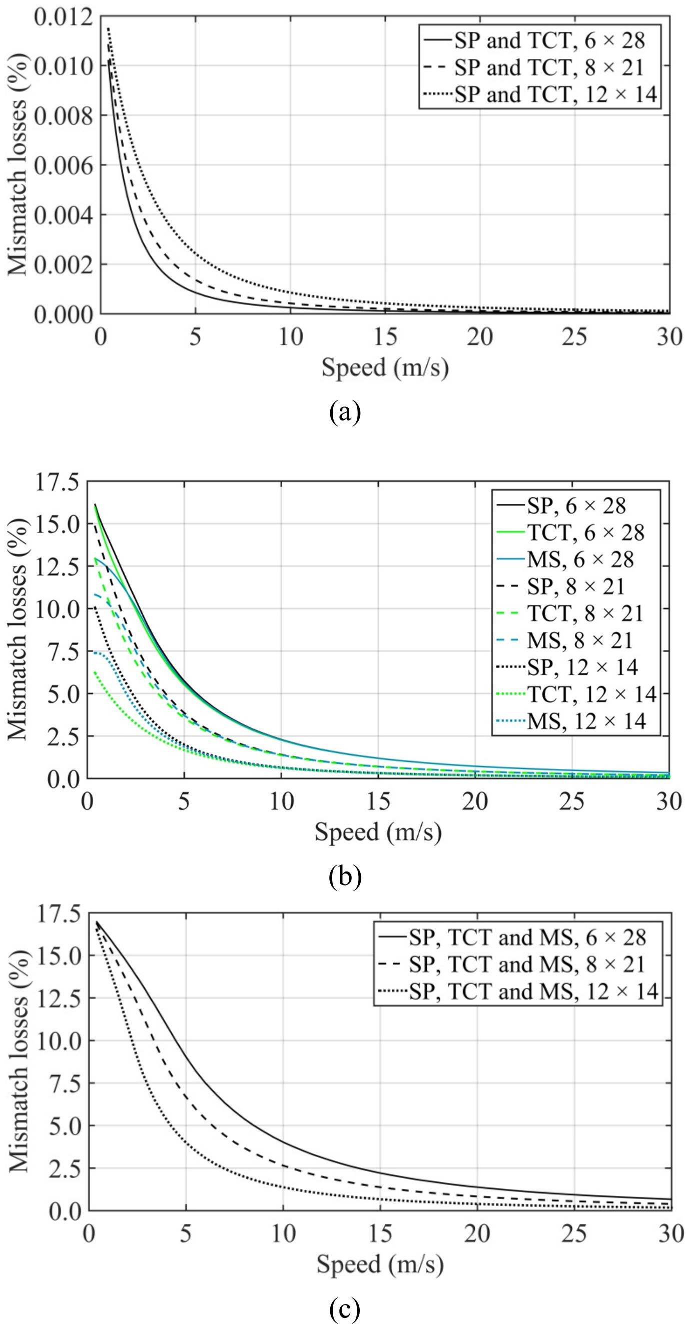

(a)

(b)

(c)

Figure 7.6. Relative mismatch losses of the SP, TCT and MS configurations as a function of the apparent speed during partial shading caused by the movement of a typical shadow edge, with apparent movement directions of 0° (a), 45° (b) and 90° (c), over the PV array.

tions. Moreover, it has been presented in Chapter 6 that the output power fluctuations caused by moving clouds are practically the same for the SP, TCT and MS configurations.

The second notable finding of real practical importance is that the mismatch losses due to irradiance transitions caused by moving clouds increased strongly with the increasing length of the PV module strings, except in the case of perpendicular shadow edge movement. However, in the case of perpendicular shadow edge movement, the mismatch losses were negligible. The conclusion is that, from a mismatch losses point of view, PV strings should not be installed in straight rows. Instead, the diameter of the PV module string area should be minimised to minimise the mismatch losses in accord with the earlier findings of Mäki and Valkealahti (2012). The effect of PV string length on the mismatch losses is discussed in more detail in Section 7.3.

The third notable finding is that the apparent direction of movement of shadow edges had a notable effect on the mismatch losses. The relative mismatch losses were the largest in the case of parallel and the smallest in the case of perpendicular shadow edge movement with respect to the PV strings. Based on the results, PV arrays should be placed so that the dominant apparent direction of movement of shadow edges is perpendicular to the PV strings as presented earlier in Lappalainen et al. (2013a and 2013b). The effect of the geographic orientation of PV arrays on the mismatch losses of the arrays is discussed in more detail in Section 7.3.

7.2 Mismatch losses during identified irradiance transitions

Mismatch losses during all the identified irradiance transitions were studied by directly using the curve fits of Eq. (3.2). The relative mismatch losses during all the identified irradiance transitions, the largest relative mismatch losses during a single irradiance transition and the largest instantaneous relative mismatch losses during the identified transitions for the 6 × 28, 8 × 21 and 12 × 14 PV arrays with the SP, TCT and MS electrical configurations and a typical east-west orientation are presented in Table 7.1. The relative mismatch losses during all the identified transitions were the largest, about 4%, for the 6 × 28 SP array, and they decreased with decreasing string length. The differences between the electrical PV array configurations were small. However, the mismatch losses were the largest for the SP configuration. With the string lengths of 28 and 21 PV modules, the mismatch losses of the TCT configuration were larger

Table 7.1. Relative mismatch losses of the studied PV arrays during all the identified irradiance transitions.

Electrical configuration	Layout	Relative mismatch losses (%)	Largest relative mismatch losses during an irradiance transition (%)	Largest instantaneous relative mismatch losses (%)
SP	6 × 28	4.04	23.7	61.1
SP	8 × 21	2.86	21.9	58.7
SP	12 × 14	1.63	21.6	53.5
TCT	6 × 28	3.92	23.7	60.6
TCT	8 × 21	2.69	21.0	58.1
TCT	12 × 14	1.40	21.4	53.3
MS	6 × 28	3.87	19.7	58.0
MS	8 × 21	2.68	19.3	56.6
MS	12 × 14	1.48	17.9	52.5

than those of the MS configuration, while with the string length of 14 modules the mismatch losses behaved oppositely. The largest relative mismatch losses during a single irradiance transition and the largest instantaneous relative mismatch losses were over 23% and 61%, respectively, for the 6 × 28 array layout with the SP configuration. Both of these maximum mismatch losses decreased only slightly with changing array layout or electrical configuration. In addition to actual mismatch losses during the irradiance transitions, mismatch between PV modules increases the transition rates of the PV output power with respect to the initial irradiance transition rates as illustrated in Fig. 6.1.

Because of the minor differences between the electrical PV array configurations, only the SP configuration is considered in the rest of this section. The SP configuration was selected since it has the largest mismatch losses and it is most commonly applied in real PV systems.

The relative cumulative frequencies of the relative mismatch losses for the three PV array layouts of the SP configuration during all the identified irradiance transitions are presented in Fig. 7.7. The relative mismatch losses were most of the time small, while large mismatch losses also seldom took place. Half of the time during the transitions the relative mismatch losses of the 6 × 28, 8 × 21 and 12 × 14 arrays were less than 0.54%, 0.31% and 0.15%, respectively, and 80% of time they were less than 7.1%, 4.4% and 2.2%, respectively. The mismatch losses increased clearly with the increasing length of the strings in accord with Table 7.1 and only a fraction of the irradiance transitions caused major mismatch losses. Those transitions had typically high SS and short length.

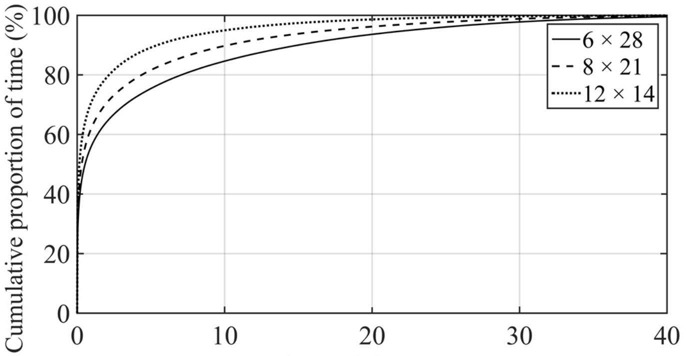

Figure 7.7. Relative cumulative frequencies of the relative mismatch losses of three PV array layouts of the SP configuration during all the identified irradiance transitions.

The scatter plots between the relative mismatch losses of the 6 × 28 and 12 × 14 array layouts with the SP configuration and the SS for all the identified irradiance transitions are presented in Fig. 7.8. Further, quadratic polynomial fits to the simulation results are presented. It is worth noting that the 40% limit of minimum acknowledged SS was used in the identification of the irradiance transitions. The results show that the median, upper limit and dispersion of the mismatch losses increase with the increasing SS. The polynomial fits are similar in shape compared to the curves in Fig. 7.4 (b) representing the relative mismatch losses of these arrays as a function of the SS during PS caused by the movement of a typical shadow edge, with apparent movement direction of 45°, over the array.

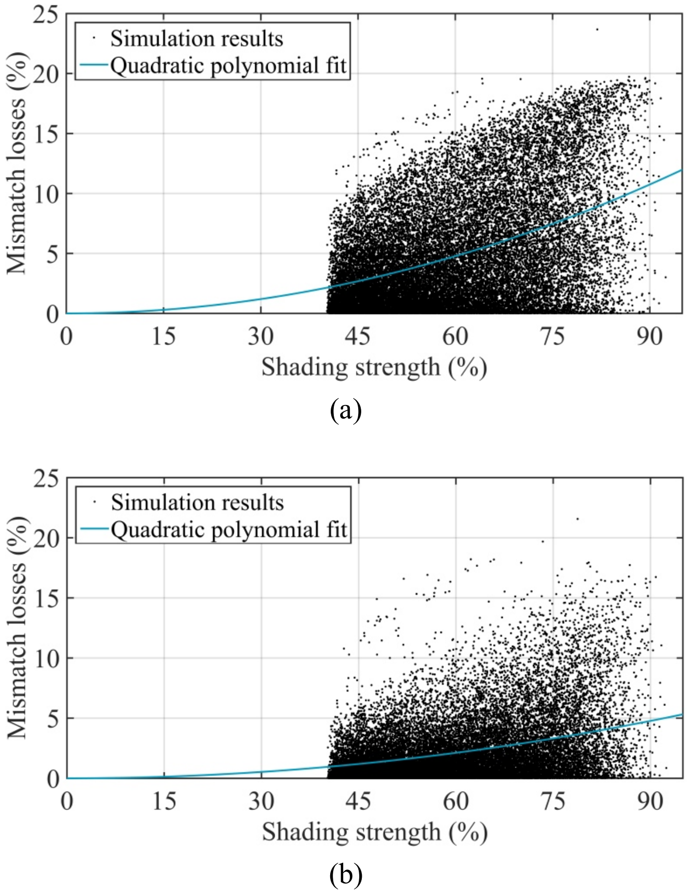

Figure 7.8. Scatter plots between the relative mismatch losses of the 6 × 28 (a) and 12 × 14 (b) PV array layouts with the SP configuration and the shading strength of all the identified irradiance transitions and curve fits to the data.

In the case of the 6 × 28 array, the relative mismatch losses of over 19% were always caused by dark clouds leading to SSs over 64%. However, as presented in Chapter 4, these shadows are quite rare and clouds with higher transparency occur more often. The polynomial fits to the simulation results demonstrate how the typical mismatch losses decrease rabidly towards 0% when SS decreases below the 40% limit. This implicates that weak shading transitions caused by moving clouds do not cause mismatch losses of major general importance.

7.3 Effects of the PV array layout and orientation on mismatch losses

The effects of PV array layout and its geographic orientation on the mismatch losses of PV arrays were studied by using the parametrisation method of irradiance transitions. The relative mismatch losses of an east-west oriented PV array with the SP, TCT and MS electrical configurations are presented as a function of the string length in Fig. 7.9 during all the identified irradiance transitions. In accord with the earlier results of this chapter, the mismatch losses increased with the increasing string length since irradiance differences between the PV modules of a string increases with the increasing physical string length. The results of Fig. 7.9 are also in line with the study of Torres Lobera and Valkealahti (2013), where the mismatch losses due to moving clouds in series-connected PV arrays were found to be more than 100 times larger than in parallel-connected arrays. The relative mismatch losses of the arrays with strings of 28 PV modules were around 3.5% and the ones of the arrays with the shortest strings can be regarded as negligible. The differences between the mismatch losses of different electrical PV array configurations were again very small. However, the mismatch losses in the TCT and MS electrical configurations were smaller than in the SP configuration in line with the results of Lappalainen et al. (2013a, 2013b) and Vijayalekshmy et al. (2014). The differences in the mismatch losses between different electrical array configurations are further demonstrated in Fig. 7.10 where the mismatch losses of the SP, TCT and MS configurations with respect to the ones of the SP configuration are presented as a function of the PV array string length during all the identified irradiance transitions.

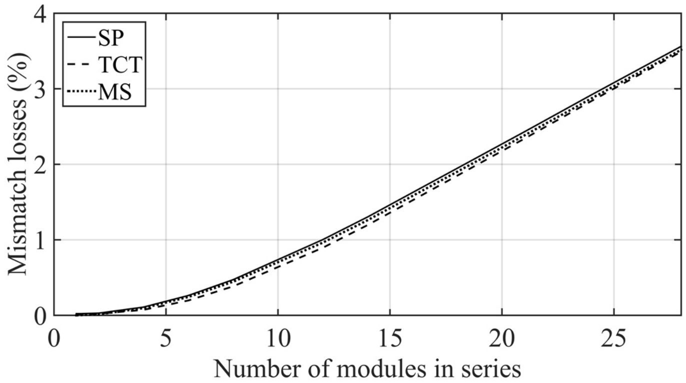

Figure 7.9. Relative mismatch losses of the east-west oriented SP, TCT and MS configurations as a function of the PV array string length during all the identified irradiance transitions. The total number of PV modules in the array is constant 168.

One of the main results of this thesis is that mismatch losses due to cloud shadings are practically independent of the electrical PV array configuration. The reason for this outcome is that the length of a typical irradiance transition region is much longer than the diameters of the

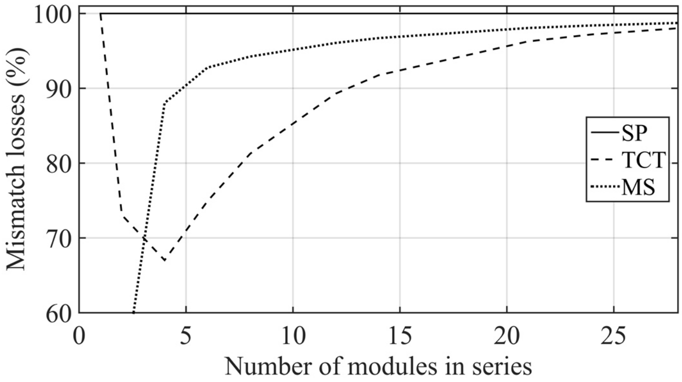

Figure 7.10. Mismatch losses of the east-west oriented SP, TCT and MS configurations with respect to the ones of the SP configuration as a function of the PV array string length during all the identified irradiance transitions. The total number of PV modules in the array is constant 168.

studied PV arrays, thus causing only minor irradiance differences between adjacent PV modules. The relative differences of mismatch losses between the electrical configurations are studied a bit further to convince the readers conclusively on this issue.

As shown in Fig. 7.10, the relative differences in the mismatch losses between the electrical array configurations are the biggest at small PV module string lengths. With string length of one module, all the modules are connected in parallel, and thus the SP and TCT configurations are identical, leading to identical mismatch losses and the MS configuration has no mismatch losses at all since all of its modules are controlled individually. With the string length of six modules, the relative difference in the mismatch losses is still around 25% for the TCT configuration, but much smaller for the MS configuration. For longer PV strings, the relative differences decrease rabidly with the increasing length. However, one must recognise that the mismatch losses of all the configurations are very small at small string lengths (Fig. 7.9) and the differences in the mismatch losses between the electrical PV array configurations are indeed negligible irrespective of the string length. Moreover, it has been presented in Chapter 6 that the output power fluctuations caused by moving clouds are practically the same for the studied electrical PV array configurations.

These results indicate that the use of the TCT configuration, or other configurations with additional connections between PV module strings, is not economically profitable in large-scale PV systems. They increase the cost of the PV system but produce only minor benefit under PS conditions caused by moving clouds. Because of the minor differences between the studied electrical array configurations, only the SP configuration is considered in the rest of this chapter. The SP configuration was selected since it has the largest mismatch losses, represent well all electrical configurations and is most commonly applied in real PV systems.

The relative mismatch losses of six different PV array layouts with the SP configuration during all the identified irradiance transitions are presented as a function of the array orientation in Fig. 7.11. Angle 0° denotes the basic east-west orientation of the PV strings and the angle increases clockwise. The array orientation has a clear effect on the mismatch losses of the studied array layouts, but not as large as could be anticipated based on the distributions of the apparent direction of movement of the identified shadow edges presented in Fig. 4.25.

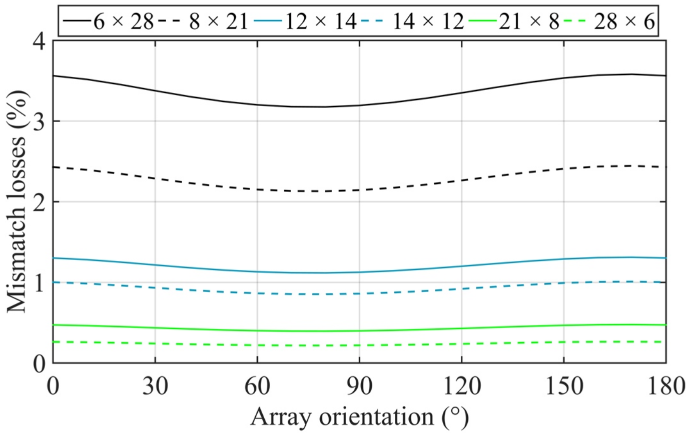

Figure 7.11. Relative mismatch losses of six different PV array layouts of the SP configuration as a function of the array orientation during all the identified irradiance transitions.

The absolute change of the mismatch losses with the varying array orientation was the higher the longer were the PV strings while the relative change behaved oppositely. The relative mismatch losses of the 28 × 6 array layout changed almost 22% with the varying array orientation, while for the 6 × 28 layout the changes were only around 13%. The maximum relative changes of the relative and absolute mismatch losses of the studied six array layouts due to the array orientation are presented in Table 7.2.

Table 7.2. The maximum relative changes of the relative and absolute mismatch losses of six different PV array layouts of the SP configuration caused by the varying array orientation.

Layout	Maximum change of relative mismatch losses (%)	Maximum change of absolute mismatch losses (%)
6 × 28	12.8	14.1
8 × 21	14.7	15.3
12 × 14	17.4	16.8
14 × 12	18.3	17.3
21 × 8	20.5	18.3
28 × 6	21.8	18.6

The reason for the effect of the array orientation on the mismatch losses is the uneven distribution of the apparent direction of movement of the shadow edges (see Fig. 4.25). As presented earlier in Lappalainen et al. (2013a and 2013b), the movement direction of shadow edges has a substantial effect on the mismatch losses. The mismatch losses are the smallest when the dominant direction of movement of the shadow edges is perpendicular to the PV strings.

The effects of PV array layout and its orientation on the PV power production during PSs caused by moving shadow edges is further illustrated in Fig. 7.12 where the average power of the studied PV array layouts of the SP configuration is presented as a function of the array orientation during all the identified irradiance transitions with respect to the 6 × 28 layout. The power increased with the decreasing string length. The maximum power gain achieved by the layout with the shortest strings was 3.4% for array orientation of 170°, when the mismatch losses in the 6 × 28 array were the largest. This array orientation is close to typical installations of fixed PV string systems facing due south.

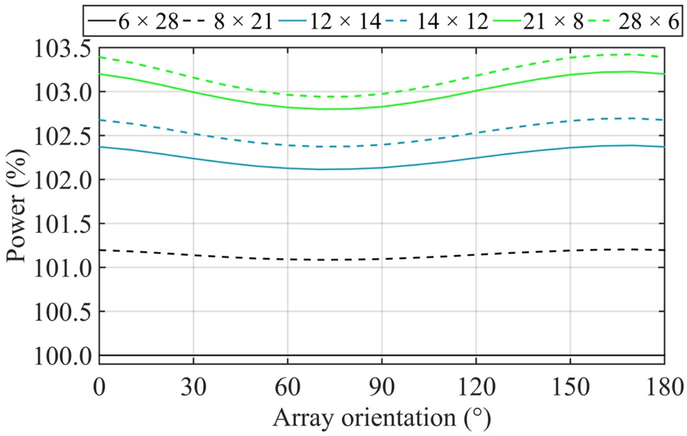

Figure 7.12. Average power of six different PV array layouts of the SP configuration with respect to the 6 × 28 modules array layout as a function of the array orientation during all the identified irradiance transitions.

It is noteworthy that the presented studies of the effects of array orientation on the output power variation and mismatch losses are based on certain simplifications and assumptions. In the simulations, the PV array was chosen to be under the constant STC irradiance of 1000 W/m^2 before each irradiance fall. However, in reality, the orientation of the modules affects the irradiance reaching the surface of the modules. Since the effect of array orientation on the mismatch losses, as well as on the output power variation, of PV arrays was found to be quite small, PV arrays should be oriented so that the amount of irradiance on the PV modules is maximised.

While the power gain of PV array layouts with short strings can be regarded as significant during PSs caused by shadow edges, it is good to be conscious that the array layout has no effect on the power production under uniform irradiance conditions. Most of the mismatch losses can be avoided by applying short strings in the PV arrays or by minimising the maximum dimensions of the strings. However, sharp shadows caused by nearby objects can lead to significantly larger mismatch losses and to bigger differences between the electrical PV array configurations.

The overall finding of this section is that the mismatch losses of PV arrays caused by moving clouds do not depend, in practice, at all on the electrical PV array configuration. Also the shape of the array as such is not important from the point of view of the mismatch losses. Only the length of the PV strings has a considerable effect on the mismatch losses so that the losses increase with the increasing string length since irradiance differences between the series-connected PV modules increases with the increasing string length. On the contrary, the mismatch losses are not very sensitive to the number of PV strings connected in parallel, which is of practical importance for the designing of the layouts of utility-scale PV power plants. The mismatch losses were the largest for the PV arrays oriented in line with the dominant apparent direction of movement of cloud shadow edges. However, since the effect of array orientation on the mismatch losses was found to be quite small, PV arrays should be oriented so that the amount of irradiance on the PV modules is maximised in order to maximise the energy production of the arrays.

7.4 Overall effect of the mismatch losses caused by moving clouds

The total mismatch losses of PV plants caused by moving clouds can be estimated based on the results of Section 7.2 and irradiance measurements. For this purpose, the irradiance transition identification method presented in Section 3.1 was applied to identify all the transitions with SS over 5% during which the moving irradiance average of five seconds changed more than 1.5 W/(m^2s). With these lower limits of irradiance transition characteristics, all transitions should be considered with some practically meaningful mismatch losses.

In total, 189,282 irradiance transitions were identified in the same measurement data of irradiance sensor S5 as earlier. The relative number of the identified irradiance transitions is presented as a function of the limit of minimum acknowledged SS in Fig. 7.13 (a). The proportion of the irradiance transitions with more than 40% SS was about 23% of all the identified transitions, meaning that clouds cause mostly week shadings with small SSs. The proportion of the time taken by all the identified irradiance transitions is presented as a function of the lower limit of acknowledged SS in Fig. 7.13 (b). The total duration of the transitions with over 5% SS was about 6% of the time, i.e., about 1.4 h in a day. This is a considerable share of the power production time for PV generators.

The total mismatch losses of the 6 × 28, 8 × 21 and 12 × 14 PV arrays with the SP configuration caused by all the 189,282 identified irradiance transitions were estimated by the following approach. The relative mismatch power losses of the 6 × 28 SP array layout corresponding to the SS of each transition were obtained from the fit of Fig. 7.8 (a) and multiplied by the energy produced by the PV array during the PS as if the PV modules were operating separately.

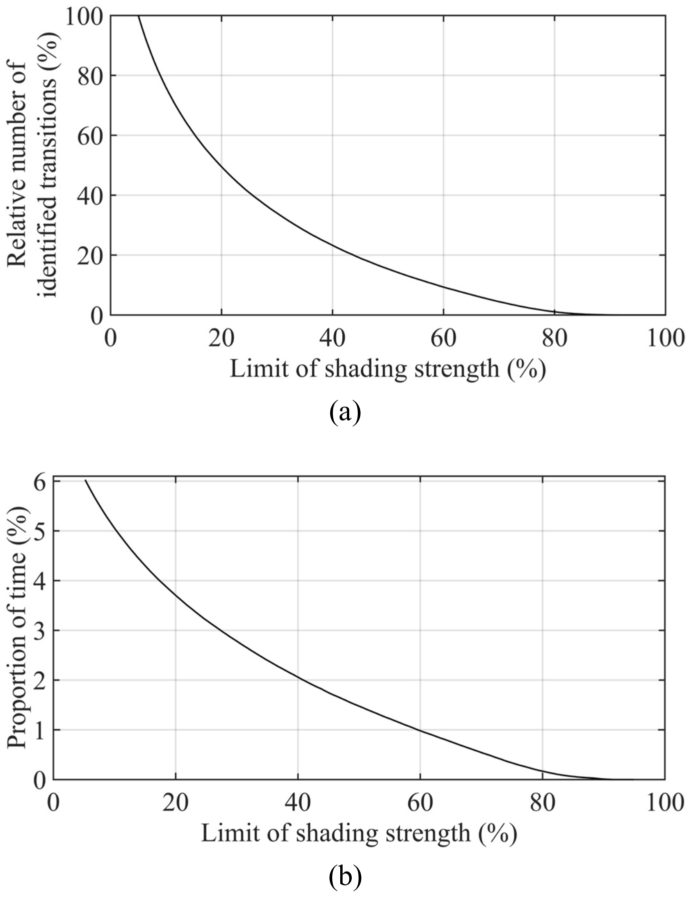

Figure 7.13. Relative number of the identified irradiance transitions (a) and proportion of the time taken by all the identified irradiance transitions (b) as a function of the lower limit of acknowledged shading strength.

The mismatch losses for the 8 × 21 and 12 × 14 SP array layouts were calculated accordingly. The energy produced during the PS was calculated for a single PV module using the irradiance data measured with a sampling frequency of 10 Hz, and then was scaled for the PV array by the number of PV modules in the array and by using the average durations of the simulation periods as presented in Table 5.4. The energy production during the 15-month period was calculated similarly than the energy productions during the PSs by using the measured irradiance data with a sampling frequency of 1 Hz. Finally, the relative total mismatch losses caused by moving clouds were calculated dividing the sum of the mismatch losses during the PSs by the total energy production for the 15 months.

The relative total mismatch losses of the 6 × 28, 8 × 21 and 12 × 14 PV arrays with the SP configuration are presented as a function of the lower limit of SS of the identified transitions in Fig. 7.14. The relative total mismatch losses decreased strongly with decreasing string length. In total, almost 80% of the total mismatch losses were caused by the irradiance transitions with over 40% SS, although the proportion of these transitions was only slightly over 20% of all the analysed transitions (Fig. 7.13 (a)). This result supports the selection of the 40% limit of minimum acknowledged SS used in the identification of irradiance transitions. Further, the relative total mismatch losses level off with the decreasing limit of the SS at small values, indicating that the chosen 5% lower limit is small enough for the presented study.

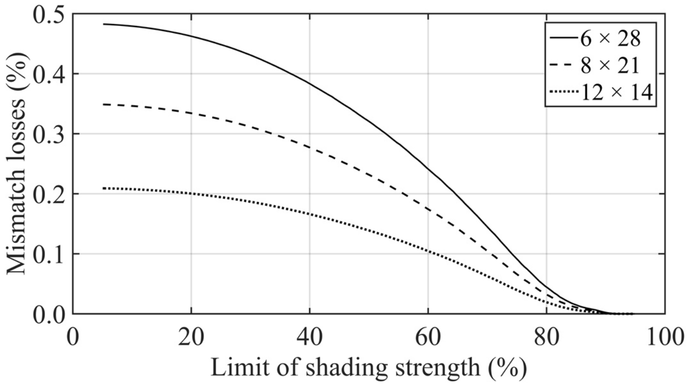

Figure 7.14. Relative total mismatch losses of three PV array layouts of the SP configuration as a function of the lower limit of acknowledged shading strength during all the identified irradiance transitions.

The total mismatch losses of the 6 × 28, 8 × 21 and 12 × 14 PV arrays caused by moving clouds were about 0.48%, 0.35% and 0.21%, respectively. In total, the mismatch losses caused by moving clouds do not seem to be a major problem for PV power production. However, minor improvement in energy production can be achieved by minimising the maximum diameter of PV module strings.

The distribution of the total mismatch losses as a function of the SS of the irradiance transitions is presented in Fig. 7.15. The distribution is the same for all the three studied PV array layouts. The proportion of the mismatch losses caused by the transitions with SSs less than 20% was small, although the share of these transitions was about half of all the transitions (Fig. 7.13 (a)). The reason for this is that these transitions caused by moving clouds with high transparency cause only minor mismatch losses as can be seen in Fig. 7.8. For the irradiance transitions with very high SSs, the situation was opposite; albeit the mismatch losses during

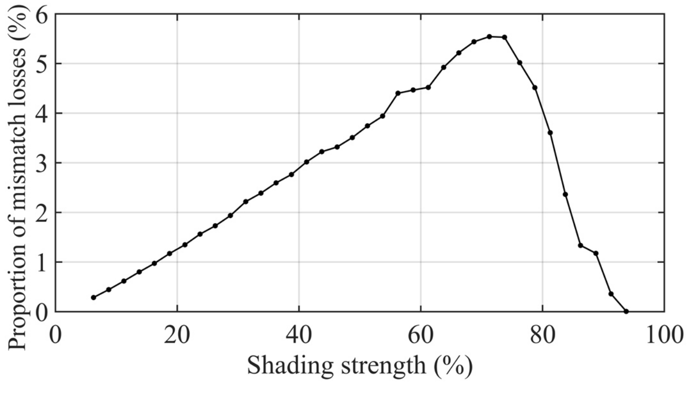

Figure 7.15. Proportion of total mismatch losses caused by irradiance transitions with different shading strengths.

these transitions can be large, these transitions are very rare. Hence, the proportion of the mismatch losses caused by the shadow edges of extremely dark clouds was also small. Most of the mismatch losses, about 70%, were caused by the irradiance transitions with SSs between 40% and 80%. The SSs of these transitions are high enough to cause major mismatch losses and they are frequent enough to have a high cumulative effect.

In this study, especially in the estimation of the total mismatch losses caused by moving clouds, several assumptions were made. Irradiance transitions identified in single point measurements were used, and it was assumed that the identified shadows covered the whole PV array. For the PV array, the number of irradiance transitions can be larger than for a single point since the PV array detects irradiance fluctuations on a larger area than a point sensor. However, the point sensor measurement describes the irradiance at the centre of the PV array and irradiance transitions taking place only on the border of the array will shade the whole array marginally like the transitions with small SSs and thus cause only minor mismatch losses. In conclusion, the use of the single point irradiance measurements did not cause major errors to the presented results.

In the method to define the apparent velocities of the identified shadow edges presented in Section 3.5, the following three assumptions were used: the apparent velocity of the shadow edge while passing over the used irradiance sensor triplet is constant, the shadow edge is linear across the sensor array and the shadow covers all the three sensors. These assumptions are generally satisfied for closely placed sensors, but the results were used for the whole PV array in this study. However, the maximum dimensions of the studied 6 × 28, 8 × 21 and 12 × 14 PV arrays (Table 5.3) are not drastically larger than the dimensions of the sensor array. Therefore, the cloud shadow edges can be assumed to be nearly linear for the whole array area and the changes in their apparent velocities while passing over the array can be expected to be small. Further, it is presented in Fig. 7.6 that the mismatch losses are sensitive to the variation of the apparent speed only at slow speeds. Thus, these assumptions of the linearity and constant apparent velocity of shadow edges should not have caused significant errors to the results.

In the simulations, the temperature of all the PV modules was assumed to be the same. However, in reality, irradiance differences cause temperature differences and thus mismatches between the modules. Moreover, mismatch losses caused by temperature differences can also occur whether the whole array is shaded or unshaded. However, the thermal mass of the PV modules is so high and the irradiance transitions are mostly so fast that, during most of the transitions, the module temperatures do not change considerably. During the longest transitions, temperature changes may be considerable. However, in these cases, irradiance differences between the modules are small, thus leading to only small temperature differences.

Only the time when a PV array was becoming shaded or unshaded, i.e., when a shadow edge was moving over the array, was studied. However, some mismatch losses also exist when the identified transitions are not taking place since the irradiance during a clear sky or overcast situation is never perfectly even, i.e., there are always some differences in the irradiance levels received by the PV modules. However, the differences in irradiance levels between the modules in those situations are typically very small leading to minor mismatch losses. Thus, the mismatch losses caused by moving clouds during clear sky conditions or when the whole array is shaded can be regarded as negligible.

In conclusion, several assumptions were made, and thus the total mismatch losses of PV arrays caused by moving clouds might be somewhat larger than are presented in this section. However, based on the presented results it is clearly evident that the total mismatch losses of PV arrays caused by moving cloud shadows are very small. This result is valid for larger PV power plants as well since PV arrays are the operational units of large PV power plants.

It is noteworthy that only the mismatch losses caused by moving clouds were studied in this thesis and that there are also several other sources of mismatch losses. Sharp shadows caused by nearby objects can lead to significantly larger mismatch losses and to bigger differences between the electrical PV array configurations. Moreover, the mismatch losses caused by manufacturing tolerances exist in every PV system and the soiling and damages of PV modules can also cause mismatch losses. Hence, the total mismatch losses of PV systems might be substantially larger than the mismatch losses caused by moving clouds. In addition to the mismatch losses, overpassing cloud shadows cause losses through failures in MPPT. MPPT losses are largely dependent on the used MPPT algorithm and might momentarily be much larger than the mismatch losses. Thus, although the total mismatch losses caused by moving clouds are small, the total losses caused by moving clouds might be substantially larger. Further, as presented in Chapter 6, cloud shadows can cause fast irradiance transitions leading to fluctuations in the output power of PV systems, which can lead to power quality problems and grid stability issues.

8 CONCLUSIONS

In this thesis, the output power variation and mismatch losses of PV arrays caused by the edges of moving cloud shadows were studied by simulations based on a comprehensive analysis of the measured irradiance data of the TUT solar PV power station research plant. Methods to identify irradiance transitions and shading periods due to moving clouds in measured irradiance data and a method to determine apparent shadow edge velocity were developed. The characteristics of irradiance transitions caused by the edges of cloud shadows were studied comprehensively. A mathematical model of irradiance transitions to be used in the simulations of PV system operation and a parametrisation method of irradiance transitions to make the simulations computationally less demanding were developed and verified.

A lot of academic research has been conducted and is most probably ongoing related to the mitigation of the effects of PS introducing various electrical configuration schemas, shading dispersion techniques, etc. However, those studies are typically based on hypothetical PS conditions lacking the knowledge of real irradiance transitions caused, for example, by moving clouds. In this thesis that gap of knowledge was filled up by analysing the real shadings caused by moving clouds. The results of the irradiance transition analysis and the developed methods can be exploited in a wide range of studies of PV system operation under PS conditions caused by moving clouds, e.g. in studies of mismatch losses, output power variation, energy storage requirements, MPP characteristics and MPPT losses. The develop methods are not regionally bounded.

A total of around 43,000 irradiance transitions were identified in 15 months of data measured with one individual irradiance sensor during spring, summer and autumn in 2011–2014. A total number of about 27,000 irradiance transitions were thus identified by all the sensors of the used sensor triplet. Irradiance transitions caused by moving clouds can be very fast, irradiance was observed to change over 400 W/m^2 in 0.1 s during an irradiance transition. The duration of the irradiance transitions varied a lot from a second up to several minutes while the shading strength of the transitions varied from very thin shadings up to 90%. The apparent speed of the shadow edges varied considerably with an average value of around 9 m/s. Around 65% of the identified shadow edges moved towards the directions from north to south-east. The length of shadow edges caused by moving clouds was found to be typically around 100 meters, which is large enough to affect the operation of PV power plants of all sizes causing output power fluctuations, mismatch losses, MPPT failures, etc.

Based on the presented results of the characteristics of the shadows of moving clouds it seems evident that they inflict a considerable amount of power fluctuations for PV power plants of all sizes. It is also evident that the shadows of moving clouds cause gentle irradiance transitions leading typically to only minor irradiance differences between adjacent PV modules. In particular in large-scale PV plants, shadings are mostly caused by moving clouds, and sharp shadows, which are typically caused by nearby objects, can be considered as rare worst-case scenarios.

The output power variation and mismatch losses of various electrical PV array configurations were studied during the identified irradiance transitions. The effects of irradiance transition characteristics and the layout and geographic orientation of PV arrays on the output power variation and mismatch losses were studied and the overall effect of the mismatch losses caused by moving clouds on the energy production of PV plants was determined. The study was conducted using the developed mathematical model of irradiance transitions and an experimentally verified MATLAB Simulink model of a PV module. The developed parametrisation method of irradiance transitions was used to study the effects of the layout and geographic orientation of PV arrays on the output power variation and mismatch losses. The use of the parametrisation method is computationally less demanding than the direct use of irradiance transitions or their curve fits and thus enables more demanding and complex simulations of the operation of PV systems.

The differences in the output power variation and mismatch losses between the studied electrical PV array configurations were small since shadows of moving clouds produce gentle irradiance transitions causing typically only minor irradiance differences between adjacent PV modules. Only the steepest and fastest shadow edges bring about some differences on the operation of different electrical PV array configurations. This indicates that the studies related to different electrical PV array configurations, shading dispersion techniques, etc. are useless from the point of view of real applications in large-scale PV systems. They increase the cost of the PV system but produce hardly any benefit under PS conditions caused by moving clouds. From the points of view of the output power variation and mismatch losses caused by clouds, one can just use the simplest electrical configuration for PV arrays.

The average rate of change of power for all the studied PV arrays during the identified irradiance transitions was around 3 %/s. The largest observed instantaneous rate of change in power was about 75 %/s. However, the use of the mathematical irradiance transition model smoothed the irradiance transitions and reduced the largest instantaneous rates of change of irradiance compared to actual irradiance transitions. Thus, even larger instantaneous rates of change can be expected to occur in the MPP power of real PV systems. That high variations in the power fed to an electric grid can have considerable negative effects on the power quality and reliability of the grid. The average rate of change in the power decreased with the increasing diagonal length of the PV array.

The relative mismatch losses during the identified irradiance transitions ranged from 1.4% to 4.0% depending on the electrical configuration and layout of the PV array. Most of the time during the transitions, the relative mismatch losses were less than 1%, while large mismatch losses also seldom took place. The largest observed instantaneous relative mismatch losses were over 60%. The mismatch losses were the largest when the dominant apparent direction of movement of the shadow edges was parallel to the PV strings and mostly depended on the length of the strings. The mismatch losses increased with the increasing string length since irradiance differences between the PV modules of a string increases with the increasing physical string length. From a mismatch losses point of view, PV strings should not be installed in straight rows. Instead, the maximum diameter of the PV module strings should be minimised to minimise the mismatch losses. On the contrary, the mismatch losses were not very sensitive to the number of PV strings connected in parallel, which is of practical importance for the designing of the layouts of utility-scale PV power plants.

The overall effect of the mismatch losses caused by moving clouds on the electricity production was about 0.5% for the PV array with strings of 28 PV modules and substantially smaller for the arrays with shorter strings. The proportions of the mismatch losses caused by the shadow edges of very dark clouds or the clouds with high transparency were small. Most of the mismatch losses, about 70%, were caused by the shadow edges having shading strengths ranging between 40% and 80% since the shading strengths of these transitions are high enough to cause major mismatch losses and they are frequent enough to have a high cumulative effect. Several assumptions were done in the estimation of the total mismatch losses caused by moving clouds. Due to these assumptions, the total mismatch losses caused by moving clouds might be somewhat larger than was estimated. However, it is evident that the total mismatch losses of PV arrays caused by moving cloud shadows are very small. Since PV arrays are the operational units of large PV power plants, this result is valid for larger PV power plants as well.

Sharp shadows, caused by nearby objects, can lead to significantly larger mismatch losses and to bigger differences between the electrical PV array configurations than the shadows of moving clouds. Moreover, the manufacturing tolerances, damages and uneven soiling of PV modules can also cause mismatch losses. Thus, the total mismatch losses of PV systems might be substantially larger than the mismatch losses caused by moving clouds. In addition to mismatch losses and output power fluctuations, overpassing cloud shadows cause MPPT losses.

The results of this thesis bring out the following future research topics:

- In this thesis, the measured irradiance data of the TUT solar PV power station research plant was analysed and the results were used to study of the output power variation and mismatch losses of PV arrays caused by moving clouds. However, the research plant has some features which restrict its use for that kind of studies, for example, the area of the research plant is relatively small, the sensors are placed at multiple altitudes and the arrangement of the sensors and PV modules is far from ideal. The presented methods could be used with irradiance measurements from other locations and the results could be compared to verify the presented methods and to see how much the characteristics of cloud shadows differ regionally.

- This thesis presented a comprehensive study of the output power variation and mismatch losses of PV arrays caused by moving clouds. By using the same methods and approaches also the characteristics of MPPs, such as the number of MPPs and the voltage behaviour of the global MPP, during irradiance transitions caused by moving clouds could be studied.

- In Chapter 6, the average rate of change in the power of a PV array was shown to decrease with the increasing diagonal length of the array. The study of the smoothing of power fluctuations with increasing PV array dimensions using a larger range of dimensions would be an interesting continuation of the research presented in this thesis.

- In this thesis, the overall effect of the mismatch losses caused by moving clouds on the energy production of PV plants was studied. However, overpassing cloud shadows cause also MPPT losses which might momentarily be much larger than the mismatch losses. The overall effect of the MPPT losses caused by moving clouds could be studied exploiting the methods and approaches presented in this thesis.

REFERENCES

Abbot, D. 2010. Keeping the Energy Debate Clean: How Do We Supply the World's Energy Needs?. Proceedings of the IEEE, 98(1), pp. 42–66.

Acciari, G., Graci, D. and La Scala, A. 2011. Higher PV Module Efficiency by a Novel CBS Bypass. IEEE Transactions on Power Electronics, 26(5), pp. 1333–1336.

Ahmadi, D., Mansouri, S.A. and Wang, J. 2011. Circuit Topology Study for Distributed MPPT in Very Large Scale PV Power Plants. 26th Annual IEEE Applied Power Electronics Conference and Exposition, Fort Worth, TX, USA, March 6–11, pp. 786–791.

Balato, M., Costanzo, L. and Vitelli, M. 2016. Reconfiguration of PV modules: A tool to get the best compromise between maximization of the extracted power and minimization of localized heating phenomena. Solar Energy, 138(16), pp. 105–118.

Belhachat, F. and Larbes, C. 2015. Modeling, analysis and comparison of solar photovoltaic array configurations under partial shading conditions. Solar Energy, 120(10), pp. 399–418.

Belhaouas, N., Ait Cheikh, M.-S., Agathoklis, P., Oularbi, M.-R., Amrouche, B., Sedraoui, K. and Djilali, N. 2017. PV array power output maximization under partial shading using new shifted PV array arrangements. Applied Energy, 187(3), pp. 326–337.

Bishop, J.W. 1988. Computer simulation of the effects of electrical mismatches in photovoltaic cell interconnection circuits. Solar Cells, 25(1), pp. 73–89.

Bosch, J.L. and Kleissl, J. 2013. Cloud motion vectors from a network of ground sensors in a solar power plant. Solar Energy, 95(9), pp. 13–20.

Bosch, J.L., Zheng, Y. and Kleissl, J. 2013. Deriving cloud velocity from an array of solar radiation measurements. Solar Energy, 87(1), pp. 196–203.

Bose, B.K. 2013. Global Energy Scenario and Impact of Power Electronics in 21st Century. IEEE Transactions on Industrial Electronics, 60(7), pp. 2638–2651.

Cai, C. and Aliprantis, D.C. 2013. Cumulus Cloud Shadow Model for Analysis of Power Systems With Photovoltaics. IEEE Transactions on Power Systems, 28(4), pp. 4496–4506.

Carrasco, J.M., Franquelo, L.G., Bialasiewicz, J.T., Galván, E., Portillo Guisado, R.C., Prats, M.A.M., León, J.I. and Moreno-Alfonso, N. 2006. Power-Electronic Systems for the Grid Integration of Renewable Energy Sources: A Survey. IEEE Transactions on Industrial Electronics, 53(4), pp. 1002–1016.

Chamberlin, C.E., Lehman, P., Zoellick, J. and Pauletto, G. 1995. Effects of mismatch losses in photovoltaic arrays. Solar Energy, 54(3), pp. 165–171.

Chapin, D.M., Fuller, C.S. and Pearson, G.L. 1954. A New Silicon *p-n* Junction Photocell for Converting Solar Radiation into Electrical Power. Journal of Applied Physics, 25(5), pp. 676–677.

Chow, C.W., Urquhart, B., Lave, M., Dominguez, A., Kleissl, J., Shields, J. and Washom, B. 2011. Intra-hour forecasting with a total sky imager at the UC San Diego solar energy testbed. Solar Energy, 85(11), pp. 2881–2893.

Dunlop, J. 2007. Photovoltaic systems. American technical publishers. 453 p.

Eftekharnejad, S., Vittal, V., Heydt, G.T., Keel, B. and Loehr, J. 2013. Impact of Increased Penetration of Photovoltaic Generation on Power Systems. IEEE Transactions on Power Systems, 28(2), pp. 893–901.

European Commission 2017. 2030 Energy Strategy. https://ec.europa.eu/energy/en/topics/energy-strategy/2030-energy-strategy. Accessed on 25.4.2017.

European Photovoltaic Industry Association 2013. Global Market Outlook for Photovoltaics 2013-2017. Technical report, European Photovoltaic Industry Association.

Fonash, S.J. 2010. Solar Cell Device Physics. 2nd ed. Elsevier. 381 p.

Fraunhofer Institute for Solar Energy Systems 2016. Photovoltaics Report. https://www.ise.fraunhofer.de/content/dam/ise/de/documents/publications/studies/Photovoltaics-Report.pdf. Accessed on 25.4.2017.

Fu, Q. Radiation (Solar). In: Holton, J.R., Curry, J.A. and Pyle, J.A. 2003. Encyclopedia of Atmospheric Sciences. Elsevier. pp. 1859–1863.

Fung, V., Bosch, J.L., Roberts, S.W. and Kleissl, J. 2014. Cloud shadow speed sensor. Atmospheric Measurement Techniques, 7(6), pp. 1693–1700.

Gautam, N.K. and Kaushika, N.D. 2002. An efficient algorithm to simulate the electrical performance of solar photovoltaic arrays. Energy, 27(4), pp. 347–361.

Gray, J.L. The Physics of the Solar Cell. In: Luque, A. and Hegedus, S. 2011. Handbook of Photovoltaic Science and Engineering. 2nd ed. John Wiley & Sons. pp. 82–129.

Green, M.A. 1998. Solar Cells: Operating Principles, Technology and System Applications. Prentice Hall. 274 p.

Green, M.A., Emery, K., Hishikawa, Y., Warta, W., Dunlop, E.D., Levi, D.H. and Ho-Baillie, A.W.Y. 2017. Solar cell efficiency tables (version 49). Progress in Photovoltaics: Research and Applications, 25(1), pp. 3–13.

Gueymard, C.A. 2004. The sun's total and spectral irradiance for solar energy applications and solar radiation models. Solar Energy, 76(4), pp. 423–453.

Hammer, A., Heinemann, D., Lorenz, E. and Lückehe, B. 1999. Short-term forecasting of solar radiation: a statistical approach using satellite data. Solar Energy, 67(1–3), pp. 139–150.

Hegedus, S. and Luque, A. Achievements and Challenges of Solar Electricity from Photovoltaics. In: Luque, A. and Hegedus, S. 2011. Handbook of Photovoltaic Science and Engineering. 2nd ed. John Wiley & Sons. pp. 1–38.

Hermann, W.A. 2006. Quantifying global exergy resources. Energy, 31(12), pp. 1685–1702.

Hinkelman, L.M. 2013. Differences between along-wind and cross-wind solar irradiance variability on small spatial scales. Solar Energy, 88(2), pp. 192–203.

Hoff, T.E. and Perez, R. 2010. Quantifying PV power Output Variability. Solar Energy, 84(10), pp. 1782–1793.

Hoff, T.E. and Perez, R. 2012. Modeling PV fleet output variability. Solar Energy, 86(8), pp. 2177–2189.

Häberlin, H. 2012. Photovoltaics: System Design and Practise. John Wiley & Sons. 701 p.

International Energy Agency 2015. Medium-Term Renewable Energy Market Report 2015. OECD/IEA. http://www.iea.org/publications/freepublications/publication/MTRMR2015.pdf. Accessed on 27.4.2017.

International Energy Agency 2016a. Key World Energy Statistics 2016. OECD/IEA. http://www.iea.org/publications/freepublications/publication/KeyWorld2016.pdf. Accessed on 25.4.2017.

International Energy Agency 2016b. Key Renewables Trends 2016. OECD/IEA. http://www.iea.org/publications/freepublications/publication/KeyRenewablesTrends.pdf. Accessed on 25.4.2017.

Kjaer, S.B., Pedersen, J.K. and Blaabjerg, F. 2005. A Review of Single-Phase Grid-Connected Inverters for Photovoltaic Modules. IEEE Transactions on Industry Applications, 41(5), pp. 1292–1306.

Lappalainen, K., Mäki, A. and Valkealahti, S. 2013a. Effects of the Size of PV Arrays on Mismatch Losses under Partial Shading Conditions Caused by Moving Clouds. 28th European Photovoltaic Solar Energy Conference and Exhibition, Paris, France, September 30 – October 4, pp. 4071–4076.

Lappalainen, K., Mäki, A. and Valkealahti, S. 2013b. Effects of the Sharpness of Shadows on the Mismatch Losses of PV Generators under Partial Shading Conditions Caused by Moving Clouds. 28th European Photovoltaic Solar Energy Conference and Exhibition, Paris, France, September 30 – October 4, pp. 4081–4086.

Lappalainen, K. and Valkealahti, S. 2014. Recognition of Irradiance Transitions Caused by Moving Clouds Harmful to the Operation of PV Systems. 29th European Photovoltaic Solar Energy Conference and Exhibition, Amsterdam, The Netherlands, September 22–26, pp. 2650–2653.

Lappalainen, K. and Valkealahti, S. 2015a. Recognition and modelling of irradiance transitions caused by moving clouds. Solar Energy, 112(2), pp. 55–67.

Lappalainen, K. and Valkealahti, S. 2015b. Recognition of Shading Events Caused by Moving Clouds and Determination of Shadow Velocity from Solar Radiation Measurements. 31st European Photovoltaic Solar Energy Conference and Exhibition, Hamburg, Germany, September 14–18, pp. 1568–1573.

Lappalainen, K. and Valkealahti, S. 2016a. Mathematical Parametrisation of Irradiance Transitions Caused by Moving Clouds for PV System Analysis. 32nd European Photovoltaic Solar Energy Conference and Exhibition, Munich, Germany, June 22–24, pp. 1485–1489.

Lappalainen, K. and Valkealahti, S. 2016b. Analysis of shading periods caused by moving clouds. Solar Energy, 135(13), pp. 188–196.

Lappalainen, K. and Valkealahti, S. 2016c. Apparent velocity of shadow edges caused by moving clouds. Solar Energy, 138(16), pp. 47–52.

Lappalainen, K. and Valkealahti, S. 2016d. Effects of Irradiance Transitions on the Output Power Fluctuations of Different PV Array Configurations. IEEE Innovative Smart Grid Technologies Asia Conference, Melbourne, Australia, November 28 – December 1, pp. 705–711.

Lappalainen, K. and Valkealahti, S. 2017a. Effects of irradiance transition characteristics on the mismatch losses of different electrical PV array configurations. IET Renewable Power Generation, 11(2), pp. 248–254.

Lappalainen, K. and Valkealahti, S. 2017b. Effects of PV array layout, electrical configuration and geographic orientation on mismatch losses caused by moving clouds. Solar Energy, 144(4), pp. 548–555.

Lappalainen, K. and Valkealahti, S. 2017c. Output power variation of different PV array configurations during irradiance transitions caused by moving clouds. Applied Energy, 190(6), pp. 902–910.

Lappalainen, K. and Valkealahti, S. 2017d. Photovoltaic mismatch losses caused by moving clouds. Solar Energy, 158(18), pp. 455–461.

Lave, M. and Kleissl, J. 2010. Solar variability of four sites across the state of Colorado. Renewable Energy, 35(12), pp. 2867–2873.

Lave, M., Kleissl, J. and Arias-Castro, E. 2012. High-frequency irradiance fluctuations and geographic smoothing. Solar Energy, 86(8), pp. 2190–2199.

Lave, M., Reno, M.J. and Broderick, R.J. 2015. Characterizing local high-frequency solar variability and its impact to distribution studies. Solar Energy, 118(8), pp. 327–337.

Leese, J.A., Novak, C.S. and Clark, B.B. 1971. An Automated Technique for Obtaining Cloud Motion from Geosynchronous Satellite Data Using Cross Correlation. Journal of Applied Meteorology, 10(1), pp. 118–132.

Lorente, D.G., Pedrazzi, S., Zini, G., Dalla Rosa, A. and Tartarini, P. 2014. Mismatch losses in PV power plants. Solar Energy, 100(2), pp. 42–49.

Marcos, J., de la Parra, Í., García, M. and Marroyo, L. 2016. Simulating the variability of dispersed large PV plants. Progress in Photovoltaics: Research and Applications, 24(5), pp. 680–691.

Marcos, J., Marroyo, L., Lorenzo, E., Alvira, D. and Izco, E. 2011. Power output fluctuations in large scale PV plants:one year observations with one second resolution and a derived analytic model. Progress in Photovoltaics: Research and Applications, 19(2), pp. 218–227.

Marcos, J., Marroyo, L., Lorenzo, E. and García, M. 2012. Smoothing of PV power fluctuations by geographical dispersion. Progress in Photovoltaics: Research and Applications, 20(2), pp. 226–237.

Marcos, J., Storkël, O., Marroyo, L., Garcia, M. and Lorenzo, E. 2014. Storage requirements for PV power ramp-rate control. Solar Energy, 99(1), pp. 28–35.

Markvart, T. 2000. Solar Electricity. 2nd ed. John Wiley & Sons. 280 p.

Massi Pavan, A., Tessarolo, A., Barbini, N., Mellit, A. and Lughi, V. 2015. The effect of manufacturing mismatch on energy production for large-scale photovoltaic plants. Solar Energy, 117(7), pp. 282–289.

Mäki, A. and Valkealahti, S. 2012. Mismatch Losses in Photovoltaic Power Generators Due to Partial Shading Caused by Moving Clouds. 27th European Photovoltaic Solar Energy Conference and Exhibition, Frankfurt, Germany, September 24–28, pp. 3911–3915.

Mäki, A. and Valkealahti, S. 2014. Differentiation of multiple maximum power points of partially shaded photovoltaic power generators. Renewable Energy, 71(11), pp. 89–99.

Mäki, A., Valkealahti, S. and Leppäaho, J. 2012. Operation of series-connected silicon-based photovoltaic modules under partial shading conditions. Progress in Photovoltaics: Research and Applications, 20(3), pp. 298–309.

National Renewable Energy Laboratory 2017. Best Research-Cell Efficiencies. https://www.nrel.gov/pv/assets/images/efficiency-chart.png. Accessed on 25.4.2017.

Nguyen, D. and Lehman, B. 2008. An Adaptive Solar Photovoltaic Array Using Model-Based Reconfiguration Algorithm. IEEE Transactions on Industrial Electronics, 55(7), pp. 2644–2654.

Patel, H. and Agarwal, V. 2008. MATLAB-Based Modeling to Study the Effects of Partial Shading on PV Array Characteristics. IEEE Transactions on Energy Conversion, 23(1), pp. 302–310.

Perez, R., Kivalov, S., Schlemmer, J., Hemker, K. and Hoff, T. 2011. Parameterization of site-specific short-term irradiance variability. Solar Energy, 85(7), pp. 1343–1353.

Perpiñán, O., Marcos, J. and Lorenzo, E. 2013. Electrical power fluctuations in a network of DC/AC inverters in a large PV plant: Relationship between correlation, distance and time scale. Solar Energy, 88(2), pp. 227–241.

Picault, D., Raison, B. and Bacha, S. 2009. Guidelines for evaluating grid connected PV system topologies. IEEE International Conference on Industrial Technology, Gippsland, Australia, February 10–13, 5 p.

Picault, D., Raison, B., Bacha, S., de la Casa, J. and Aguilera, J., 2010. Forecasting photovoltaic array power production subject to mismatch losses. Solar Energy, 84(7), pp. 1301–1309.

Potnuru, S.R., Pattabiraman, D., Ganesan, S.I. and Chilakapati, N. 2015. Positioning of PV panels for reduction in line losses and mismatch losses in PV array. Renewable Energy, 78(6), pp. 264–275.

Pulvirenti, F., La Scala, A. and Pennisi, S. 2012. Low Voltage-Drop Bypass Switch for Photovoltaic Applications. IEEE International Symposium on Circuits and Systems, Seoul, South Korea, May 20–23, pp. 2283–2286.

Rakesh, N. and Madhavaram, T.V. 2016. Performance enhancement of partially shaded solar PV array using novel shade dispersion technique. Frontiers in Energy, 10(2), pp. 227–239.

Riehl, H. 1962. Jet Streams of the Atmosphere. Technical Report No. 32. Colorado State University, Fort Collins. 117 p.

Roche, D., Outhred, H. and Kaye, R.J. 1995. Analysis and Control of Mismatch Power Loss in Photovoltaic Arrays. Progress in Photovoltaics: Research and Applications, 3(2), pp. 115–127.

Rodrigo, P., Velázquez, R., Fernández, E.F., Almonacid, F. and Pérez-Higueras, P.J. 2016. Analysis of electrical mismatches in high-concentrator photovoltaic power plants with distributed inverter configurations. Energy, 107(14), pp. 374–387.

Sahu, H.S., Nayak, S.K. and Mishra, S. 2016. Maximizing the Power Generation of a Partially Shaded PV array. IEEE Journal of Emerging and Selected Topics in Power Electronics, 4(2), pp. 626–637.

Shams El-Dein, M.Z., Kazerani, M. and Salama, M.M.A. 2013a. An Optimal Total Cross Tied Interconnection for Reducing Mismatch Losses in Photovoltaic Arrays. IEEE Transactions on Sustainable Energy, 4(1), pp. 99–107.

Shams El-Dein, M.Z., Kazerani, M. and Salama, M.M.A. 2013b. Optimal Photovoltaic Array Reconfiguration to Reduce Partial Shading Losses. IEEE Transactions on Sustainable Energy, 4(1), pp. 145–153.

SolarPower Europe 2016. Global Market Outlook for Solar Power 2016 – 2020. Technical report, SolarPower Europe, 40 p.

Stubenrauch, C.J., Rossow, W.B., Kinne, S., Ackerman, S., Cesana, G., Chepfer, H., Di Girolamo, L., Getzewich, B., Guignard, A., Heidinger, A., Maddux, B.C., Menzel, W.P., Minnis, P., Pearl, C., Platnick, S., Poulsen, C., Riedi, J., Sun-Mack, S., Walther, A., Winker, D., Zeng, S. and Zhao, G. 2013. Assessment of Global Cloud Datasets from Satellites: Project and Database Initiated by the GEWEX Radiation Panel. Bulletin of the American Meteorological Society, 94(7), pp. 1031–1049.

Tabanjat, A., Becherif, M. and Hissel, D. 2015. Reconfiguration solution for shaded PV panels using switching control. Renewable Energy, 82(10), pp. 4–13.

Tiedje, T., Yablonovitch, E., Cody, G.D. and Brooks, B.G. 1984. Limiting efficiency of silicon solar cells. IEEE Transactions on Electron Devices, 31(5), pp. 711–716.

Tomson, T. 2010. Fast dynamic processes of solar radiation. Solar Energy, 84(2), pp. 318–323.

Tomson, T. 2013. Transient processes of solar radiation. Theoretical and Applied Climatology, 112(3), pp. 403–408.

Tomson, T. 2014. Dynamic behaviour of diffuse solar radiation. Theoretical and Applied Climatology, 117(3), pp. 399–402.

Tomson, T. and Hansen, M. 2011. Dynamic properties of clouds *Cumulus humilis* and *Cumulus fractus* extracted by solar radiation measurements. Theoretical and Applied Climatology, 106(1), pp. 171–177.

Tomson, T. and Tamm, G. 2006. Short-term variability of solar radiation. Solar Energy, 80(5), pp. 600–606.

Torres Lobera, D., Mäki, A., Huusari, J., Lappalainen, K., Suntio, T. and Valkealahti, S. 2013. Operation of TUT Solar PV Power Station Research Plant under Partial Shading Caused by Snow and Buildings. International Journal of Photoenergy, 2013, 13 p.

Torres Lobera, D. and Valkealahti, S. 2013. Mismatch Losses in PV Power Generators Caused by Partial Shading Due to Clouds. 4th IEEE International Symposium on Power Electronics for Distributed Generation Systems, Rogers, AR, USA, July 8–11, 7 p.

Van Haaren, R., Morjaria, M. and Fthenakis, V. 2014. Empirical assessment of short-term variability from utility-scale solar PV plants. Progress in Photovoltaics: Research and Applications, 22(5), pp. 548–559.

Vijayalekshmy, S., Bindu, G.R. and Rama Iyer, S. 2014. Estimation of Power Losses in Photovoltaic Array Configurations under Moving Cloud Conditions. Fourth International Conference on Advances in Computing and Communications, Cochin, India, August 27–29, pp. 366–369.

Vijayalekshmy, S., Bindu, G.R. and Rama Iyer, S. 2016. A novel Zig-Zag scheme for power enhancement of partially shaded solar arrays. Solar Energy 135(13), pp. 92–102.

Villa, L.F.L., Picault, D., Raison, B., Bacha, S. and Labonne, A. 2012. Maximizing the Power Output of Partially Shaded Photovoltaic Plants Through Optimization of the Interconnections Among Its Modules. IEEE Journal of Photovoltaics, 2(2), pp. 154–163.

Villalva, M.G., Gazoli, J.R. and Filfo, E.R. 2009. Comprehensive Approach to Modeling and Simulation of Photovoltaic Arrays. IEEE Transactions on Power Electronics, 24(5), pp. 1198–1208.

Wang, G., Kurtz, B. and Kleissl, J. 2016. Cloud base height from sky imager and cloud speed sensor. Solar Energy, 131(9), pp. 208–221.

Wang, Y.-J. and Hsu, P.C. 2011. An investigation on partial shading of PV modules with different connection configurations of PV cells. Energy, 36(5), pp. 3069–3078.

Wenham, S.R., Green, M.A., Watt, M.E. and Corkish, R. 2007. Applied Photovoltaics. 2nd ed. Earthscan. 319 p.

Woyte, A., Van Thong, V., Belmans, R. and Nijs, J. 2006. Voltage Fluctuations on Distribution Level Introduced by Photovoltaic Systems. IEEE Transactions on Energy Conversion, 21(1), pp. 202–209.

Yadav, A.S., Pachauri, R.K. and Chauhan, Y.K. 2016. Comprehensive investigation of PV arrays with puzzle shade dispersion for improved performance. Solar Energy, 129(7), pp. 256–285.

Yadav, A.S., Pachauri, R.K., Chauhan, Y.K., Choudhury, S. and Singh, R. 2017. Performance enhancement of partially shaded PV array using novel shade dispersion effect on magic-square puzzle configuration. Solar Energy, 144(4), pp. 780–797.

Yan, R., Saha, T.K., Meredith, P., Ananth, A. and Hossain, M.I. 2016. Megawatt-scale solar variability study: An experience from a 1.2 MWp photovoltaic system in Australia over three years. IET Renewable Power Generation, 10(8), pp. 1229–1236.

Yang, F., Yang, L. and Ma, X. 2014. An advanced control strategy of PV system for low-voltage ride-through capability enhancement. Solar Energy, 109(11), pp. 24–35.

Yordanov, G.H., Midtgård, O.-M., Saetre, T.O., Nielsen, H.K. and Norum, L.E. 2013. Overirradiance (Cloud Enhancement) Events at High Latitudes. IEEE Journal of Photovoltaics, 3(1), pp. 271–277.

Young, H.D. and Freeman, R.A. 2008. University Physics with modern physics. 12th ed. Pearson Addison-Wesley. 1551 p.

Tampereen teknillinen yliopisto
PL 527
33101 Tampere

Tampere University of Technology
P.O.B. 527
FI-33101 Tampere, Finland

ISBN 978-952-15-4033-2
ISSN 1459-2045